Title
Low Dissipation Spin Currents in Magnetic Materials

Author
Hill, Daniel Mark

Publication Date
2019

Peer reviewed|Thesis/dissertation

UNIVERSITY OF CALIFORNIA

Los Angeles

Low Dissipation Spin Currents in Magnetic Materials

A dissertation submitted in partial satisfaction

of the requirements for the degree

Doctor of Philosophy in Physics

by

Daniel Mark Hill

2019

ABSTRACT OF THE DISSERTATION

Low Dissipation Spin Currents in Magnetic Materials

by

Daniel Mark Hill

Doctor of Philosophy in Physics

University of California, Los Angeles, 2019

Professor Yaroslav Tserkovnyak, Chair

This thesis advances the theory of spintronics by exploring ways in which collective spin dynamics can be manipulated in magnetic materials, with an emphasis on sytems which can exhibit low dissipation spin currents and nontrivial response to external driving.

In Chapter 1, we provide an introductory review of mesoscopic ferromagnetic dynamics. The Landau-Lifshitz equation is motivated and derived, with a brief discussion on its application in the presence of dissipative forces and external driving. Then we discuss the notion of spin superfluidity in easy plane ferromagnets and compare this to traditional Ginzberg-Landau superconductivity.

In Chapter 2, we further extend the analogy between ferromagnetism and superconductivity, and apply this anology to the study of the ferromagnet with strong coherent easy-plane anisotropy and weak in-plane coherent anisotropy. The low bias non-equilibrium phase diagram is mapped, and the potential for producing applications with superconductor-based circuit functionality at elevated temperatures is discussed.

In Chapter 3, the spin superfluid is studied in strong driving regimes in which the anaology to superconductivity begins to break down. Multiple non-equilibrium phases are discovered which are associated with the onset of non-linear effects, such as choatic oscillations and stationary soliton formation, near the spin torque injection region. Using numerical simulations

and analytical modeling, we observe a robustness in spin superfluid transport and its high bias phase diagram despite the presence of symmetry breaking dipole-dipole interactions, finite size effects, and dissipation.

In Chapter 4, we turn to microscopic magnetic lattices, in particular weakly coupled arrays of quantum spin chains with fermionizable, via a Jordan-Wigner transformation, Hamiltonians. Using mean field theory, we find models which may exhibit dissipationless spin currents closely analogous to that of superconductivity and the quantum Hall effect.

In Chapter 5, we study the manipulation of magnetic domain walls on a wire with mechanical waves. We show how ferromagnetic and anitferromagnetic domain walls can be driven by circularly and linearly polarized waves, respectively. We note the potential for applications using mechanical waves as a means for manipulating magnetic solitons in insulators.

For Chapter 6, in collaboration with an experimental study on a cleaved edge overgrowth sample, we analyze the chiral edge states of the quantum Hall effect and their tunneling properties. Our modeling provides a theoretical fooundation from which the experimental method of momentum resolved spectroscopy can provide insight into how the quantum Hall effect evolves with changing magnetic field. Spin splitting of the chiral edge states is observed in the presence of a strong in-plane magnetic field.

We close with Chapter 7 giving an outlook for future work which could build off of the research presented in this thesis.

The dissertation of Daniel Mark Hill is approved.

Sudip Chakravarty

Rahul Roy

Christopher R. Anderson

Yaroslav Tserkovnyak, Committee Chair

University of California, Los Angeles

2019

To John D. Miller, a better friend than anyone could ask for.

Contents

1 Introduction **1**

1.1 The Landau-Lifshitz equation 1

1.1.1 Motivation for and derivation of the Landau-Lifshitz equation 2

1.1.2 The Landau free energy and symmetry 5

1.1.3 Dissipation and the Landau-Lifshitz-Gilbert equation 7

1.1.4 Spin torques and boundary conditions 9

1.2 Spin superfluids 10

1.3 Comparison to traditional superconductivity 12

2 Easy-Plane Magnetic Strip as a Long Josephson Junction **16**

2.1 Introduction 17

2.2 Magnetic model 18

2.3 Relation to long Josephson junctions 21

2.4 Analytic equilibrium solutions 23

2.5 Dynamic solutions 25

2.6 Discussion 28

3 Self-stabilizing spin superfluids **29**

3.1 Introduction 29

3.2 Results 32

3.2.1 Behavior without dipolar interaction 33

3.2.2 Analytical model . . . 34
3.2.3 Impact of dipolar interaction . . . 39
3.3 Discussion . . . 40
3.4 Methods . . . 42
3.4.1 Micromagnetic simulations. . . . 42
3.4.2 Analytical model . . . 42

4 Spin analogs of superconductivity and integer quantum Hall effect in an array of spin chains 44

4.1 Introduction . . . 45
4.2 Main results . . . 47
4.3 Spin superconductivity . . . 51
4.4 Spin integer quantum Hall effect . . . 53
4.5 Discussion . . . 54

5 Mechanical Actuation of Magnetic Domain-Wall Motion 56

5.1 Introduction . . . 56
5.2 Main Results . . . 59
5.3 Transverse waves . . . 64
5.4 Torque and force. . . . 65
5.5 Ferromagnetic domain wall . . . 67
5.6 Antiferromagnetic domain wall . . . 67
5.7 Discussion . . . 68

6 Evolution of the quantum Hall bulk spectrum into chiral edge states 70

6.1 Introduction . . . 71
6.2 Results . . . 72
6.2.1 Integer quantum Hall edge states for the hard wall confinement . . . 72
6.2.2 Formation and evolution of the edge states . . . 75

6.2.3 Spin splitting and Landau level depopulation 80
6.2.4 Analytical model of resonant tunneling 81
6.3 Discussion 84
6.4 Methods 86

7 Outlook **89**

List of Figures

2.1 (a) EPF with spin injection from metal contacts on two side. The spin polarization of the current is along the z axis, while the spin-current flow is oriented along the x axis. The ferromagnet is sufficiently narrow in the transverse dimensions to treat it as quasi-one-dimensional. (b) Diagram of the inline LJJ, with W much smaller than L as well as the depth of the structure in the z direction. We assume two conventional superconductors (SC) much larger than the London penetration depth in all dimensions. The magnetic-field screening currents as well as the circulating vortices are schematically depicted with black oriented lines. The vortices in the junction map onto the domain walls depicted in (a). 20

2.2 The regions of stability for equalibium p-vortex solutions of the LJJ boundary-value problem, for $L/\lambda = 1$. The spin torques $\tau_{r,l}$ are in units of A/λ. Overlapping regions can have either solution. Outside of these regions, i.e., in the high $|\tau_r - \tau_l|$ limit, there are no stable time-independent solutions. Inset: The dependence of the critical torque τ_c, for which $\tau_r + \tau_l = 0$, on the length L in units of λ. 24

2.3 Plot of the approximate modulation of the superfluid phase solution, $\epsilon^{(0)}(x,t)$, resulting from a weak in-plane anisotropy, with $L = 1$, $\beta_d = 0.1$, $\gamma = 0.01$, $\tau_l = 1.5$, and $\tau_r = -2$. 27

3.1 Spin superfluid in the absence of dipolar interaction. (a) Schematic view of the thin film. The spin injector provides spin current with out-of-plane polarization (blue arrows). The spin sinks are shown. The red arrows represent a magnetization snapshot. (b) Initial superfluid velocity as a function of the current density (black circles) and base frequency (red circles). Three regimes of the spin superfluid are marked. Black line shows transmitted spin current τ (in the same units as superfluid velocity) calculated based on the analytical model. (c) Spatial dependence of the superfluid velocity in regime I, (d) in regime II at $j = 3.1 \cdot 10^{11}\,\mathrm{A\,m^{-2}}$, (e) in regime III at $j = 4.6 \cdot 10^{11}\,\mathrm{A\,m^{-2}}$. . . 31

3.2 Spin superfluid in the presence of dipolar interaction. (a) Threshold current as a function of film thickness. (b) Initial superfluid velocity as a function of the current density for 5 nm thick film (sub-threshold regime omitted for clarity). (c) Spatial dependence of the superfluid velocity. 38

4.1 Schematic of a bilayer of two arrays of weakly-coupled spin chains (shown as the solid lines indexed by m), each of which can be represented by a one-dimensional system of (spinless) Jordan-Wigner fermions. The top and bottom layer indices serve as the pseudospin up and down for the fermions, respectively. The green box represents a pseudospin-singlet Cooper pair of two fermions established by an Ising interlayer interaction. 46

4.2 (a) Schematic of an array of spin-orbit-coupled spin-1/2 spin chains, which can support chiral edge modes of the Jordan-Wigner fermions. The coupling of four spins (colored by yellow) illustrates the interchain interaction $\mathcal{O}$ [Eq. (4.2.2)]. (b) A schematic plot showing how the interchain interaction gives rise to chiral edge modes with the gapped bulk. At the external magnetic field h corresponding to the filling factor $\nu = 1$, the JW fermion can flow in the left direction on the top chain (colored by blue) and in the right direction on the bottom chain (colored by red) in (a), which are represented by the left blue and right red dots in (b), respectively. The particle current in the JW representation corresponds to the spin current polarized along the z axis. 47

5.1 A schematic illustration of a ferromagnetic wire with a magnetic domain wall (shown by blue thick arrows) and a transverse elastic deformation (which is exaggerated for illustrative purposes). The yellow circles represent incoming phonons, quanta of elastic waves; the yellow diamonds represents transmitted and reflected phonons. The red (blue) arrows on circles represent phonons' angular momentum in the positive (negative) z direction. Phonons are injected from the left; some of them are reflected by the domain wall and thereby exert the force on it; some of the transmitted and reflected phonons change their angular momentum and thereby exert the torque on the wall. 58

5.2 The torque τ on the domain wall by the circularly-polarized waves as a function of the wavenumber $k\lambda$ for the parameters $\kappa = 0.2$ and $a = \lambda/10$. The solid line is obtained with the analytical expression for τ in Eq. (5.2.5); the dots are obtained with τ in Eq. (5.4.2) calculated from numerical solutions of the differential equations (5.3.1). The inset shows a zoom-in at small wave vectors $k\lambda < 1$. 61

5.3 The force F on the domain wall exerted by the linearly-polarized waves perpendicular to the wall plane for the parameters $\kappa = 0.2$ and $a = \lambda/10$. The solid line is obtained with the analytical expression for F in Eq. (5.2.6); the dots are obtained with F in Eq. (5.4.3) calculated from numerical solutions of the differential equations (5.3.1). 63

6.1 **Bulk to edge correspondence. a,** Energy evolution of the center of mass (CM) position (thin blue/red curves) and the guiding center (GC) position (bold blue/red curves) for the first two Landau levels LL_0 and LL_1. Here, LL_2 is above the Fermi energy and is depopulated. The confinement (hard wall) lifts the bulk LLs in energy, resulting in corresponding edge states (solid circles) when the CM is crossing the Fermi energy E_F. Note that the Fermi energy shown here is lower than in the experiment. **b,** Same as **a** for larger magnetic field B_z, where the width $2\sigma_n = 2l_B\sqrt{2n+1}$ of LL_n is squeezed and LL_1 was depopulated, with magnetic length l_B. **c,** Coordinate system (black) and sample schematic, showing the 2DEG in light blue, upper and lower quantum wire (UW/LW) in dark blue, top gate in green, and CM for integer quantum Hall edge states in purple. Ω indicates the conductance measurement. **d,** Simplified UW and LL dispersions calculated for independent triangular and hard wall confinement. **e,** Calculated dispersion for the combined confinement potential, resulting in hybridized states H_n with avoided crossings (see inset). Here, the bulk LL_0 transforms into the UW mode at the sample edge. Gray segments indicate empty states, colored ones are filled. . . 73

6.2 **Formation and B-field evolution of the chiral integer quantum Hall edge states. a,** Differential tunneling conductance as a function of in-plane magnetic field B_y and perpendicular magnetic field B_z at $\approx 10\,\mathrm{mK}$. The 2D-wire transitions break up into multiple curves and fan out with increasing B_z, see also Supplementary Fig. 2. Horizontal resonances at small $|B_y|$, associated with wire-wire tunneling, are not affected by B_z. **b**, Larger B_y range than **a**, showing 6 fans corresponding to tunneling to modes LW_2, LW_3, and LW_4. Due to the chiral nature of the states, the fans are not seen in the data when only B_z is reversed. The sketches depict the resonance condition (black dots) at $B_z = 0$. **c**, Schematic representation of quantum wire (gray) to LL (red) tunneling at $B_z = 0.7\,\mathrm{T}$. B_y shifts the lower wire dispersion in relation to the LLs, as indicated by gray arrows of corresponding length. The blue filled parabola indicates the 2DEG dispersion for $B_z = 0$, projected onto the k_x axis. Black dots and black circle indicate resonant tunneling to bulk states and edge state, respectively. 76

6.3 **Magnetic depopulation and spin splitting of integer quantum Hall edge states.** **a,** Second derivative with respect to B_y of the differential tunnel conductance ($d^2 g_{\mathrm{T}}/dB_y{}^2$) as a function of magnetic fields B_y and B_z. **b**, Extracted resonance positions from **a**. Red, black, and light blue data correspond to tunneling between edge modes and the first (LW_1), second (LW_2) and third (LW_3) lower wire mode. **c,d,e,f,** Zoom in of **a** for regions of interest: **c,** Landau fans for $B_z < 0$ (counter-clockwise edge states $\Leftrightarrow$ right moving edge state at cleaved edge), imaged with co-propagating (white solid ellipse) and counter-propagating wire modes (white dashed ellipse).**d,** Jumps in the resonance position whenever the bulk filling changes. The three vertical bars of growing height indicate a distance of 2 nm in real space. The height ΔB_y of the bar is given by $\Delta B_y = \Delta Y B_z/d$, where ΔY is the distance in real space. Thus, the real space resolution is improving with increasing magnetic field B_z. **e,** LL spin splitting clearly visible even in undifferentiated raw data (tunneling conductance g_{T}). **f,** branching out of resonances at the transition to magnetic depopulation. 79

6.4 **Comparison of experiment and theory. a,** Landau Level wave functions for particular values of B_z chosen to visualize the important stages of magnetic field evolution. Note that the resulting vertical scale is highly nonlinear. The wave functions are obtained from a numerical Schrödinger solver, showing magnetic compression of the wave function and subsequent depopulation. The hard wall confinement completely separates wave function CM and GC position, the latter residing outside the physical sample for most of the B-field range. Hybridization of LLs and UW_1 would result in an additional node for LL wave functions at the Fermi energy. In **b,c** experimental data are compared to theoretical predictions from an analytical model and to numerical solutions from a single-particle Schrödinger solver, respectively. 83

7.1 Schematic non-equilibrium phase diagram of the easy-plane ferromaget with a driving torque on one edge in the presence of weak in-plane anisotropy. . . 90

7.2 A simplified schematic diagram of a potential spintronics-based neuromorphic computer, which would transform imputs with a anisotropic ferromagnet base neural network and then extract usable data using a traditional machine learning algorithm. 91

Acknowledgements

It is a pleasure to thank my advisor, Yaroslav Tserkovnyak, for his mentorship. I would like to thank Francoise Queval for directing me to Yaroslav when I was looking to start my research career. I would also like to thank Hector Ochoa, Richardo Zarzuela, and Se Kwon Kim for many helpful discussions and also for being exceptional role models as some of the hardest working researchers in condensed matter. Lastly, I would like to thank John D. Miller for help with navigating LaTeX and Dallar Babaian for giving me a reason to keep going.

Without these people, this thesis likely would not exist, and for their help I am eternal grateful.

Contribution of authors

Chapters 2, 4, and 5 are taken from [1–3], work done in collaboration with Se Kwon Kim and Yaroslav Tserkovnyak. Chapter 6 is taken from [4], done in collaboration with Taras Patlatiuk, Christian P. Scheller, Yaroslav Tserkovnyak, Gilad Barak, Amir Yacoby, Loren N. Pfeiffer, Ken W. West, Dominik M. Zumbühl. Chaper 3 is taken from [5], done in collaboration with Tobias Schneider, Attila Kàkay, Kilian Lenz, Jürgen Lindner, Jürgen Fassbender, Pramey Upadhyaya, Yuxiang Liu, Kang Wang, Yaroslav Tserkovnyak, Ilya N. Krivorotov, Igor Barsukov

Vita

2013	B.A. (Physics), University of California, Los Angeles
2013 – 2019	Teaching Assistant, Department of Physics and Astronomy, UCLA

Publications

"Mechanical actuation of magnetic domain-wall motion,"

Kim, S.K., Hill, D., Tserkovnyak, Y., Phys. Rev. Lett. 117, 237201(2016)

DOI: 10.1103/PhysRevLett.117.237201, arXiv:1606.05430 [cond-mat.mes-hall]

"Spin analogs of superconductivity and integer quantum Hall effect in an array of spin chains,"

Hill, D., Kim, S.K., Tserkovnyak, Y., Phys. Rev. B 95, 180405(R) (2017)

DOI: 10.1103/PhysRevB.95.180405, arXiv:1701.01509 [cond-mat.mes-hall]

"Evolution of the quantum Hall bulk spectrum into chiral edge states,"

Patlatiuk, T., Scheller, C.P., Hill, D., Tserkovnyak, Y., Barak, G., Yacoby, A. Pfeiffer, L.N., West, K.W., Zumbühl, D.M., Nat. Commun. 9, 3692 (2018)

DOI: 10.1103/PhysRevB.95.180405, arXiv:1701.01509 [cond-mat.mes-hall]

"Spin-Torque-Biased Magnetic Strip: Nonequilibrium Phase Diagram and Relation to Long Josephson Junctions,"

Hill, D., Kim, S.K., Tserkovnyak, Y., Phys. Rev. Lett. 121, 037202 (2018)

DOI: 10.1103/PhysRevLett.121.037202, arXiv:1802.04229 [cond-mat.mes-hall]

"Self-stabilizing spin superfluid,"

Schneider, T., Hill, D., Tserkovyak, Y., Kakay, A., Lenz, K., Lindner, J., Fassbender, J., Upadhyaya, P., Liu, Y., Wang, K., Krivorotov, I.N., Barsukov I., arXiv:1811.09369 [cond-mat.other]

Chapter 1

Introduction

Spin, or intrinsic quantum mechanical angular momentum, is a fundamental property in physics. Quarks, electrons, photons, the ever-present particles that constitute much of the known universe, all have spin associated with them. The study of spin and its applications is called spintronics. The research detailed in this thesis advances the theory of spintronics by exploring many ways in which collective spin dynamics can be manipulated in magnetic materials.

This chapter covers some basic preliminaries with the hopes of providing the uninitiated reader with a more solid foundation from which to better understand the following chapters. This chapter is aimed roughly at the level of an advanced undergrad or beginning graduate student.

1.1 The Landau-Lifshitz equation

The Landau-Lifshitz (LL) equation is essential for the mesoscopic or macroscopic modeling of a ferromagnet. Despite describing one of the simplest magnetic phases known in nature[1], the LL equation admits a wide range of non-trivial solutions, some of which are highly non-linear or chaotic [6]. An early phenomenological derivation of the equation was published by Lev

[1]Examples of magnetic phases that typically require somewhat more advanced treatment include antiferromagnets, ferrimagnets, spin glasses, and spin liquids.

Landau and Evgeny Lifshitz in 1935 [7]. The contemporary version of the equation, derived by Langrangian methods, was published by Gilbert in 1955 [8]. In order to understand how the LL equation arises, we will first consider the context in which a ferromagnetic phase typically develops.

1.1.1 Motivation for and derivation of the Landau-Lifshitz equation

Consider a d dimensional lattice of atoms with non-zero total spin at each lattice site. We denote the quantum mechanical spin operators at lattice site i by $\boldsymbol{S}_i = (S_i^x, S_i^y, S_i^z)$. These operators satisfy the spin commutator relations

$$[S_i^\alpha, S_j^\beta] = i\hbar\,\delta_{ij} \sum_\gamma \epsilon_{\alpha\beta\gamma}\, S_i^\gamma \tag{1.1.1}$$

where δ_{ij} is the Kronecker delta and $\epsilon_{\alpha\beta\gamma}$ is the Levi-Civita symbol. The time evolution and ground state for these spins is determined by the Hamiltonian $H(\{S_i^\alpha\})$. For example, in the case of nearest neighbor exchange coupling, easy-plane or easy-axis anisotropy, and Zeeman coupling in an applied magnetic field, the Hamilton takes the form

$$H = -J \sum_{\langle i,j \rangle} \boldsymbol{S}_i \cdot \boldsymbol{S}_j + K \sum_i (\boldsymbol{S}_i \cdot \boldsymbol{\zeta})^2 + \frac{g\mu_B}{\hbar} \sum_i \boldsymbol{S}_i \cdot \boldsymbol{B} \tag{1.1.2}$$

Here the sum over $\langle i, j \rangle$ denotes a sum over nearest neighbor lattice sites, J is exchange coupling which is taken to be positive for the case of ferromagnetism, $\boldsymbol{\zeta}$ is a unit vector pointing along the anisotropy axis, g is the Landé g-factor, μ_B is the Bohr magneton, $\boldsymbol{B}$ is the magnetic field, and K parameterizes anisotropy strength and, through its sign, determines whether the anisotropy is easy-axis ($K < 0$) or easy-plane ($K > 0$). This is an important hamiltonian which can be used to model many of the observed features of magnetic materials; however, it neglicts various potentially important features such as coupling to other types of excitations, e.g. magnon-phonon coupling, or relativistic corrections, e.g. Dzyaloshinskii-

Moriya interactions [9].

The equations of motion for the spin operators in the Heisenberg picture are

$$\frac{dS_i^\alpha}{dt} = \frac{i}{\hbar}[H, S_i^\alpha] \tag{1.1.3}$$

In principle, this equation tells us everything we need to know about how these spins behave; however,depending on the Hamiltonian, the equation may be very difficult or even impossible to solve, and even if it is solvable, the solution giving the detailed time evolution of every single spin in a macroscopic system would likely be far more information than is observable. We may instead restict our interest to a mesoscopic quantity which averages out some of the microscopic details. One such quantity is the coarse grained spin texture, defined as

$$s^\alpha(\boldsymbol{r}, t) = \frac{1}{\mathcal{V}_{\boldsymbol{r}}} \int_{\mathcal{V}_{\boldsymbol{r}}} d^d\boldsymbol{r}' \sum_i \langle S_i^\alpha \rangle \delta(\boldsymbol{r}' - \boldsymbol{r}_i) \tag{1.1.4}$$

where $\langle A \rangle$ denotes an (ensemble averaged) expectation value of the operator A. The spin texture $\boldsymbol{s}(\boldsymbol{r}, t)$ is the average spin density within a volume $\mathcal{V}_{\boldsymbol{r}}$ centered at $\boldsymbol{r}$. Now we may ask what equation of motion, analogous to (1.1.3), may be found for $s^\alpha(\boldsymbol{r}, t)$?

Starting with a simple case, we may consider just the Zeeman term in equation (1.1.2). The Heisenberg equation of motion for the spins is

$$\frac{d\boldsymbol{S}_i}{dt} = \frac{i}{\hbar}[H_{\text{Zeeman}}, \boldsymbol{S}_i] = \frac{g\mu_B}{\hbar} \boldsymbol{B} \times \boldsymbol{S}_i \tag{1.1.5}$$

This equation is convenient in that that the right hand side is linear in the spin operator, so in order to find the equation of motion for the spin texture, we can simply apply the coarse graining proceedure on both sides to get

$$\frac{d\boldsymbol{s}}{dt} = \frac{g\mu_B}{\hbar} \boldsymbol{B} \times \boldsymbol{s} \tag{1.1.6}$$

The solution to this equation can be found simply by noting that $|\boldsymbol{s}|^2$ is constant in time, because $\frac{d}{dt}|\boldsymbol{s}|^2 = 2\,\boldsymbol{s}\cdot\frac{d\boldsymbol{s}}{dt} = 0$, and that $\frac{d\boldsymbol{s}}{dt}$ is perpendicular to $\boldsymbol{s}$ and $\boldsymbol{B}$ by nature of the cross product. Thus $\boldsymbol{s}(x,t)$ rotates around the magnetic field, sweeping out a cone shape over time, at an angle set by the initial conditions.

The above proceedure does not work for the first and second terms in equation (1.1.2) because higher order terms of the form $\langle S_i^\alpha S_j^\beta\rangle$ get in the way. Instead, in order to guess at the form of the equation, we can use the correspondence principle between commutators and poisson brackets [10]

$$[\hat{f},\hat{g}] \longleftrightarrow i\hbar\{f,g\}_P + \mathcal{O}(\hbar^2) \tag{1.1.7}$$

where $\{\dots,\dots\}_P$ denotes the Poisson bracket, and we have used hats to distiguish quantum operators from corresponding classical dynamical variables. As a result, applying correspondence to equation (1.1.3), we may expect an equation of motion for the classical dynamical variable $\boldsymbol{s}(\boldsymbol{r},t)$ in the form

$$\frac{d\boldsymbol{s}}{dt} = \{\boldsymbol{s},\mathcal{F}\}_P \tag{1.1.8}$$

where the free energy, $\mathcal{F}$, is a functional of $\boldsymbol{s}$ which is in some sense a coarse grained semi-classical version of the quantum mechanical Hamiltonian. This equation can be further expanded using the classical correspondence of the spin operator commutation relations

$$\{s^\alpha(\boldsymbol{r}), s^\beta(\boldsymbol{r}')\}_P = \sum_\gamma \epsilon_{\alpha\beta\gamma}\, s^\gamma(\boldsymbol{r})\,\delta(\boldsymbol{r}-\boldsymbol{r}') \tag{1.1.9}$$

resulting in

$$\frac{d\boldsymbol{s}}{dt} = \frac{\delta\mathcal{F}}{\delta\boldsymbol{s}}\times\boldsymbol{s} \tag{1.1.10}$$

Here, comparing to equation (1.1.6), we can see that the functional derivative of the free energy with respect to spin texture acts as an effective magnetic field for the spin texture.

Equation (1.1.10) is often writen as

$$\frac{d\boldsymbol{M}}{dt} = \gamma \boldsymbol{H}_{eff} \times \boldsymbol{M} \tag{1.1.11}$$

where γ is the gyromagnetic ratio, $\boldsymbol{M} = -\gamma \boldsymbol{s}$ is the magnetization, and $\boldsymbol{H}_{eff} = -\frac{\delta \mathcal{F}}{\delta \boldsymbol{M}}$ is the effective magnetic field.

Equation (1.1.10) is the functional derivative form of the non-dissapative version of the Landau-Lifshitz equation. Now that we have this equation, we must inquire into what form to expect for the free energy $\mathcal{F}$.

1.1.2 The Landau free energy and symmetry

As stated above, the free energy $\mathcal{F}$ is a functional of the spin texture. The precise form of this functional dependence is that which reproduces the semi-classical physics of the ferromagnet. Note that $\mathcal{F}$ depends not only on $\boldsymbol{s}$, but also on its derivatives, e.g. $\nabla \boldsymbol{s}$. This can be seen from the exchange coupling term in the Hamiltonian (1.1.2). For simplicity, consider the spins along one partucular axis of the lattice. The exchange coupling is a sum of terms of the form

$$-J\boldsymbol{S}_i \cdot \boldsymbol{S}_{i+1} = \frac{J}{4}\left[(\boldsymbol{S}_i - \boldsymbol{S}_{i+1})^2 - (\boldsymbol{S}_i + \boldsymbol{S}_{i+1})^2\right] \tag{1.1.12}$$

$$\sim \frac{a^d J}{4}\left[(a\,\partial_x \boldsymbol{s})^2 - (2\boldsymbol{s})^2\right]\Big|_{x=x_i+\frac{a}{2}} \tag{1.1.13}$$

where a is the lattice spacing. Summing up over terms of this form results in an approximate integral over the $\boldsymbol{s}$ dependent expression in line (1.1.13) The approximate replacement of quantum spin operators with their coarse grained classical analogue, going from (1.1.12) to (1.1.13), is more accurate in the limit of large spin S per lattice site. This makes sense intuitively because the smallest spin, $S = \frac{1}{2}$ is simply a two state system, i.e. a highly quantum mechanical system; whereas, the larger S gets the closer the system gets to being

a macroscopic scale magnet, i.e. highly classical system.

More generally, in order to find a useful form for $\mathcal{F}$, we may need to expand in terms of $\boldsymbol{s}$ and its derivatives. The resulting truncated series can be simplified with symmetry considerations and fitted to experimental data.

As an example of how this works, we will consider a particularly simple, highly symmetric case. Suppose we have a magetic system which is translation invariant and rotation invariant, meaning that there are no prefered directions or locations. We require that the free energy satisfies these symmetry conditions. The free energy is an integral over a local free energy density which can be expressed as a series in s, i.e.

$$\mathcal{F} = \int d^d\boldsymbol{r} f \tag{1.1.14}$$

where

$$f = \sum_{nm\ell} a_{nm\ell}(\boldsymbol{r})(s^x)^n(s^y)^m(s^z)^\ell + \sum_{nm\ell\mu\alpha} b^{\mu\alpha}_{nm\ell}(\boldsymbol{r})(s^x)^n(s^y)^m(s^z)^\ell(\partial_\mu s^\alpha) + \dots \tag{1.1.15}$$

The first term is a series in components of s, the second term is a series over first order derivative terms, and the dots represent all terms involving higher order derivatives.

Translation invariance implies that the the coeficients in the series (1.1.15) must be position independent, such that the only position dependence in the free energy density comes from implicit dependence through $\boldsymbol{s}(\boldsymbol{r}, t)$.

For rotation invariance, we will assume that spin space and position space are independently invariant, meaning that the free energy does not change if one rotates all spins at the same time, nor does it change if one rotates the entire magnet in position space while keeping spin direction fixed. The former implies that the free energy can only depend on rotation invariant combinations of the components of $\boldsymbol{s}$, e.g. powers of $\boldsymbol{s} \cdot \boldsymbol{s}$. The spatial rotation invariance similarly requires invariant combinations of derivatives of the form $\sum_\mu \partial_\mu(\dots)\partial_\mu(\dots)$ or $\nabla^2(\dots)$.

With these constraints we have narrowed down the free energy density to

$$f = a_2|\boldsymbol{s}|^2 + a_4|\boldsymbol{s}|^4 + \cdots + c_2 \sum_{\mu} \partial_\mu \boldsymbol{s} \cdot \partial_\mu \boldsymbol{s} + \ldots \tag{1.1.16}$$

Note that all of the terms of the form $|\boldsymbol{s}|^n$ are irrelevant for the Landau-Lifshitz equation. The functional derivative of these terms is proportional $\boldsymbol{s}$, so they don't contribute to the cross product in equation (1.1.10). Instead these terms are important when minimizing the free energy and, as such, are useful modeling phase trasitions and qualitatively predicting how the magnetization strength behaves as a function of tempreature or magnetic field.

We can further simplify the free energy by focusing on the low energy, long wavelength behavior, such that only the lowest order derivatives are important. In this case the Landau-Lifshitz equation takes the form

$$\frac{d\boldsymbol{s}}{dt} = (-c_2 \nabla^2 \boldsymbol{s}) \times \boldsymbol{s} \tag{1.1.17}$$

If we relax the rotaional invariance condition, then the above equation will be modified by the addition of anisotropy terms.

1.1.3 Dissipation and the Landau-Lifshitz-Gilbert equation

Dissipation in magnetic dynamic occurs naturally as a result of coupling to the atomic lattice and the evironment around it. This coupling will transfer energy from the coarse grained spin texture to various energetic excitations such lattice vibrations, eddy currents, or microscopic spin waves [11] [12], which will result in an excited spin texture state decaying into the ground state if not sustained by external driving.

Due to the many competing mechanisms, the microscopic details of dissipation can be very complex, despite often having a fairly straightforeward consequence for macroscopic dynamics. As such, a phenological approach to modeling dissipation is often a good starting

point. To this end, one can add a damping term proportional to the derivative of the macroscopic dynamical variables to the equation of motion. To ensure that the damping term is incorporated properly, we can take the Lagrangian approach with a Rayleigh dissipation function, e.g.

$$\mathcal{R} = \frac{\alpha}{2} \int d^d \boldsymbol{r} \left(\frac{d\boldsymbol{s}}{dt} \right)^2 \tag{1.1.18}$$

where α is the Gilbert damping parameter. In terms of sperical coordinates of the spin texture,

$$\boldsymbol{s}(x) = s \begin{pmatrix} \cos\phi(x) \sin\theta(x) \\ \sin\phi(x) \sin\theta(x) \\ \cos\theta(x) \end{pmatrix} \tag{1.1.19}$$

the effective Lagrangian for the coarse grained spin texture is

$$\mathcal{L} = \int d^d \boldsymbol{r} \left[s(1 - \cos\theta) \frac{d\phi}{dt} \right] - \mathcal{F} \tag{1.1.20}$$

where $s = |\boldsymbol{s}|$ is the spin saturation density, which is typically taken to be constant. The kinetic-energy-like term is proportional to the rate of solid angle swept out by the spin dynamics, which can be seen by intgrating over time

$$\int dt \left[(1 - \cos\theta) \frac{d\phi}{dt} \right] = \int [1 - \cos\theta(\phi)] d\phi = \int \left[\int_0^{\theta(\phi)} d\theta \sin\theta \right] d\phi = \int d\Omega \tag{1.1.21}$$

The non-conservative form of the Euler-Lagrange field equations with a Rayleigh dissipation function are

$$\frac{d}{dt} \left(\frac{\delta \mathcal{L}}{\delta \dot{\psi}_i} \right) - \frac{\delta \mathcal{L}}{\delta \psi_i} + \frac{\delta \mathcal{R}}{\delta \dot{\psi}_i} = 0 \tag{1.1.22}$$

Here we have denoted time derivatives of the dynamical field variables with a dot. After some manipulation, these equations applied to the Lagrangian of equation (1.1.20) and the Rayleigh dissipation function of equation (1.1.18) result in the Landau-Lifshitz-Gilbert

equation

$$\frac{d\boldsymbol{s}}{dt} = \left(\frac{\delta \mathcal{F}}{\delta \boldsymbol{s}} - \alpha \frac{d\boldsymbol{s}}{dt}\right) \times \boldsymbol{s} \tag{1.1.23}$$

An equivalent form of this equation can be found by substituting the expression on the right hand side into the damping term derivative and applying the identity $\boldsymbol{s} \times (\dot{\boldsymbol{s}} \times \boldsymbol{s}) = (\boldsymbol{s} \cdot \boldsymbol{s})\dot{\boldsymbol{s}} - (\boldsymbol{s} \cdot \dot{\boldsymbol{s}})\boldsymbol{s} = s^2\, \dot{\boldsymbol{s}}$, resulting in

$$(1 + \alpha^2 s^2)\frac{d\boldsymbol{s}}{dt} = \left(\frac{\delta \mathcal{F}}{\delta \boldsymbol{s}} - \alpha \frac{\delta \mathcal{F}}{\delta \boldsymbol{s}} \times \boldsymbol{s}\right) \times \boldsymbol{s} \tag{1.1.24}$$

which (without the $\alpha^2 s^2$ term, which can often be neglected or simply absorbed into a redefinition of $\mathcal{F}$) is the original Landau-Lifshitz equation with dissipation.

1.1.4 Spin torques and boundary conditions

The ground state solution for the Landau-Lifshitz equation is often fairly simple, e.g. a uniform, symmetry-breaking magnetization, and this state is often achieved fairly quickly due to damping. One way to find more non-trivial behavior in the system is to to introduce some external driving. For a ferromagnetics, a non-equilibrium state can be produced by driving angular momentum into the system, resulting in additional spin torque terms in the equations of motion [13] [14].

The spin torques under consideration in this thesis are mainly those localized at the edges of effectively two dimensional systems. Such torques can be expressed as boundary conditions on the ferromagnet by setting the conserved spin current at the edge equal to the applied spin torque. For example, for the isotropic ferromagnet, the equation of motion (1.1.17) can be expressed as a continuity equation

$$\frac{d\boldsymbol{s}}{dt} = -\nabla \mathbf{J}_s \tag{1.1.25}$$

where the components of spin current tensor $\mathbf{J}_s$ for the s_α conserved current in the μ direction

are

$$J_s^{\mu\alpha} = c_2 \sum_{\beta\gamma} \epsilon_{\alpha\beta\gamma} s^\gamma \partial_\mu s^\beta \tag{1.1.26}$$

Thus the boundary conditions at an interface $\mathcal{I}$ with unit normal $\hat{n}$ would be

$$\mathbf{J}_s \cdot \hat{n}\Big|_{\mathcal{I}} = \boldsymbol{\tau}_{ext} \tag{1.1.27}$$

where $\boldsymbol{\tau}_{ext}$ is an externally driven torque acting on the magnetic intergface. The torque could be produced by e.g. spin Hall currents in Pt contacts [15] or tunned spin polarized edge currents on topological insulator surfaces [16].

In addition to these driving torques, one can also expect enhanced magnetic damping at the interface due to the connected material adding additional channels for dissipation. Thresulting localized damping can be accounted for with another Rayleigh dissipation for the boundary, which leads to a modification of equation (1.1.27) to the following form [17]

$$\mathbf{J}_s \cdot \hat{n}\Big|_{\mathcal{I}} = \boldsymbol{\tau}_{ext} - \frac{\hbar}{4\pi} G \boldsymbol{\omega} \tag{1.1.28}$$

where $\boldsymbol{\omega}$ is the angular frequency of rotation vector of the spin texture and G is the spin mixing conductance, which is a matrix in general.

1.2 Spin superfluids

Low dissipation spin currents come in many forms: ballistic transport, superfluid transport, equilibrium currents, and spin Hall effect currents. A more thorough overview of these different low dissipation spin currents can be found in Ref. [18]. Here we will focus mainly on spin superfluid transport.

Spin superfluids are predicted to occur in easy-plane ferromagnets. The easy plane ferromagnet has $U(1)$ rotational symmetry similar to that of traditional superfluids and superconductors, thus the name spin superfluid. As we shall see below, however, these phenomenon

are not identical; though they do exhibit some simularities in robustness of currents due to these currents being associate with topologically conserved winding about the axis of symmetry [19].

The Landau free energy of the easy-plane ferromagnet in a magnetic field parallel to the anisotropy axis is

$$\mathcal{F} = \int d\boldsymbol{r} \left[\frac{A}{2}(\nabla \boldsymbol{n})^2 + \frac{K}{2} n_z^2 + h n_z \right] \tag{1.2.1}$$

where $\boldsymbol{n} = \boldsymbol{s}/s$ is the normalized spin texture, A is the spin stiffness, K is the anisotropy parameter, and h parameterizes the magnetic field strength. In the absense of a magnetic field, the anisotropy term pins the ground state into the xy-plane. Compared to the fully $O(3)$ symmetric case of equation (1.1.16), the addition of the anisotropy term reduces the spin space symmetry to just $U(1)$ rotational symmetry about the z-axis. The Landau-Lifshitz-Gilbert equations for the spin texture in terms of the standard spherical angle ϕ and θ parameterization are [20]

$$s\,\partial_t \theta - s\alpha \sin\theta\,\partial_t \phi = -A \frac{\nabla(\sin^2\theta\,\nabla\phi)}{\sin\theta} \tag{1.2.2}$$

$$s \sin\theta\,\partial_t \phi + s\alpha\,\partial_t \theta = A\nabla^2\theta - \frac{A}{2}(\nabla\phi)^2 \sin 2\theta + \frac{K}{2}\sin 2\theta + h\sin\theta \tag{1.2.3}$$

This form is a common starting point for analytical study. These equations can be solved for soliton and wave solutions via the method of inverse scattering transform [21]. In order to illustrate the analogy to superfluidity, we rewrite these equations in terms of the conserved (in absence of damping) out of plane component, n_z, giving

$$-s\,\partial_t n_z - s\alpha(1-n_z^2)\partial_t\phi = -A\nabla[(1-n_z^2)\nabla\phi] \tag{1.2.4}$$

$$s\sqrt{1-n_z^2}\,\partial_t\phi + s\alpha\frac{\partial_t n_z}{\sqrt{1-n_z^2}} = A\nabla\left(\frac{\nabla n_z}{\sqrt{1-n_z^2}}\right) + [K - A(\nabla\phi)^2] n_z\sqrt{1-n_z^2} + h\sqrt{1-n_z^2} \tag{1.2.5}$$

Spin superfluid transport is often considered in the limit $n_z \ll 1$ so as to ignore the possibility

of phase slips, which is the phenomenon of loss of winding number about the z-axis via the spin texture "slipping" over the north pole ($\theta = 0$) due to quantum or thermal fluctuations. Driving a spin superfluid through the system can induce an out of plane component of the spin texture which is approximately proportional to the driving strength in the low bias, linear response regime. Thus, in assuming $n_z \ll 1$, we are typically assuming a low driving regime[2]. Under this approximation, we drop squared and higher order terms of n_z and its derivatives, resulting in a much simpler form for the Landau-Lifshitz-Gilbert equations

$$-s\,\partial_t n_z - s\alpha\partial_t\phi \approx -A\nabla^2\phi \tag{1.2.6}$$

$$s\,\partial_t\phi + s\alpha\partial_t n_z \approx A\nabla^2 n_z + [K + h - A(\nabla\phi)^2]n_z \tag{1.2.7}$$

This is the form where the similarity to tranditional superfluidity is most apparent. The spin superfluid response to boundary torques is studied under this approximation in Ref. [15]. The $n_z \ll 1$ approximation is not used in Ref. [20], however, where the authors instead opt for neglecting Gilbert damping, which mainly causes an algebraic decay of the spin superfluid current without significantly impacting other qualitative features of the spin superfluid.

1.3 Comparison to traditional superconductivity

Now let us turn to the traditional superconductivity for a brief comparison. Superconductivity and superfluidity can arise in Fermi liquids at low temperatures. Due to effectively attractive interactions, often mediated by phonons in the case of an electron fermi sea, the Fermi liquid develops an instability to a zero-viscosity ground state which can in some ways be thought of as a delocalized Bose-Einstein condensation of bosonic composite quasiparticles called cooper pairs. The system develops a macroscopically large filling of the cooper pair ground state, which allows the wavefunction of this state to be treated effectively as a

[2]An exeption can occur when roughly equal torques on opposite ends of the ferromagnet work against eachother, inducing greater tension in the spin texture through winding, but not inducing significant out of plane spin polarization.

classical field. This classical field plays the role of the order parameter in the Landau free energy

$$\mathcal{F}_{SC} = \int d\boldsymbol{r} \left[a_1 (\nabla \Psi)^2 + a_2 |\Psi|^2 + a_3 |\Psi|^4 \right] \tag{1.3.1}$$

Note that the $U(1)$ symmetry in this case comes from the invariance under a constant phase shift of the complex valued order parameter,

$$\Psi(\boldsymbol{r}, t) \;\longrightarrow\; \Psi(\boldsymbol{r}, t)\, e^{i\delta} \tag{1.3.2}$$

Because the order parameter is simply a macroscopically filled wavefunction, we can model it's dynamics with a Schrödinger equation

$$i\hbar\, \partial_t \Psi = -\frac{\hbar^2}{2m} \left(\nabla - \frac{iq}{\hbar c} \boldsymbol{A} \right)^2 \Psi + qV\Psi \tag{1.3.3}$$

where m and q are effective mass and effective charge for the cooper pair quasiparticles, and $\boldsymbol{A}$ and V are vector and scalar potentials. For the sake of comparison to the spin superfluid equations (1.2.6) and (1.2.7), we expand the superfluid order parameter in terms of its phase and modulus, $\Psi = \Psi_0\, e^{i\varphi}$, and separate the real and imaginary parts of the resulting equation to get

$$\hbar\, \partial_t \Psi_0 = -\frac{\hbar^2}{2m} (\Psi_0 \nabla^2 \varphi + 2 \nabla \Psi_0 \cdot \nabla \varphi) \tag{1.3.4}$$

$$-\hbar\, \Psi_0\, \partial_t \varphi = -\frac{\hbar^2}{2m} [\nabla^2 \Psi_0 - \Psi_0 (\nabla \varphi)^2] + qV\Psi_0 \tag{1.3.5}$$

where for simplicity we have dropped the vector potential. Now let us compare these equations with equations (1.2.6) and (1.2.7).

The most glaring difference between the spin superfluid and superconductor equations of motion is the presence of dissipation in the former. However, this doesn't kill the anology just yet. For superfluids some degree of dissipation is not completely unheard of, as dissipation has been observed in persistent supercurrents of atomic Bose-Einstein condensates [22], where

the supercurrent decays in discrete jumps due to vortex phase slips. On the other hand, some magnetic materials, such as Yittrium-Iron-Garnate (YIG) have extremely low Gilbert damping [23].

If we neglect damping and spatial varations in n_z and Ψ_0, then the equation become effectively identical. For this case, the superconductor phase rate of change is determined by the local scalar potential. In a sense one can think of the magnetic field playing the role of a (shifted) chemical potential for the spin superfluid.

Without damping equation (1.2.6) is a continuity equation for a conserved spin density with an associated current of

$$\boldsymbol{J} = -A\nabla\phi \tag{1.3.6}$$

For the superconductor, equation (1.3.4) bears some simularity to a continuity equation, but of course Ψ_0 is not conserved. Instead, the particle density, Ψ_0^2, is conserved and satisfies the continuity equation

$$\partial_t|\Psi|^2 = -\nabla\cdot\boldsymbol{J}_{SC} \tag{1.3.7}$$

where the current can be found by evaluating the time derivative on the left hand side with the equation of motion to get

$$\boldsymbol{J}_{SC} = \frac{\hbar}{2m}(\Psi^*\nabla\Psi - \Psi\nabla\Psi^*) = \frac{\hbar}{m}\Psi_0^2\,\nabla\varphi \tag{1.3.8}$$

Thus for both systems, the superfluid dynamics is intricately tied to the $U(1)$ winding angle in both space and time, with currrents proportional to the winding gradient and a local "potential" proportional to the local winding rate. As we shall see in later chapters, the analogy between these two systems holds in some other contexts as well, and becomes quite useful, as one may simply reduce the ferromagnet model to a recongizable form and then translate results directly from the theory of superconductivity. However, we shall also see that the analogy breaks down for the ferromagnet in the presence of strong external driving, and this is the regime in which distinguishing physics can arise, such as stationary

solitons and persistent chaos.

Chapter 2

Easy-Plane Magnetic Strip as a Long Josephson Junction

Spin-torque-biased magnetic dynamics in an easy-plane ferromagnet (EPF) is theoretically studied in the presence of a weak in-plane anisotropy. While this anisotropy spoils U(1) symmetry thereby quenching the conventional spin superfluidity, we show that the system instead realizes a close analog of a long Josephson junction (LJJ) model. The traditional magnetic-field and electric-current controls of the latter map respectively onto the symmetric and antisymmetric combinations of the out-of-plane spin torques applied at the ends of the magnetic strip. This suggests an alternative route towards realizations of superfluid-like transport phenomena in insulating magnetic systems. We study spin-torque-biased phase diagram, providing analytical solution for static multidomain phases in the EPF. We adapt an existing self-consistency method for the LJJ to develop an approximate solution for the EPF dynamics. The LJJ-EPF mapping has potential for producing applications with superconductor-based circuit functionality at elevated temperatures. The results apply equally to antiferromagnets with suitable effective free energy in terms of the Néel order instead of magnetization.

2.1 Introduction

It has been suggested [18,24,25] that insulating thin-film easy-plane ferromagnets (EPF) can exhibit features of superfluid spin transport, which is attractive for spintronics applications, due to low dissipation and long-ranged signal propagation [15, 26]. However, complications can arise in that spin supercurrents, i.e., spin transport with topologically-suppressed dissipation [24], can be inhibited in an EPF by the presence of magnetic anisotropy within the easy-plane. This spoils the requisite $U(1)$ symmetry and pins the magnetization along a particular direction. Such symmetry-breaking anisotropies always exist in real materials, due to, e.g., underlying crystal symmetries or shape anisotropy, demoting the spin superfluid analogy to an imperfect one. Potential signatures of spin superfluids were recently observed in Refs. [27, 28], so measuring effects of anisotropy may be viable in the near future.

In this Letter, departing from the previous view of the EPF with in-plane anisotropy as a defective spin superfluid, we propose a description as a magnetic analog of a long Josephson junction (LJJ), which consists of two superconductors sandwiching a thin insulating layer [29]. This incorporates the in-plane anisotropy as a natural and potentially desirable ingredient. Specifically, we consider the magnetic dynamics of the EPF driven by the out-of-plane spin torques exerted at its ends. The mapping between EPF and LJJ represents a key result of the paper: Domain walls in the former correspond to phase vortices in the latter, and symmetric and antisymmetric combinations of the spin torques in the former correspond to the magnetic-field and electric-current controls of the latter. We find a nonequilibrium phase diagram of the EPF, including exact static solutions and approximate dynamic solutions. To this end, we adapt the stability analysis of the static sine-Gordon equation presented in Refs. [30, 31], along with dynamic solutions of Ref. [32].

In the following, we construct the spin-torque-biased phase diagram, in which the multi-vortex stationary states of the LJJ get mapped onto multi-magnetic-domain-wall stationary states in the EPF. The mapping from the equations of motion (EoM) for the LJJ to the

Landau-Lifshitz-Gilbert equations for the EPF is exact for static cases, thus giving the full analytical solution for static multidomain phases in the EPF. For dynamic cases, the EoM for the EPF differ from those of the LJJ in that the dissipative leakage at the boundaries due to spin pumping [33] must be accounted for; however, techniques for approximating the dynamical solutions in LJJ's can be carried over to the EPF with minor adjustments. As an example, we develop an approximate analytical solution for the EPF dynamics by adapting an existing self-consistent method for the LJJ [32].

2.2 Magnetic model

In this Letter, we show that a magnetic strip connected to spin-injection leads bears close analogy to a LJJ. We illustrate this by considering a simple structure depicted in Fig. 2.1(a). An insulating EPF of length $2L$ is subjected to spin torques $\tau_{r,l}$ applied at its left (right) interface. The underlying spin currents are injected via the spin Hall effect [34] with spins oriented out of the magnetic easy (xy) plane. The system is similar to the EPF thin-film junction of Ref. [15] but with the addition of a small in-plane anisotropy $K' \ll K$. Our magnetic free energy is given by $F[\phi, n] = \frac{1}{2}\int d^2r \left[A(\partial_{\mathbf{r}}\phi)^2 + Kn^2 + K'\sin^2\phi\right]$, where $\phi(\mathbf{r}, t)$ is the azimuthal angle of the directional (unit-vector) order parameter $\mathbf{n}(\mathbf{r}, t) \equiv (\sqrt{1-n^2}\cos\phi, \sqrt{1-n^2}\sin\phi, n)$ Its z projection, $n(\mathbf{r}, t)$, parametrizes the generator of spin rotations in the plane, which thus dictates the Poisson bracket $s\{\phi, n\} = \delta(\mathbf{r}-\mathbf{r}')$ and establishes the canonical conjugacy of the pair (ϕ, sn) [35]. s is the saturation spin density and A is the order-parameter stiffness. The hard-z-axis anisotropy $K \gg K'$ keeps the magnetization dynamics predominantly near the xy plane, which allows us to neglect the gradient terms involving n. The ground-state orientation is collinear with the x axis, according to the magnetic anisotropy $\propto K'$, dictating the presence of metastable domain-wall textures, as depicted in Fig. 2.1(a).

The dissipation associated with the magnetization dynamics is introduced in the conventional Gilbert-damping form [36], which for our easy-plane dynamics reduces to the Rayleigh

dissipation function (per unit area) of $R = \alpha_d s(\partial_t\phi)^2/2$, parametrized by a damping constant α_d. We assume the low-bias regime, such that $|\partial_{\mathbf{r}}\phi| \ll \sqrt{K/A}$ (the Landau criterion for the stability of planar textures [24].), so as to prevent significant departures of the magnetization away from the easy plane. Thermal nucleation of magnetic vortices responsible for superfluid-like phase slips [37] is likewise neglected.

Putting these ingredients together, we obtain the EoM, $s\partial_t\phi = Kn$ and $s\partial_t n = A\partial_{\mathbf{r}}^2\phi - \frac{K'}{2}\sin 2\phi - \alpha_d s\partial_t\phi$. Boundary conditions are set by spin injection/pumping. The total out-of-plane spin-current densities through the right (left) interface, in the positive x direction are [15]

$$j_{r,l}^{(s)} = \mp\frac{g}{4\pi}\left[\mu_{r,l}^{(s)} - \hbar\partial_t\phi\right], \tag{2.2.1}$$

where g is the (real part of) the spin-mixing conductance per unit length of the interface and $\mu^{(s)}$ is the out-of-plane spin accumulation near the interface, which is induced by the spin Hall effect in the metal contacts. For the sake of simplicity, we assume the spin-mixing conductances to be the same for both interfaces. Recognizing the stiffness $\propto A$ term in the EoM as stemming from the bulk spin current $\mathbf{j}^{(s)} = -A\partial_{\mathbf{r}}\phi$, so that $s\partial_t n = -\partial_{\mathbf{r}}\cdot\mathbf{j}^{(s)} + \ldots$ [24], we invoke spin continuity to obtain the boundary conditions:

$$-A\partial_x\phi(\pm L, t) = j_{r,l}^{(s)} = \tau_{r,l} \pm \gamma\partial_t\phi(\pm L, t)\,. \tag{2.2.2}$$

Here, $\tau_{r,l} \equiv \mp\frac{g}{4\pi}\mu_{r,l}^{(s)} = \frac{\hbar\tan\theta_{\rm SH}}{2e}j_{r,l}$ is the spin Hall torque at the left (right) interface generated by an electric current density $j_{r,l}$ flowing in the y direction through the metal leads. $\theta_{\rm SH}$ is the effective spin Hall angle of the interfaces [38]. $\gamma \equiv \hbar g/4\pi$ parametrizes spin pumping out of the ferromagnet by the magnetic dynamics [33].

Eliminating n from the EoM and applying the substitution

$$\tilde{\phi} = 2\phi\,, \tag{2.2.3}$$

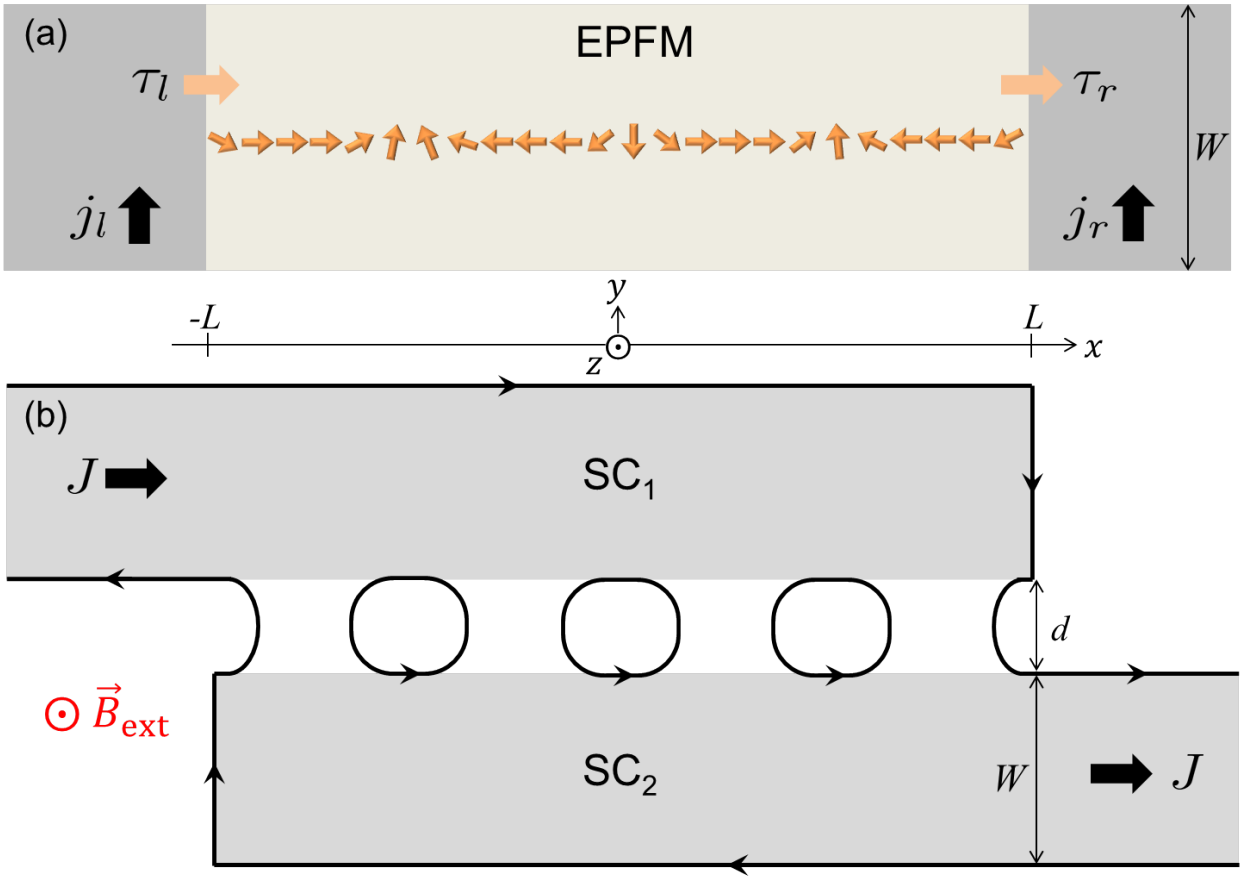

Figure 2.1: (a) EPF with spin injection from metal contacts on two side. The spin polarization of the current is along the z axis, while the spin-current flow is oriented along the x axis. The ferromagnet is sufficiently narrow in the transverse dimensions to treat it as quasi-one-dimensional. (b) Diagram of the inline LJJ, with W much smaller than L as well as the depth of the structure in the z direction. We assume two conventional superconductors (SC) much larger than the London penetration depth in all dimensions. The magnetic-field screening currents as well as the circulating vortices are schematically depicted with black oriented lines. The vortices in the junction map onto the domain walls depicted in (a).

we arrive at the damped sine-Gordon equation:

$$\partial_x^2\tilde{\phi} = \frac{\partial_t^2\tilde{\phi}}{u^2} + \frac{\sin\tilde{\phi}}{\lambda^2} + \beta_d\partial_t\tilde{\phi}\,, \tag{2.2.4}$$

with the wave speed $u = \sqrt{AK}/s$, characteristic domain-wall width $\lambda = \sqrt{A/K'}$, and damping constant $\beta_d = \alpha_d s/A$. This equation admits a solution of an isolated domain wall as well as low-amplitude spin-wave solutions which obey the massive Klein-Gordon equation, with the mass proportional to K'. In the large spin-current limit, so that $|\partial_{\mathbf{r}}\phi| \gg 1/\lambda$, the excitations become approximately massless. In this (linearly-dispersing) limit, the system approaches the behavior of the EPF without in-plane anisotropy, thus allowing for states that closely resemble the spin superfluid of Ref. [15]. In the small spin-current regime, on the contrary, the steady state configuration is static, laking the aforementioned spin-superfluid dynamics, but the analogy to LJJ nevertheless holds.

The damped sine-Gordon equation has found application in a number of disciplines [39]. The equation is commonly studied in relation to its physical realizations in coupled series of pendulums and long Josephson Junctions. Below we exploit some relevant results of the latter.

2.3 Relation to long Josephson junctions

It is instructive to recall the dynamics of the inline configuration of a LJJ [40,41], a diagram of which is depicted in Figure 2.1(b). A Josephson junction permits coherent supercurrent tunneling through the insulating region up to a critical current density j_c, which depends on the tunneling strength and the superfluid density in the superconductor. In the presence of a magnetic field $\mathbf{B} = B(x)\mathbf{z}$ inside of the junction, we can choose a gauge $\mathbf{A} = A(x,y)\mathbf{x}$, so that $B = -\partial_y A$. The DC Josephson relation for the tunneling current flowing from SC_1 to SC_2 is

$$j = j_c \sin\vartheta + gV\,, \tag{2.3.1}$$

where $\vartheta(x) = \theta_1 - \theta_2$ is the superconducting phase difference across the junction, and we also added the normal current component proportional to the conductance (per unit area) g and the local voltage $V(x) = V_1 - V_2$ across the junction. $B(x)$ satisfies the Ampère-Maxwell equation

$$\partial_x B = \frac{4\pi}{c} j + \frac{\varepsilon}{c} \partial_t E \,, \tag{2.3.2}$$

where $E = -\mathbf{E} \cdot \mathbf{y} = V/d$ is the electric field in and ε the permittivity of the insulating region.

Next, we invoke the superconducting phase evolution equation ($e > 0$)

$$V = \frac{\hbar}{2e} \partial_t \vartheta \tag{2.3.3}$$

and the relation $\partial_x \theta = -(2e/\hbar c) A$ well inside of the superconducting regions (on the scale of the London penetration depth λ_L), which leads to

$$B = \frac{A_2 - A_1}{d + 2\lambda_L} = \frac{\hbar c}{2e(d + 2\lambda_L)} \partial_x \vartheta \,. \tag{2.3.4}$$

Putting Eqs. (2.3.1)-(2.3.4) together, we reproduce the damped sine-Gordon equation (2.2.4), thus identifying the Swihart velocity $u = c\sqrt{\frac{d}{\varepsilon(d+2\lambda_L)}}$, the Josephson penetration depth $\lambda_J = c\sqrt{\frac{\hbar}{8\pi e(d+2\lambda_L) j_c}}$, and the damping parameter $\beta_d = \frac{4\pi g(d+2\lambda_L)}{c^2}$.

The boundary conditions are obtained from Eq. (2.3.4) by noting that

$$B(\pm L) = B_{\text{ext}} \pm \frac{2\pi}{c} J \,, \tag{2.3.5}$$

where B_{ext} is the externally applied field in the z direction and J is the applied current through the system, per unit of length in the z direction. Comparing this with Eq. (2.2.2), we see that the symmetric (antisymmetric) combination of the torques, $\tau_r \pm \tau_l$, realizes the

effect of the external field B_{ext} (applied current J), in the mapping from the LJJ to the EPF:

$$\frac{\tau_{r,l}}{A} \rightleftharpoons -\frac{e}{\hbar c}(d + 2\lambda_L)\left(B_{\text{ext}} \pm \frac{2\pi}{c}J\right) . \tag{2.3.6}$$

The EoM of the LJJ and anisotropic EPF systems differ only in the addition of the boundary spin pumping term, $\gamma\partial_t\phi$, in Eq. (2.2.2). If spin pumping is negligible, e.g. time-independent solutions, the two problems are equivalent. Having an exact mapping between the models of the LJJ and EPF for time-independent solutions allows the equilibrium stability analysis of Ref. [30] to carry over. The close analogy of the EPF system to the thoroughly studied LJJ model allows us to immediately draw several conclusions about the static solutions. The substitution (2.2.3) indicates that a 2π phase vortex in the LJJ model corresponds to a domain wall (π rotation) in the EPF. In particular, the symmetric torque $\tau_r = \tau_l$ injects static domain-wall textures into the EPF, which in the LJJ corresponds to the external field B_{ext} producing a static multivortex configuration. The number of stable domain walls is dependent on the boundary conditions and the solution for a given boundary condition can be multivalued, resulting in hysteretic effects. The multivalued solutions are dependent on the length of the system, in units of λ. Figure 2.2 shows the regions of stability for p-vortex equilibrium solutions for the case of $L = \lambda$. The stability regions have greater overlap in the limit of large L/λ, and in this limit the edge of the $p > 0$ stability region asymptotically approaches the zero bias point as $\sim e^{-L/p\lambda}$. See Ref. [30] for the analytic equations for computing the phase boundaries.

2.4 Analytic equilibrium solutions

Using the stable solutions of the LJJ problem studied in Ref. [30], we map back to the EPF to find the static domain-wall configurations. We give the form of the $\phi(x)$ solutions after mapping to the EPF, as well as some general remarks, and refer to Refs. [30, 31] for further details. Similar solutions were recently found for the one terminal case in Ref. [42]. From

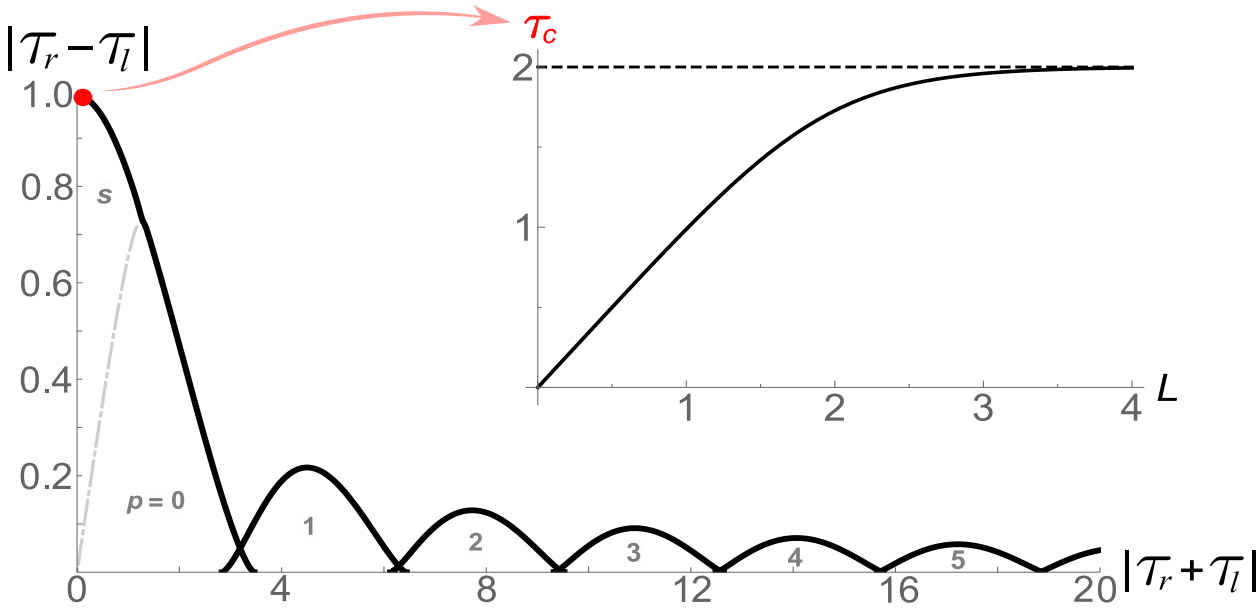

Figure 2.2: The regions of stability for equalibium p-vortex solutions of the LJJ boundary-value problem, for $L/\lambda = 1$. The spin torques $\tau_{r,l}$ are in units of A/λ. Overlapping regions can have either solution. Outside of these regions, i.e., in the high $|\tau_r - \tau_l|$ limit, there are no stable time-independent solutions. Inset: The dependence of the critical torque τ_c, for which $\tau_r + \tau_l = 0$, on the length L in units of λ.

the p-vortex LJJ solutions, we find p-domain-wall solutions in the EPF have the form

$$\phi(x) = \eta \begin{cases} \frac{\pi}{2}(p-1) + \mathrm{am}\left(\xi + K(k), k\right) , & \text{for } p \text{ even} \\ \frac{\pi}{2}p + \mathrm{am}\left(\xi, k\right) , & \text{for } p \text{ odd} \end{cases} , \tag{2.4.1}$$

where $\xi = \frac{x}{k\lambda} + \alpha$, and $\eta = \pm 1$ for $\tau_r + \tau_l \lessgtr 0$. Here, α and k are parameters determined by the boundary conditions, and $\mathrm{am}(u)$ and $K(u)$ are the Jacobi amplitude function and complete elliptic integral of the first kind, respectively.

The zero-domain-wall region includes a portion, separated by the gray line and labeled by s in Fig. 2.2, in which Eq. (2.4.1) no longer holds. The solution in the s region has the form

$$\phi(x) = \zeta \cos^{-1}\left[k \frac{\mathrm{cn}\left(x/\lambda + \beta\right)}{\mathrm{dn}\left(x/\lambda + \beta\right)}\right] , \tag{2.4.2}$$

where k and β are again determined by the boundary conditions, $\zeta = \pm 1$ for $\tau_r - \tau_l \lessgtr 0$,

and $\mathrm{cn}(u)$ and $\mathrm{dm}(u)$ are the Jacobi elliptic cosine and delta amplitude, respectively. In the case of $L = \infty$, the s crossover line becomes a phase-transition line from a no-domain-wall phase to a many-domain-wall phase, but away from this limit the crossover from s to $p = 0$ is smoothed out by finite-size effects and no phase transition takes place.

In the special case of perfectly asymmetric boundary conditions, i.e., $\tau_r = -\tau_l$, the equilibrium solution is given by Eq. (2.4.2) with $\beta = 0$, up to the critical value of $|\tau_r - \tau_l| \to \tau_c$. This critical asymmetric torque τ_c is analogous to the critical current J_c in the LJJ model, with, as shown in the Fig. 2.2 inset, its value depending on the normalized length of the system. τ_c approaches A/λ asymptotically as $L \to \infty$ and diminishes as $\tau_c = LK'$ for $L \to 0$. For yttrium iron garnet, $A \sim 10^{-11}$ J/m^2, so the saturated critical torque (per unit area), corresponding to $\lambda \sim 100$ nm would be $A/\lambda \sim 10^{-4}$ J/m^2. Using the spin Hall angle $\theta_{\mathrm{SH}} \sim 0.1$, the corresponding electrical current density needed at the metallic contacts in order to approach τ_c is of order 10^{12} A/m^2, which is high but feasible.

2.5 Dynamic solutions

Here, inspired by the LJJ analogy, we apply a method similar to that of Ref. [32] in finding an approximate dynamic, spin-propagating solution for the EPF EoM, Eq. (2.2.4) with boundary conditions (2.2.2). To simplify the discussion, we adopt dimensionless notation, such that $A = u = \lambda = 1$. It is natural to start with a trial solution of the form $\tilde{\phi}(x,t) = \Omega t + f(x) + \epsilon(x,t)$. where $\epsilon(x,t)$ is a small periodic function with the to-be-determined period $T = 2\pi/\Omega$ and with zero time average, and $f(x)$ is a to-be-determined time-independent function. We consider the weak in-plane anisotropy limit for which $\epsilon(x,t) \ll 1$. The boundary conditions are

$$-\partial_x f(\pm L) = 2\tau_{r,l} \pm \gamma\Omega \tag{2.5.1}$$

and

$$\partial_x \epsilon(\pm L, t) = 0\,, \tag{2.5.2}$$

where we discard the boundary term $\gamma\partial_t\epsilon$ by considering the $\gamma \ll 1$ limit[1]. Plugging the trial solution into Eq. (2.2.4) and averaging over the period T, denoted by $\langle \dots \rangle_T$, we get the time-independent equation $\partial_x^2 f = \beta_d\Omega + \langle \sin\tilde{\phi} \rangle_T$. Integrating and applying the boundary conditions, we find the self-consistency equation

$$\begin{aligned} f(x) = \int_{-L}^{x} dx_1 \int_{-L}^{x_1} dx_2 \left[\beta_d\Omega + \langle \sin\tilde{\phi} \rangle_T(x_2)\right] \\ - (2\tau_l - \gamma\Omega)x\,, \end{aligned} \tag{2.5.3}$$

with the constraint

$$\int_{-L}^{L} dx \langle \sin\tilde{\phi} \rangle_T = 2(\tau_l - \tau_r - \gamma\Omega - L\beta_d\Omega)\,. \tag{2.5.4}$$

Note that the integral on the right-hand side of Eq. (2.5.3) depends on both $f(x)$ and $\epsilon(x,t)$ through $\tilde{\phi}$.

For the time-dependent part of the solution, the dominant contribution is harmonic in Ωt and obeys $\partial_x^2\epsilon - \partial_t^2\epsilon - \beta_d\partial_t\epsilon = \sin(\Omega t + f)$. The solution satisfying the boundary conditions (2.5.2) is then readily found to be

$$\begin{aligned} \epsilon(x,t) = \mathrm{Im}\Big(\frac{e^{i\Omega t}}{2i\omega}\big[e^{i\omega x}F^-(x) - e^{-i\omega x}F^+(x) \\ + A\cos(\omega x + \omega L)\big]\Big)\,, \end{aligned} \tag{2.5.5}$$

where $A = i\left[e^{i\omega L}F^-(L) + e^{-i\omega L}F^+(L)\right]/\sin(2\omega L)$, $\omega^2 = \Omega^2 - i\beta_d\Omega$, and the functions $F^{\pm}(x) = \int_{-L}^{x} dx_1\, e^{if(x_1)\pm i\omega x_1}$. Equations (2.5.3), (2.5.4), and (2.5.5) form a system of coupled integral equations for $f(x)$, Ω, and $\epsilon(x,t)$. Approximate solutions can be found iteratively by starting with, for example, $\langle \sin\tilde{\phi} \rangle_T^{(0)} = 0$, which implies $f^{(0)}(x) = \beta_d\Omega^{(0)}(x+L)^2/2 - (2\tau_l - \gamma\Omega^{(0)})(x+L)$, with $\Omega^{(0)} = (\tau_l - \tau_r)/(L\beta_d + \gamma)$. This agrees with the XY-model solution

[1]This approximation is made to simplify the discussion. Without this constraint, ϵ satisfies $\partial_x\epsilon \pm \gamma\partial_t\epsilon = 0$ at the right (left) boundary, and the resulting solution is similar but lengthier than the one presented here.

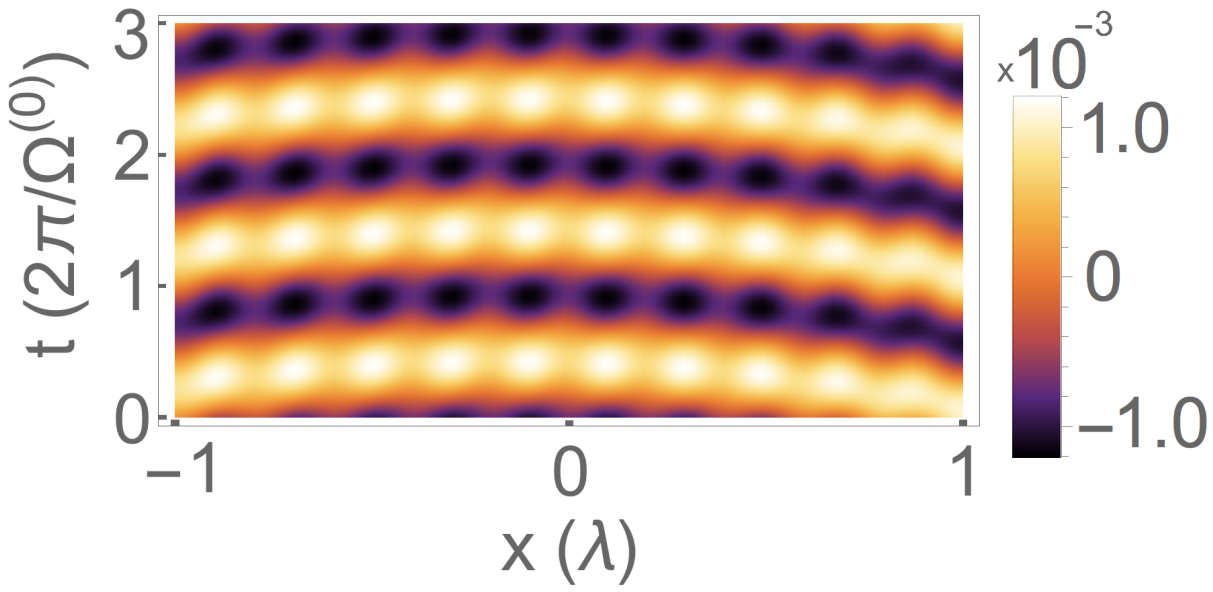

Figure 2.3: Plot of the approximate modulation of the superfluid phase solution, $\epsilon^{(0)}(x,t)$, resulting from a weak in-plane anisotropy, with $L = 1$, $\beta_d = 0.1$, $\gamma = 0.01$, $\tau_l = 1.5$, and $\tau_r = -2$.

[2] of Ref. [26]. This intermediate solution can be plugged into Eq. (2.5.5) to get $\epsilon^{(0)}(x,t)$, an example of which is plotted in Fig. 2.3. These in turn can be used to evaluate $\left\langle \sin\tilde{\phi} \right\rangle_T^{(1)}$ for generating a new set $f^{(1)}(x)$, $\Omega^{(1)}$, and $\epsilon^{(1)}(x,t)$, and so on.

Note that the frequency of oscillation of the superfluid phase, Ω, is modulated as a function of EPF length, L, as a result of the in-plane anisotropy. This is seen through the dependence of Ω on the integral on the right-hand side of Eq. (2.5.4). The predicted dependence of Ω on L can in practice provide a useful experimental probe of the underlying physics.

Because the transmitted superfluid current is dependent on Ω, this modulation effect could in principle be measured by injecting sufficient spin current ($\tau \gtrsim A/\lambda$) into insulating thin film ferromagnets of variable length and measuring the inverse spin Hall effect on the opposite end, using similar methods to those discussed in Refs. [43, 44].

[2]Note that our definitions of Ω and L, chosen to more closely adhere to the LJJ references, differ from Ref. [26] by a factor of 2.

2.6 Discussion

Given that Josephson junction systems have many potential uses as computing circuit elements, e.g. as a transistor [45] or memristor [46], the close analogy between the EPF and LJJ suggests a potential for similar spintronic applications which could operate in much the same manner as the proposed LJJ devices, due to the vortex/domain-wall corespondence between the systems, thus taking advantage of the history-dependence and information storage potential of the domain walls. Such EPF-based devices would use currents through the spin Hall contacts as inputs and would produce an output either by measuring the inverse spin Hall voltages resulting from a change of state, e.g. injection of a domain wall, or by directly reading the number of domain walls, which is possible with e.g. the magneto-optical Kerr effect [47] or magnetic force microscopy [48]. Using EPF-based spintronics devices instead of LJJ-based superconducting devices as building blocks of circuit elements could have practical advantages, e.g. the relevant physics such as the spin Hall torque [49] being able to operate at room temperature and the use of eletrical current inputs instead of precisely controlled magnetic fields to control the state of the system.

We wish to thank the anonymous referees, whose comments and questions led to the significant improvement of the Letter. This work was supported by the Army Research Office under Contract No. W911NF-14-1-0016.

Chapter 3

Self-stabilizing spin superfluids

Spin superfluidity is sought after as a potential route to long-range spin transport. In magnetic systems, it refers to exchange-mediated spin transport by a spin texture with robust topological winding. Its signatures have recently been observed in antiferromagnets which are nearly free of dipolar interaction. However in ferromagnets, realization of spin superfluid remains a challenge. Using micromagnetic simulations, we observe spin superfluidity in extended thin ferromagnetic films. We uncover a surprising two-fluid state, in which spin superfluidity co-exists with and is stabilized by spin waves, as well as a soliton-screened superfluid at high biases. Both states are associated with distinct spin texture reconstructions near the spin injection region and maintain superfluidity above the expected Landau instability. The results of this study advance our understanding of spin superfluidity and provide guidance for future experiments.

3.1 Introduction

The field of magnon-spintronics opens new possibilities for energy-efficient information storage, transport, and processing. Achieving low-dissipation long-range spin transport is one of the main goals of spintronics research. In magnetic insulators, spin currents are carried by spin waves, free of undesired electric currents [50]. Despite low damping, however, spin

waves exhibit exponential decay over distances that can be short at high frequencies.

The bosonic nature of spin excitations in ordered magnetic materials can benefit from magnon-magnon interactions and the ensuing coherence. Bose-Einstein condensation of magnons, that was experimentally observed in various systems [51–55], is a notable example. Another phenomenon characteristic of bosonic systems is superfluidity; resistance-free charge transport in superconductors and viscosity-free mass transport in superfluid helium are some prominent examples [56–58]. Early works by Halperin and Hohenberg proposed a hydrodynamic theory of magnons [59], which is closely related to superfluidity. Spin superfluids can be induced in easy-plane ordered spin systems; upon non-equilibrium spin injection with perpendicular-to-plane polarization, a global texture of magnetic order parameter develops in the form of a topologically robust winding spiral (Fig. 1a). The order parameter precesses coherently in time at low frequencies and transports spin current over macroscopic distances [60] with a small [61–64] but finite dissipation rate. The spin current shows power-low spatial decay, thus enabling long-range spin transport beyond the mean free path of ordinary spin waves. While spin superfluidity bears similarities to mass superfluidity (equation of spin motion resembles Josephson relations for superfluidity, superflow is characterized by the gradient of the phase), it must be stressed that this phenomenon is not truly dissipationless.

Recently, signatures of spin superfluidity have been experimentally observed in antiferromagnetic spin systems [65, 66]. A realization of spin superfluid in ferromagnets remains an unsolved challenge. Previous theoretical works have revealed the potential of superfluid spin transport [15, 44, 60, 67–74] for spintronics applications but have not systematically studied the role of dipolar interactions. Numerical calculations in Ref. [75] for micrometer-scale thin-film ferromagnets have demonstrated that dipolar interaction can destroy the spin superfluid; recent numerical simulations in thin ferromagnetic stripes [69, 70] have shown that spin superfluidity can be achieved despite the dipolar interaction, sparking a discussion on experimental feasibility of such states.

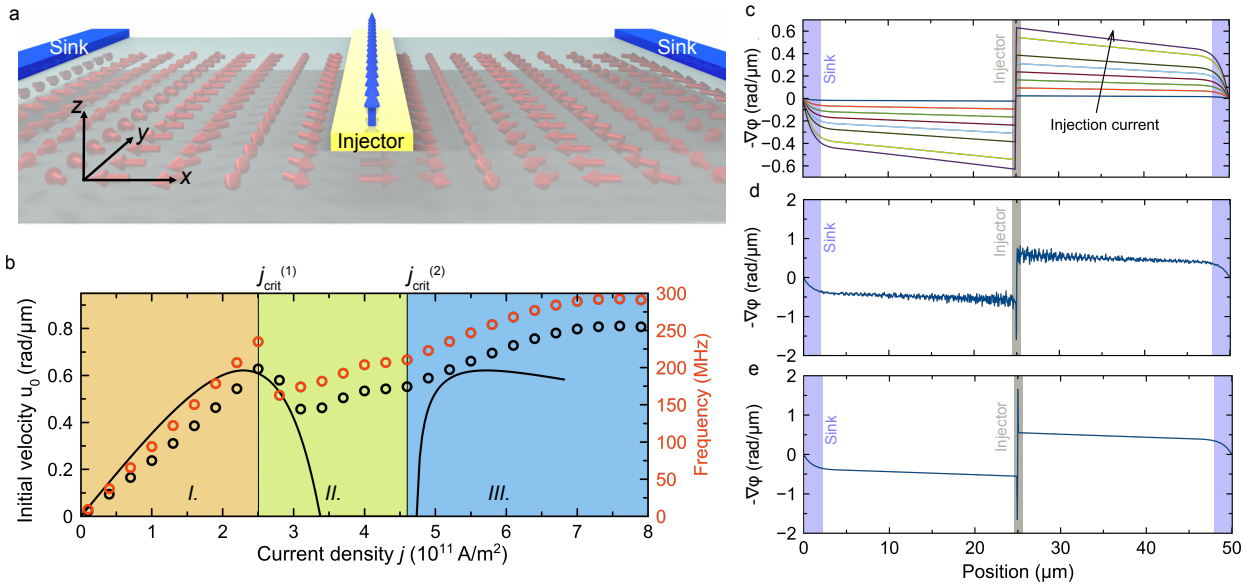

Figure 3.1: Spin superfluid in the absence of dipolar interaction. (a) Schematic view of the thin film. The spin injector provides spin current with out-of-plane polarization (blue arrows). The spin sinks are shown. The red arrows represent a magnetization snapshot. (b) Initial superfluid velocity as a function of the current density (black circles) and base frequency (red circles). Three regimes of the spin superfluid are marked. Black line shows transmitted spin current τ (in the same units as superfluid velocity) calculated based on the analytical model. (c) Spatial dependence of the superfluid velocity in regime I, (d) in regime II at $j = 3.1 \cdot 10^{11}\,\mathrm{A\,m^{-2}}$, (e) in regime III at $j = 4.6 \cdot 10^{11}\,\mathrm{A\,m^{-2}}$.

Here we present a micromagnetic study of superfluid spin transport in extended ferromagnetic thin films and investigate the role of dipolar interaction. We find that stable spin superfluid state can in fact be achieved. Most surprisingly, we observe that the spin superfluid is stable beyond the anticipated Landau instability, allowing for long-range spin transport in a wide range of spin biases.

The Landau superfluid breakdown describes a superflow-carrying state becoming energetically unstable at the critical injection bias. In ferromagnetic films, this corresponds to alignment of magnetic order parameter out-of-plane, which disrupts the superfluid spin transport [60]. Unlike the conventional breakdown of the superfluidity or superconductivity, however, the superflow in our system is recovered. We find that the spin bias applied to the injector does not determine the spin current flowing through the magnet. The latter is rather determined self-consistently, taking into account the feedback of the magnetic dynamics near the injector. We find that this feedback regulates the spin injection through spin wave emission and coherent soliton formation. The superflow thus stays effectively below the Landau instability threshold even at large spin biases.

3.2 Results

We simulate extended ferromagnetic films in the thickness range of $t = 2$—$30\,\mathrm{nm}$ by applying periodic boundary conditions in the film plane to a $50\,\mu\mathrm{m} \times 5\,\mu\mathrm{m}$ patch. Magnetic parameters of the film are chosen (Methods) to mimic $Y_3Fe_5O_{12}$ (YIG) – a magnetic insulator with low damping that may be considered as a candidate for experimental realization of spin superfluidity. Magnetization dynamics is excited by locally injecting a continuous pure spin current with out-of-plane spin polarization. It is simulated through spin-transfer toque in the middle of the film underneath a narrow spin injector. The spin injector carries electric current that translates into spin current with conversion efficiency of $\theta_\mathrm{s} = 0.07$ (see Methods). At the short edges of the film patch, spin sinks are simulated by local increase of the Gilbert damping as explained in Methods. The spin sinks are representative of a spintronics

devices that shall be fed and operated with spin current supplied through the superfluid. All calculations in this study are carried out at 0 K, i.e. without thermal excitations. Figure 3.1a shows sample geometry, spin injector, and spin sinks.

3.2.1 Behavior without dipolar interaction

At first, we investigate the case of omitted dipolar interaction by enforcing zero dipole fields in our simulations and introducing an artificial easy-plane anisotropy $K_{\mathrm{u}} = -10\,\mathrm{kJ\,m^{-3}}$ approximating the shape anisotropy of a thin film [15, 76]. For each current value, the simulations are carried out until steady state or dynamic equilibrium is reached. In Fig. 3.1a, a snapshot of magnetization is shown for the steady state at a current density $j = 10^{11}\,\mathrm{A\,m^{-2}}$ in the spin injector. The magnetization presents continuous 2π-rotations in the film plane, characteristic of the spin superfluid state [60]. The superfluid velocity is defined as $u(x) = -\nabla\phi(x)$, where ϕ is the azimuthal angle of magnetization [15, 60] and the order parameter. Figure 3.1b shows the initial velocities u_0 (calculated in the vicinity of the injector region) as a function of the current density. Three distinct regimes can be identified as indicated in the figure:

Regime I. At low current densities, the superfluid velocity linearly increases with increasing current density, in good agreement with analytical predictions of Ref. [77]. The superfluid velocity decreases smoothly and slowly with increasing distance from the spin injector (Fig. 3.1c). At the spin sink, it decreases more rapidly and reaches zero value. The longitudinal spin density $n = m_z$ (equal to the polar component of the normalized magnetization) [69] is well below 0.5 (Supplementary Figure 1).

Regime II. At the first critical current density $j_{\mathrm{crit}}^{(1)}$, the superfluid starts to exhibit oscillations in real space, as shown in Fig. 3.1d. The initial superfluid velocity is calculated by averaging out these oscillations. It shows a notable drop at the first critical current (Fig. 1b). Underneath the injector, the magnetization is partially tilted out of the film plane by the

spin current. Outside of the injector region, the longitudinal spin density remains $n < 0.5$.

Analysis of the temporal evolution of magnetization reveals large oscillations in the injector region. It emits incoherent spin waves into the rest of the film which superimpose with the superfluid state (Fig. 1d). We observe spin wave emission and the drop of the superfluid velocity for various injection widths $w = 30$—$300\,\mathrm{nm}$. The injector width does not affect the critical current, but modifies [70] the critical current density through geometrical renormalization $j^{(1)}_{\mathrm{crit}} \propto I_{\mathrm{crit}}/w$ (Supplementary Figure 2).

The temporal base frequency Ω of the superfluid spiral is extracted for each current density by calculating the fast-Fourier transformation of the time evolution of the magnetization dynamics. As shown in Fig. 3.1b, both u_0 and Ω exhibit the distinct breakdown in the regime II.

Regime III. Above the second critical current density $j^{(2)}_{\mathrm{crit}}$, the superfluid velocity is again a smooth function of distance (Fig. 1e). No spin waves are observed. The magnetization underneath the injector is almost fully aligned out-of-plane and does not vary with time. Both initial velocity and base frequency show a reduced growth rate with increasing spin current and saturate around $j = 8 \cdot 10^{11}\,\mathrm{A\,m^{-2}}$ (Fig. 1b).

3.2.2 Analytical model

We strive to develop a minimal analytical model to explain the observed phase diagram; we thus neglect dipolar interaction and magnetic damping. With exchange constant A_{ex}, we employ the free energy:

$$F = \int \mathrm{d}x^3 \left[A_{\mathrm{ex}} \left(\nabla \boldsymbol{m}\right)^2 - K_{\mathrm{u}} m_z^2 \right]. \tag{3.2.1}$$

Taking into account that magnetization $\boldsymbol{m}$ does not vary along the y and z directions, Landau-Lifshitz equation assumes the form

$$\frac{\mathrm{d}\boldsymbol{m}}{\mathrm{d}t} = -\boldsymbol{m} \times \left(\frac{\partial^2 \boldsymbol{m}}{\partial x^2} - m_z \hat{\boldsymbol{z}} \right), \tag{3.2.2}$$

where x and t are re-scaled in units of $\sqrt{A_{\mathrm{ex}}/K_{\mathrm{u}}}$ and $\mu_0 M_{\mathrm{s}}/2\gamma K_{\mathrm{u}}$, respectively (with the permeability of free space μ_0 and gyromagnetic ratio γ). By parameterizing the magnetization with spherical coordinates, $\boldsymbol{m} = (\sin\theta\cos\phi, \sin\theta\sin\phi, \cos\theta)$, equation (3.2.2) becomes

$$\dot{\theta}\sin\theta = -\partial_x(\sin^2\theta\,\partial_x\phi), \tag{3.2.3}$$

$$\dot{\phi}\sin\theta = \partial_x^2\theta + \frac{1-(\partial_x\phi)^2}{2}\sin 2\theta. \tag{3.2.4}$$

Equation (3) corresponds to a continuity equation for the longitudinal spin density. We are interested in solutions which satisfy boundary conditions of the form

$$-\partial_x\phi(0) = \tau_i - \gamma\partial_t\phi(0), \quad -\partial_x\phi(L) = \gamma\partial_t\phi(L) \tag{3.2.5}$$

where τ_i is the spin torque from the injection site and γ parameterizes the edge damping effects of spin pumping [72, 78]. General soliton solutions of equation (3.2.2) were studied in Ref. [21]. Here we develop soliton solutions with boundary conditions (3.2.5). Assuming soliton solutions have the form $\theta = \theta(x - ct)$ results (Methods) in

$$\phi - \phi_0 = \omega t - \int_0^x \mathrm{d}x' \frac{c\cos\theta + a_1}{\sin^2\theta}, \tag{3.2.6}$$

$$x - ct = x_0 \pm \frac{1}{\sqrt{2}} \int_{\theta_1}^{\theta(x,t)} \frac{\mathrm{d}\theta'}{\sqrt{f(\theta')}}, \tag{3.2.7}$$

where $f(\theta) = a_2 - \omega\cos\theta - \frac{1}{2}\sin^2\theta - \frac{1}{2}(c^2 - a_1^2)\csc^2(\theta) - ca_1\cot(\theta)\csc(\theta)$. Here ω, c, ϕ_0, a_1, and a_2 are integration constants. We consider the case in which $f(\theta) > 0$ for some open

interval $(\theta_1, \theta_2) \subset (0, \pi/2)$, where θ_1 and θ_2 are zeros of $f(\theta)$. The resulting soliton solution, $\theta(x-ct)$, is symmetric about its minimum θ_1 (corresponding to a spike in m_z) centered at x_0 at $t = 0$. Because the soliton expression (7) only describes θ over a finite interval of $x - ct$, to describe a full solution, the soliton and its first derivatives must be patched to suitable surrounding solutions, such as another soliton or a superfluid, or to the boundary conditions. This patching process fixes the integration constants. One such solution is an isolated soliton traveling at speed c through a surrounding spin superfluid which has constant polar angle θ_2. The length of the soliton is determined by the characteristic length scale $\sqrt{A_{\mathrm{ex}}/K_{\mathrm{u}}}$.

We find the relevant solutions by fixing the boundary conditions with a spin injection site and spin sink on either side. The analytically calculated transmitted spin current per spin density ($\tau = -\nabla\phi \sin^2\theta$) is shown in Fig. 1b as the black solid line. The analytical spin current plot shows three distinct phases, similar to the three phases identified in micromagnetic simulations. The low-current regime (I) corresponds to the conventional spin superfluidity, i.e. a coherently precessing constant-θ superflow as derived in Ref. [71].

In a previous analytical study [71], the drop of the transmitted spin current to zero at intermediate bias has been associated with spin superfluid becoming fully polarized out of plane ($\theta = 0$). However, such state is in fact unstable, even in the undamped model. It has a mode of instability which forms near the boundaries and propagates into the rest of the film. This mode of instability has superfluid-like precession and grows exponentially with time. There are no stable time-independent θ solutions in the intermediate (II) regime between the two analytical solutions (I) and (III) plotted in Fig. 1b. The solution in the intermediate (II) regime must thus be a non-trivial dynamic state. The first critical current observed in micromagnetic simulations may, in fact, be different from the critical current derived in Ref. [71]. The damped model micromagnetic simulations indicate that the dynamic instability sets in before the precipitous drop in the calculated transmitted spin current (and below the Landau criterion). The mechanisms and system parameters [69], that may shift the first critical current and determine the current range of the intermediate regime, are yet

to be fully understood.

Above the second critical current, we find a stationary soliton solution $c = 0$ of particular interest. The soliton is placed with the peak at the injection region boundary. In regime III, the injector region is nearly fully polarized out-of-plane, and the local time-dependent oscillations in θ cease. As micromagnetic simulations show, this configuration lacks the spin wave noise present in regime II. The spin current is reduced by the injector edge soliton due to the $(1 - m_z^2)$ factor in the spin current. For high out-of-plane polarizations, it diminishes the transmitted spin current at the same superfluid velocity u. The polarization in the injector region partially blocks the spin injection, and the transmitted spin current asymptotically behaves as $\propto 1/j$ for $j \to \infty$. By virtue of this self-regulation in the injector region, the superfluid persists above biases expected for the Landau instability. We therefore suggest to name this regime *screened spin superfluid*.

The exact mechanism of the superfluid stabilization in regime II remains elusive, however, the data allows us to propose two hypotheses. (i) The superfluid solution may be a hybrid periodically transitioning between the conventional superfluid and screened superfluid. The steady-state solution that matches the boundary conditions ($\theta = 0$) is unstable to variations in θ, resulting in the spin texture dropping down to a θ-superfluid which is unable to accommodate the large spin current at the boundaries. Therefore, the stationary soliton of a screened superfluid begins to form as spin accumulates near the edge of the injector region. However, the spin current is not strong enough to maintain a stable soliton, and the soliton decays into spin waves before reaching steady-state screening. The soliton formation and decay processes are then repeated, resulting in injector region oscillations and spin waves propagating into the film. (ii) The solution may be a large amplitude spin wave over the superfluid which would be composed of the above derived propagating solitons, fitted back to back and satisfying the boundary conditions on average. These large amplitude spin waves would have to quickly decay, possibly due to Suhl scattering [79], resulting in the observed noise of incoherent spin waves. The reduction of superfluid velocity observed in the micro-

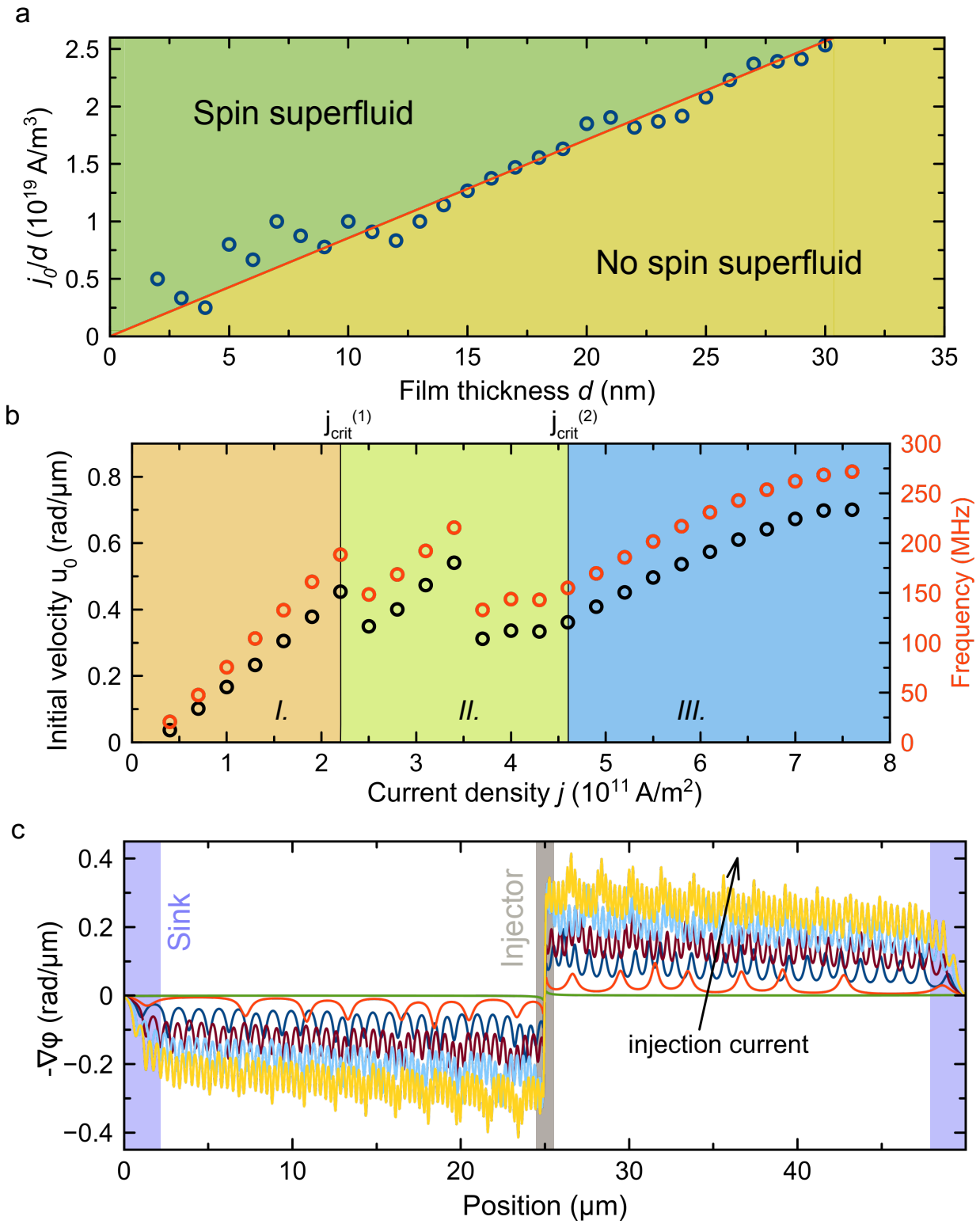

Figure 3.2: Spin superfluid in the presence of dipolar interaction. (a) Threshold current as a function of film thickness. (b) Initial superfluid velocity as a function of the current density for 5 nm thick film (sub-threshold regime omitted for clarity). (c) Spatial dependence of the superfluid velocity.

magnetic simulations could be explained by the emergence of such dissipation channel for the injected spin current.

3.2.3 Impact of dipolar interaction

A previous study [75] on micron-sized ferromagnetic thin films has pointed out a detrimental effect of the dipolar interaction on the spin superfluidity, leading to a collapse of the operable bias range. Here, we investigate extended systems by employing periodic boundary conditions. In the following micromagnetic simulations, the dipolar interaction is enabled and the previously used uniaxial anisotropy K_u is set to zero.

First, we find that the presence of the dipolar interaction suppresses spin superfluidity at low currents and imposes a threshold j_0 for its formation [75]. The dipolar interaction acts as an effective magnetic anisotropy [60, 69, 70] that must be overcome. The effective dipole energy increases with the thickness of the film d which is varied in the range of 2—30 nm in our simulations. For comparison across different film thicknesses, the current needs to be scaled by d. Indeed, Fig. 2a shows that such normalized threshold current j_0/d increases nearly linearly with increasing film thickness.

Upon the formation of spin superfluid, its initial velocity u_0 presents non-monotonous dependence on the current density. Figure 2b shows a qualitatively very similar behavior as in the case of omitted dipolar interaction. Employing spatio-temporal analysis of the magnetization dynamics, we find again: (I) the low-current regime free of incoherent spin waves, (II) the intermediate regime with co-existing superfluid and incoherent spin waves, and (III) the high-current regime of screened superfluid, free of incoherent spin waves. An additional notable drop of the initial velocity and base frequency is observed in the middle of the intermediate regime (II). A detailed evaluation of the data reveals that u and Ω show multiple non-monotonicities for both dipole case and dipole-free case. While the currents at which they occur differ, their presence seems to be universal and is likely related to the

non-linear generation of spin waves in the regime II.

We further find differences of the spatial profile of superfluid velocity compared to the dipole-free case. As shown in Fig. 2c, the gradient of the azimuthal angle presents two types of modulations. Due to the continuous 2π-rotations of magnetization, dipolar interaction introduces a perturbation of the energy landscape with uniaxial symmetry – the magnetic charges alternate at every π-rotation. Upon these perturbations, the angle gradient shows a small magnitude modulation with periodicity being a multiple of the periodicity of the π-rotations.

Another modulation with larger amplitude has a smaller periodicity (larger wavelength) that corresponds to the π-rotations of magnetization. The in-plane components of magnetization present a distorted sinusoidal profile as a function of distance (Supplementary Figure 3). The out-of-plane component of magnetization reveals spikes at the locations of magnetic charges (at extrema of m_x), which reduces the exchange energy. This modulation can be considered a soliton lattice, resulting in a superfluid state with a broken symmetry. The symmetry is broken by the shape of the spin injector and is mediated to the spin superfluid by virtue of the dipolar interaction. The size of the soliton scales as $1/\langle\partial_x\phi\rangle_{\text{ave}}$ – the current-dependent averaged winding length of the spin superfluid.

3.3 Discussion

In this study, spin superfluidity is found to persist over a large range of bias currents. The magnetization pinning by dipole fields [75] does not fully suppress the superfluidity at high biases for the case of extended films [69]. The threshold suppression of spin superfluidity at low biases has been previously discussed [60,80] for symmetry-breaking magnetic anisotropy. In contrast to the effect of such local anisotropy, the symmetry breaking, investigated in this study, is mediated by the non-local dipolar interaction [70]. We find the threshold current to increase linearly with increasing dipole energy.

A coupling between the superfluid order parameter (azimuthal angle ϕ) and the longitu-

dinal spin density n is observed. The longitudinal spin density shows oscillations at twice the base frequency [70], in agreement with the symmetry order of the effective (uniaxial) magnetic anisotropy due to dipole fields. The oscillations correspond to excitations of the soliton lattice. No such behavior is observed in the absence of the dipolar interaction.

We identify three regimes of spin superfluidity, universally present with and without dipolar interaction. In the low-current regime, conventional spin superfluidity is found. Above the first critical current, the superfluid co-exists with incoherent non-thermally populated magnons. Above the second critical current, the incoherent magnons are suppressed and a soliton screened spin superfluid is found.

We discover the ability of the spin superfluid to self-stabilize beyond the anticipated critical injection bias. The spin superflow is not determined by the injection current alone but self-consistently, taking into account the spin reconstruction in the injector region. At very high biases the superfluid is partially screened from injected spin current by soliton formation. For the intermediate-current regime, we identify non-linear magnon scattering to play a role in superfluid self-stabilization.

Recently, spin injection with perpendicular polarization due to spin-orbit effect with spin rotational-symmetry [81] and due to planar Hall effect [82] has been experimentally realized using metallic ferromagnets. Moreover, efficient thermal spin injection [83] with polarization not bound to injector geometry has been achieved [84]. These developments may benefit designing novel ferromagnetic spin injectors and instigate research on thin film-based spin superfluids. In such studies, questions on spin texture formation in the injector region due to interaction with the injector, thermal stability of the superflow, and accessible spin bias range are likely to arise. Our work points out the impact of injector spin texture formation and incoherent spin waves on stabilization of spin superfluidity and extending the range of achievable spin biases.

3.4 Methods

3.4.1 Micromagnetic simulations.

The dipolar interaction was implemented using MuMax code [85] and the magnetostatic field was calculated by the approach presented in Ref. [86]. The material parameters were chosen to simulate YIG films [87–89]: the saturation magnetization $M_\mathrm{s} = 130\,\mathrm{kA\,m^{-1}}$ and the exchange constant $A_\mathrm{ex} = 3.5\,\mathrm{pJ\,m^{-1}}$. The magnetocrystalline anisotropy was omitted. The spin sinks were intended to emulate a spintronic devices to be operated by the spin current transmitted through the superfluid. They were modeled by non-uniform increase of the Gilbert damping over the width ($4\,\mu$m) of the spin sink regions. From the sink edge closer to the injector to the edge at the end of the film patch, the damping constant α was increased exponentially from 0.002 to 0.11. Such modification of damping emulate extraction of angular momentum from the superflow and prevents potential reflections of spin excitations at the edges of the patch, which is necessary to simulate an extended spin system. To ensure that the system reached a dynamic steady-state, a simulation time of 500 ns was chosen. The electric current density given throughout the manuscript corresponds to the spin current via $j_\mathrm{s} = \theta_\mathrm{s}\frac{\hbar}{e}j$ with the spin conversion efficiency θ_s, the Planck constant $\hbar$ and the elementary charge e. All micromagnetic simulations were carried out at zero temperature. The cell size is $24.41\,\mathrm{nm}\times 19.53\,\mathrm{nm}\times d$; the results were validated by carrying out selected simulations with a reduced cell size.

3.4.2 Analytical model

Numerical calculations of the analytical model resort to the same material parameters as micromagnetic simulations, but do not include magnetic damping. Here we derive equations (5) and (6). The assumption $\theta = \theta(x - ct)$ implies that the left-hand-side of Equation (3) can be written as a derivative in x, thus allowing Equation (3) to be integrated. The result can

be solved for $\partial_x \phi$ and integrated again to express ϕ in terms of θ. In general, the constants of integration can depend on t, i.e.

$$\phi = C_2(t) - \int^x dx' \frac{c\cos\theta + C_1(t)}{\sin^2\theta}. \tag{3.4.1}$$

However, the time dependence is restricted by substituting the expression for ϕ in terms of θ into Equation (4). Once θ has been isolated, the resulting equation should not have explicit t dependence because, by assumption, θ only depends on $x - ct$. This implies that C_1 is independent of time and restricts C_2 to at most linear dependence on t, thus resulting in equation (6). Once ϕ dependence has been eliminated in Eq. (4), equation (7) follows by direct integration with the integrating factor $\partial_x \theta$.

Investigation of dipolar effects was supported as part of the "Spins and Heat in Nanoscale Electronic Systems" (SHINES), an Energy Frontier Research Center funded by the U.S. Department of Energy, Office of Science, Basic Energy Sciences (BES) under Award # SC0012670. Investigation of the superfluid phase transitions was supported by the National Science Foundation under Grant No. ECCS-1810541. The analytical modeling by D.H. and Y.T. was supported by the US Department of Energy, Office of Basic Energy Sciences, under Award No. DE-SC0012190. We thank NVIDIA Corporation for the donation of Titan Xp GPU used for some of the calculations. We thank Jürgen König, Se Kwon Kim, and Hector Ochoa for helpful discussions.

T. S. and A. K. carried out numerical simulations. D. H. and Y. T. developed the analytical model. I. B. carried out numerical simulations and supervised the project. All authors contributed to writing the manuscript.

The authors declare no competing financial interests.

Chapter 4

Spin analogs of superconductivity and integer quantum Hall effect in an array of spin chains

Motivated by the successful idea of using weakly coupled quantum electronic wires to realize the quantum Hall effects and the quantum spin Hall effects, we theoretically study two systems composed of weakly coupled quantum spin chains within the mean-field approximations, which can exhibit spin analogs of superconductivity and the integer quantum Hall effect. First, a certain bilayer of two arrays of interacting spin chains is mapped, via the Jordan-Wigner transformation, to an attractive Hubbard model that exhibits fermionic superconductivity, which corresponds to spin superconductivity in the original spin Hamiltonian. Secondly, an array of spin-orbit-coupled spin chains in the presence of a suitable external magnetic field is transformed to an array of quantum wires that exhibits the integer quantum Hall effect, which translates into its spin analog in the spin Hamiltonian. The resultant spin superconductivity and spin integer quantum Hall effect can be characterized by their ability to transport spin without any resistance.

4.1 Introduction

In a metal under normal conditions, an electric current flows in the presence of a finite resistance engendered by, e.g., scattering with impurities. The lost electrical energy due to the resistance is dissipated into heat, which is referred to as Joule heating that opposes the efficient use of the energy. There are, however, two physical phenomena under special conditions that allow an electric current to flow without any resistance. The one is superconductivity occurring at low temperatures [90]. Its first microscopic theory was given in 1957 by Bardeen, Cooper, and Schrieffer [91], who showed that superconductivity can be understood as a property of macroscopic quantum wavefunction of condensed pairs of electrons subsequently termed Cooper pairs. The other is the set of quantum Hall effects exhibited in two-dimensional systems at low temperatures and strong magnetic fields [92]. The integer quantum Hall effect is the first of such that was discovered in 1980 by ref. [93]. It occurs when the number of electrons per unit magnetic flux takes an integer value ν, leading to the situation in which the bulk is gapped, but the edge supports ν gapless modes with no resistance.

Spintronics aims at harnessing the spin degrees of freedom to advance from conventional charge-based electronics [94, 95]. In particular, magnetic insulators that are free from Joule heating have been gaining attention in the field owing to their potential advantage of low-energy consumption. An efficient spin transport in such magnetic insulators is one of the important topics in spintronics, and researchers have been investigating possible ways to achieve it by borrowing some ideas from the aforementioned phenomena of dissipationless charge transport. For example, a spin-analogue of an electric supercurrent supported in easy-plane magnets has been theoretically investigated [15, 24, 44, 59, 60, 96–98], which is shown to decay algebraically as a function of the distance from the spin-injection point contrary to an exponential decay of a diffusive spin current. Spin analogues of the integer and fractional quantum Hall phases have also been put forward in the studies of spin liquids [99–103] and

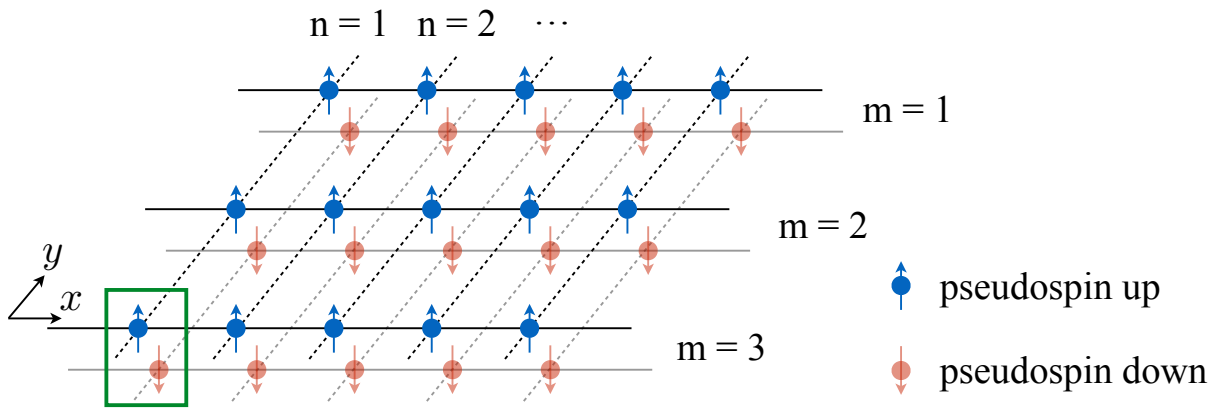

Figure 4.1: Schematic of a bilayer of two arrays of weakly-coupled spin chains (shown as the solid lines indexed by m), each of which can be represented by a one-dimensional system of (spinless) Jordan-Wigner fermions. The top and bottom layer indices serve as the pseudospin up and down for the fermions, respectively. The green box represents a pseudospin-singlet Cooper pair of two fermions established by an Ising interlayer interaction.

topological magnon insulators [104–110].

In this Letter, we theoretically construct two spin systems, which can exhibit spin analogues of superconductivity and the integer quantum Hall effect, by using weakly-coupled quantum spin chains. Our work is motivated by the successful theoretical realizations of the quantum Hall phases and the quantum spin Hall phases in an array of quantum electronic wires [111–114]. Specifically, first, we show that an Ising-coupled bilayer of two arrays of weakly-coupled quantum XX spin chains can be mapped to a negative-U Hubbard model for electrons by the Jordan-Wigner (JW) transformation [115, 116] within a mean-field treatment of the interchain coupling. The established charge superconductivity of the negative-U Hubbard model [117] then naturally translates into spin superconductivity of our original spin system. See Fig. 4.1 for an illustration of the system. Secondly, we show that an array of weakly-coupled quantum XX spin chains with Dzyaloshinskii-Moriya (DM) intrachain interaction can be transformed to an array of quantum electronic wires subjected to an external magnetic field by the same approach taken for spin superconductivity. The integer quantum Hall effect of the latter electronic system [113] then translates into its spin analogue of the former spin system. See Fig. 4.2(a) for an illustration of the system.

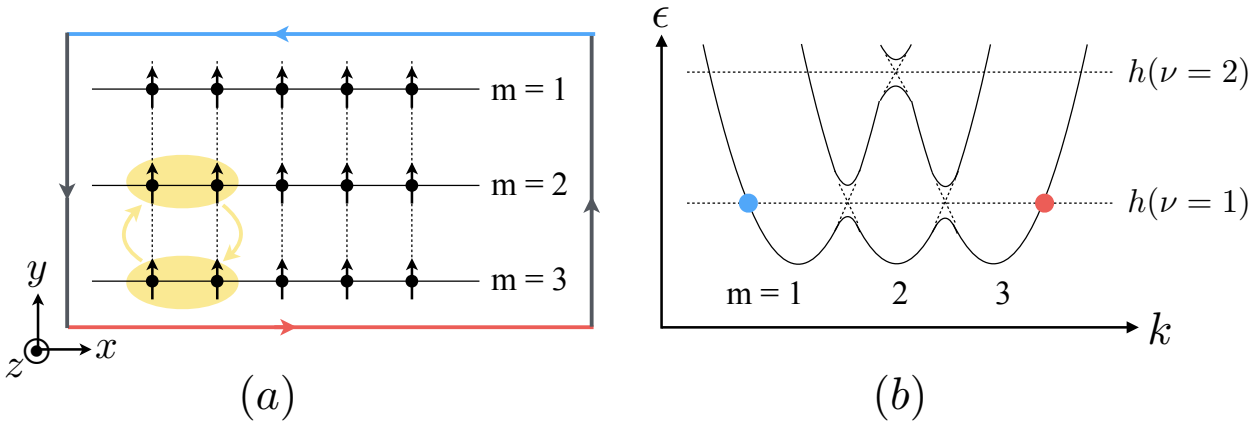

Figure 4.2: (a) Schematic of an array of spin-orbit-coupled spin-1/2 spin chains, which can support chiral edge modes of the Jordan-Wigner fermions. The coupling of four spins (colored by yellow) illustrates the interchain interaction $\mathcal{O}$ [Eq. (4.2.2)]. (b) A schematic plot showing how the interchain interaction gives rise to chiral edge modes with the gapped bulk. At the external magnetic field h corresponding to the filling factor $\nu = 1$, the JW fermion can flow in the left direction on the top chain (colored by blue) and in the right direction on the bottom chain (colored by red) in (a), which are represented by the left blue and right red dots in (b), respectively. The particle current in the JW representation corresponds to the spin current polarized along the z axis.

4.2 Main results

Our main results can be summarized as follows. First, for spin superconductivity, we consider the following spin Hamiltonian for two layers of weakly-coupled M spin-1/2 chains of length N:

$$\begin{aligned} H_{\rm sc} =& J \sum_{n,m,\alpha} \boldsymbol{\sigma}^{\parallel}_{n,m,\alpha} \cdot \boldsymbol{\sigma}^{\parallel}_{n+1,m,\alpha} \\ & - H \sum_{n,m,\alpha} \sigma^z_{n,m,\alpha} - U \sum_{n,m} \sigma^z_{n,m,\uparrow} \sigma^z_{n,m,\downarrow} \\ & - K \sum_{n,m,\alpha} \left[\mathcal{O}_{n,m,\alpha} + \text{H.c.} \right] , \end{aligned} \tag{4.2.1}$$

with

$$\mathcal{O}_{n,m,\alpha} = \sigma^+_{n,m,\alpha} \sigma^+_{n+1,m,\alpha} \sigma^-_{n,m+1,\alpha} \sigma^-_{n+1,m+1,\alpha} , \tag{4.2.2}$$

where the integers m and n are the indices for a spin chain within a layer and a spin within a chain, respectively, and $\alpha = \uparrow, \downarrow$ indexes the layer which will serve as the pseudospin of the JW fermions. A spin is represented by the three-dimensional Pauli matrices $\boldsymbol{\sigma}$; the symbol $\parallel$ denotes the projection of the vector onto the xy plane; $\sigma^{\pm} \equiv (\sigma^x \pm i\sigma^y)/2$. Here, the first term describes the quantum antiferromagnetic XX spin-1/2 chains with $J > 0$ [1]; the second term is the Zeeman energy; the third term is the ferromagnetic Ising interaction between the two layers; the last term represents a weak four-spin interaction with $0 < K \ll J$, which, in the JW representation, can engender the interchain tunneling and thereby make each layer an effective two-dimensional fermionic gas. Interchain interactions involving only two spins such as the Heisenberg XX exchange $\propto \boldsymbol{\sigma}^{\parallel}_{n,m} \cdot \boldsymbol{\sigma}^{\parallel}_{n,m+1}$ would also appear as tunneling between two chains. They, however, introduce nonlocal terms after the JW transformation, making it difficult to treat the interchain interaction [2]. Our goal, instead, is to construct simple spin systems that can be viewed as weakly-interacting simple fermionic wires. Therefore, by coupling neighboring spin chains by the four-spin interaction, we retain its locality after the JW transformation.

The spin Hamiltonian $H_{\rm sc}$ can be transformed into the Hamiltonian for the spinless fermions by the multi-dimensional JW transformation [116]:

$$f_{n,m,\alpha} = \sigma^{-}_{n,m,\alpha} \left(\prod_{l<n} \sigma^{z}_{l,m,\alpha} \right) \left(\prod_{(k,\beta)<(m,\alpha)} \tau^{y}_{k,\beta} \right) \tau^{x}_{m,\alpha} \,, \tag{4.2.3}$$

and the analogous expression for $f^{\dagger}_{n,m,\alpha}$ with σ^{-} substituted by σ^{+}, where the auxiliary Pauli-matrix vector, $\boldsymbol{\tau}_{m,\alpha}$, is introduced for each spin chain to make the fermion operators on different chains anticommute [3] The interchain interaction yields a quartic term in the

[1] We do not lose any generality by choosing the sign of the exchange interaction, $J > 0$ here, for the sign can be flipped by rotating every other spin by π around the z axis.

[2] The long-range interchain interactions may be treated within the framework of the coupled Luttinger liquids [118], but it is beyond the scope of our work.

[3] The comparison of two tuples, (k, β) and (m, α), representing two spin chains is determined by their orders in a serialization of spin chains, which can be arbitrarily chosen for our models. An alternative JW transformation would have $\beta = \alpha$ in the product and an additional Pauli matrix factor for maintaining anticommutation between the two layers for the RHS.

fermion operators, and thus we take the mean-field approach to study its effect. We will show that the resultant mean-field Hamiltonian is given by the attractive Hubbard model [117]:

$$\begin{aligned}\bar{H}_{\rm sc} =& - t_x \sum_{n,m,\alpha} \left[f^\dagger_{n,m,\alpha} f_{n+1,m,\alpha} + \text{H.c.} \right] \\ & - t_y \sum_{n,m,\alpha} \left[f^\dagger_{n,m,\alpha} f_{n,m+1,\alpha} + \text{H.c.} \right] \\ & - \mu \sum_{n,m,\alpha} n_{n,m,\alpha} - u \sum_{n,m} n_{n,m,\uparrow} n_{n,m,\downarrow} \,,\end{aligned} \tag{4.2.4}$$

where $n_{n,m,\alpha} = f^\dagger_{n,m,\alpha} f_{n,m,\alpha}$ is the fermion-number operator, $t_x = 2J, t_y = 2K\chi, \mu = 2H - 2U$, and $u = 4U$. Here, $\chi \equiv \langle \sum_{n,m,\alpha} f^\dagger_{n,m,\alpha} f_{n,m+1,\alpha} \rangle / 2NM$ is the mean field for the interchain tunneling [4]. By $\bar{H}$, we will denote the Hamiltonians in the JW representation throughout. When the Fermi energy lies close to the bottom of the band for a single chain, $\mu = -2t_x + \delta\mu$ with $|\delta\mu| \ll K$, the interchain tunneling amplitude is given by $\chi \approx K/25t_x$. From the results known for the attractive Hubbard model [117], we can conclude that the ground state of the Hamiltonian $\bar{H}_{\rm sc}$ away from the half-filling is in the superconducting phase composed of pseudospin-singlet Cooper pairs of the JW fermions, which should exhibit a spin-analogue of charge superconductivity [5].

Second, for a spin analogue of the integer quantum Hall effect, we take the following spin Hamiltonian:

$$\begin{aligned}H_{\rm qh} =& J \sum_{n,m} \cos(m\phi)\, \boldsymbol{\sigma}^{\parallel}_{n,m} \cdot \boldsymbol{\sigma}^{\parallel}_{n+1,m} \\ & + J \sum_{n,m} \sin(m\phi)\, \hat{\mathbf{z}} \cdot \boldsymbol{\sigma}_{n,m} \times \boldsymbol{\sigma}_{n+1,m} \\ & - H \sum_{n,m} \sigma^z_{n,m} - K \sum_{n,m} \left[\mathcal{O}_{n,m} + \text{H.c.} \right] \,,\end{aligned} \tag{4.2.5}$$

[4] The Hartree-Fock decoupling is taken only for the interchain interaction, not for the Ising interlayer interaction.

[5] In the weak-attraction limit, $u \ll t_x\,, t_y$, the superconducting gap is given by $\Delta \sim t\sqrt{\rho(2-\rho)}/\sinh(t/u)$, where $t \equiv t_x + t_y$ is the bandwidth and ρ is the number of electrons per site [117].

where the four-spin interaction $\mathcal{O}_{n,m}$ is given by Eq. (4.2.2) with α removed. Here, the first two terms describe the antiferromagnetic Heisenberg XY spin chains with the DM interaction; the third term is the Zeeman coupling; the last term is the weak interchain interaction, $0 < K \ll J$. See Fig. 4.2(a) for an illustration of the system. The DM interaction can exist if the reflection symmetry with respect to the xz plane is broken; the Hamiltonian respects the reflection symmetries through the xy and yz planes. The chain-dependent exchange coefficients can be realized by controlling the extent of the reflection-symmetry breaking associated with the DM interaction. We focus on the weak DM interactions, $0 < \phi J \ll K$, comparing to the interchain coupling [6].

By employing the JW transformation [116] and taking the mean-field approach for the interchain interaction, as shown below, we obtain the following tight-binding Hamiltonian:

$$\begin{aligned} \bar{H}_{\rm qh} = & - t_x \sum_{n,m} \left[e^{im\phi} f^\dagger_{n,m} f_{n+1,m} + \text{H.c.} \right] \\ & - t_y \sum_{n,m} \left[f^\dagger_{n,m} f_{n,m+1} + \text{H.c.} \right] \\ & - \mu \sum_{n,m} n_{n,m} \,, \end{aligned} \tag{4.2.6}$$

which describes an array of quantum electronic wires in the presence of an external magnetic field $\propto \phi$. The parameters are given by $t_x = 2J, t_y = 2K\chi$, and $\mu = 2H$ with the mean-field interchain tunneling χ. The integer quantum Hall effect at the filling factor $\nu = 1$ arises when the Fermi energy is close to the crossing point of the two bands of adjacent chains, $\mu = -t_x(2+\phi^2)+\delta\mu$ with $|\delta\mu| \ll t_x$. The self-consistent solution is then given by $\chi \simeq K/25t_x$. The integer quantum Hall effects at higher filling factors ν can be analogously obtained in the νth order of the perturbative treatment of the interchain interaction [113, 114].

The Hamiltonian $\bar{H}_{\rm qh}$ has been shown to exhibit the integer quantum Hall effect [111,113]. Let us briefly explain how the integer quantum Hall effects arise in the model for an example

[6] For the strong DM interactions comparing to the interchain coupling, $0 < K \ll \phi J$, the mean field for the interchain tunneling is exponentially small, $\chi \sim \exp(-4\pi\phi J/K)$.

of filling factor $\nu = 1$. See Fig. 4.2(b) for the JW fermion bands of spin chains and the gap openings by the interchain tunneling. When the Fermi energy μ lies in the bulk gap, there are one gapless mode in the top chain ($m = 1$ in the figure) and the other in the bottom chain ($m = 3$ in the figure). The two modes propagate in the opposite directions, and thus engender one chiral edge mode together. The integer quantum Hall effect at higher filling factors ν supports ν chiral edge modes by an analogous mechanism [113, 114]. The state we obtained is different from the conventional quantum Hall phase in that the transported quantity is spin, not charge; it is also distinct from the traditional quantum spin Hall phase [119] in that the resultant spin transport does not accompany any charge transport.

Although, to the best of our knowledge, there is no physical system that can realize our proposal, let us make some comments about experimental realizations. First, spin-1/2 chain systems Cs_2CoCl_4 [120] and $PrCl_3$ [121] are known to be well described by the isotropic Heisenberg XX model. Secondly, the DM interaction in a single chain can be induced by breaking the reflection symmetry through the xz plane, which can be, in principle, realized by attaching a one-dimensional nonmagnetic material next to the spin chain. The gradient in the DM interaction can be engendered by modulating the distance between the nonmagnetic material and the spin chain. Lastly, the four-spin exchange interaction can arise as the fourth-order term in the strong-coupling expansion of the half-filled Hubbard model or due to the spin-lattice coupling, and its magnitude can be comparable to two-spin Heisenberg exchange in certain materials [122–124].

4.3 Spin superconductivity

We explain how we obtained the mean-field values for the interchain tunneling amplitude for the case of spin superconductivity. To analyze the effects of the quartic fermion operator $f^\dagger_{n,m,\alpha} f^\dagger_{n+1,m,\alpha} f_{n,m+1,\alpha} f_{n+1,m+1,\alpha}$ mapped from $\mathcal{O}_{n,m,\alpha}$ [Eq. (4.2.2)], we employ the Hartree-

Fock decoupling [125]. There are two potentially relevant mean-field order parameters [7]. One is an interchain-tunneling amplitude,

$$\chi = \frac{1}{2NM} \sum_{n,m,\alpha} \langle f^{\dagger}_{n,m,\alpha} f_{n,m+1,\alpha} \rangle \,. \tag{4.3.1}$$

The other is an intrachain Cooper-pairing amplitude,

$$\Delta = \frac{1}{2NM} \sum_{n,m,\alpha} \langle f_{n,m,\alpha} f_{n+1,m,\alpha} \rangle \,. \tag{4.3.2}$$

The mean-field Hamiltonian for a single layer is given by

$$\begin{aligned} \bar{H}_{\alpha} = & - t_x \sum_{n,m} \left[f^{\dagger}_{n,m,\alpha} f_{n+1,m,\alpha} + \text{H.c.} \right] \\ & - 2K \sum_{n,m} \left[\chi f^{\dagger}_{n,m,\alpha} f_{n,m+1,\alpha} + \text{H.c.} \right] \\ & - 2K \sum_{n,m} \left[\Delta f^{\dagger}_{n,m,\alpha} f^{\dagger}_{n+1,m,\alpha} + \text{H.c.} \right] \\ & - \mu \sum_{n,m} n_{n,m,\alpha} \,, \end{aligned} \tag{4.3.3}$$

up to an additive constant, in the limit of zero interlayer coupling $U \to 0$. Assuming the periodic boundary conditions, the self-consistency equations for the two mean-field order parameters χ and Δ in the momentum space are given by

$$\Delta = \frac{1}{NM} \sum_{\mathbf{k}} \frac{2K\Delta \sin^2 k_x}{\sqrt{\epsilon(\mathbf{k})^2 + |\Delta(\mathbf{k})|^2}} \,, \tag{4.3.4}$$

$$\chi = \frac{1}{NM} \sum_{\mathbf{k}} \frac{\cos k_y}{2} \left(1 - \frac{\epsilon(\mathbf{k})}{\sqrt{\epsilon(\mathbf{k})^2 + |\Delta(\mathbf{k})|^2}} \right) \,, \tag{4.3.5}$$

where $\epsilon(\mathbf{k}) = -2t_x \cos k_x - 4K\chi \cos k_y - \mu$ and $\Delta(\mathbf{k}) = 4iK\Delta \sin k_x$. Here, the spatial coordinates x and y are the continuum analogues of n and m. Since the coefficient for

[7] There is the third mean field, $\sum_{n,m,\alpha} \langle f^{\dagger}_{n,m,\alpha} f_{n+1,m+1,\alpha} \rangle$, but it is omitted from the analysis because its effects are similar to those of χ and thus do not change the qualitative property of the system.

the interchain interaction is assumed to be positive, $K > 0$, the Cooper-pairing amplitude vanishes, $\Delta = 0$. To compute the self-consistent solution for χ analytically, we assume that the effective chemical potential is closed to the bottom of the band for a single chain, $\mu = -2t_x + \delta\mu$ with $|\delta\mu| \ll K$, and use a parabolic band approximation for the dispersion $\epsilon(\mathbf{k})$ around the origin. We then obtain

$$\chi = \left(\int_0^{\pi/2} dk_y \, \cos^{3/2} k_y \right)^2 \frac{4K}{\pi^4 t_x} + \mathrm{O}\left(\frac{\delta\mu}{K} \right) , \tag{4.3.6}$$

which can be approximated to $\chi \approx K/25t_x$. With the finite $\chi_\alpha = \chi$ and vanishing $\Delta_\alpha = 0$, the mean-field Hamiltonian $\bar{H}_\alpha$ (4.3.3) for a single layer describes a two-dimensional spinless fermion gas.

4.4 Spin integer quantum Hall effect

Next, we explain the derivation of the mean-field results for the case of spin integer quantum Hall effect. Since the gradient of spin-orbit coupling breaks the translational symmetry of the system along the y axis, it is difficult to obtain an analytical mean-field solution χ for arbitrary M. Instead, let us consider a special case of two weakly-coupled spin chains, which is described by H_{qh} [Eq. (4.2.5)] with $m = \pm 1$. Two possible order parameters pertain to the interchain tunneling, $\chi = \sum_n \langle f^\dagger_{n,1} f_{n,-1} \rangle / N$, and the Cooper pairing, $\Delta = \sum_{n,m=\pm1} \langle f_{n,m} f_{n+1,m} \rangle / 2N$. The mean-field Hamiltonian for the JW fermions in the momentum space is given by

$$\begin{aligned} \bar{H} = & \sum_{k,m=\pm1} \left[(-2t_x \cos(k + m\phi) - \mu) f^\dagger_{k,m} f_{k,m} \right] \\ & - 2K \sum_k \left[\chi f^\dagger_{k,1} f_{k,-1} + \mathrm{H.c.} \right] \\ & - 2K \sum_{k,m=\pm1} \left[\Delta e^{ik} f^\dagger_{k,m} f^\dagger_{-k,m} + \mathrm{H.c.} \right] . \end{aligned} \tag{4.4.1}$$

We will assume that two phases with finite χ and Δ are mutually exclusive, and will treat them separately. For $K > 0$, which is assumed throughout the Letter, the self-consistency equation yields a vanishing Cooper-pairing amplitude, $\Delta = 0$, as in the case of spin superconductivity. With $\Delta = 0$, the band structure of the Hamiltonian is $\epsilon_{\pm}(k) = t_x k^2 - \delta\mu \pm 2\sqrt{(t_x\phi k)^2 + (K\chi)^2}$ for $|k|, |\phi| \ll 1$, where $\mu = -t_x(2 + \phi^2) + \delta\mu$. When the effective Fermi energy is at the band-crossing point, $\delta\mu = 0$, the analytical solution to the self-consistency equation for χ is given by $\chi \simeq K/4\pi^2 t_x$, which agrees well with $\chi \approx K/50t_x$ [Eq. (4.3.6)] obtained for the $M \to \infty$ case. The finite interchain tunneling $\chi > 0$ opens up the gap at the crossing point of the two bands of chains. See Fig. 4.2(b) for illustrations of the gap openings.

4.5 Discussion

We have theoretically constructed the two models of an array of weakly-coupled spin chains, which can exhibit spin analogues of charge superconductivity and the integer quantum Hall effect. To drive spin current through those systems, we can apply an external-magnetic-field gradient, which acts as an electric field on the JW fermions [103]. We can also attach the spin system to heavy metals such as platinum, which can directly inject a spin current to proximate magnets via spin Hall effects [126]. Reciprocally, a spin current out of the system can be measured via inverse spin Hall effects by putting it next to heavy metals. Spin superconductivity and spin integer quantum Hall effects can be characterized by the zero resistance in spin flow through the bulk and along the boundary, respectively, when neglecting spin dissipation due to, e.g., thermal fluctuations or spin-lattice coupling.

From the results obtained for quantum spin chains, we expect that an array of weakly-coupled classical Heisenberg spin chains with the DM interaction in the presence of a strong external magnetic field would support the magnonic chiral edge modes by forming a topological magnon insulator [104] under suitable conditions. More broadly, we envision that weakly-coupled spin chains would serve as a versatile platform to engineer various spin-

related topological phases.

The authors thank Pramey Upadhyaya for insightful discussions. This work was supported by the Army Research Office under Contract No. 911NF-14-1-0016.

Chapter 5

Mechanical Actuation of Magnetic Domain-Wall Motion

We theoretically study the motion of a magnetic domain wall induced by transverse elastic waves in a one-dimensional magnetic wire, which respects both rotational and translational symmetries. By invoking the conservation of the associated total angular and linear momenta, we are able to derive the torque and the force on the domain wall exerted by the waves. We then show how ferromagnetic and antiferromagnetic domain walls can be driven by circularly- and linear-polarized waves, respectively. We envision that elastic waves may provide effective means to drive the dynamics of magnetic solitons in insulators.

5.1 Introduction

Phonons, quanta of elastic vibrations, are ubiquitous in condensed matter systems including magnets. Owing to their gapless nature, they can easily absorb energy from excited spins, thereby engendering the damping term in the description of spin dynamics [12]. Apart from this passive role, the idea of actively using phonons to induce magnetic dynamics has been recently gaining attention in spintronics. It has been experimentally demonstrated that acoustic pulses can induce coherent magnetization precession [127, 128] via spin-lattice

coupling [129]. Also excitation of elastic waves can generate spin currents [130, 131] and thereby drive magnetic bubbles [132].

A domain wall in an easy-axis magnet is one of the simplest and well-studied topological solitons [133], which has practical importance exemplified by the racetrack memory [48]. They can be driven by various means: a magnetic field [134], an electric field [135], a spin-polarized electric current [136–139], a temperature gradient [140, 141], or a spin wave [142, 143]. Moving domain walls have been known to generate and drag phonons, which in turn gives rise to the damping force on the walls [144]. This force increases as the domain wall approaches the speed of sound, which was pointed out as the origin of the plateau in the dependence of the domain-wall speed on an external field [145].

In this Letter, we study the reciprocal problem: actuation of the magnetic domain-wall motion via the phonon current, which can be injected by mechanical means. The stress-induced motion of a domain wall has been previously studied in Ref. [146], in which the domain wall is energetically driven by the axial stress gradient generated by the static voltage profile in piezoelectric materials. Differing from that, we focus on the effects of the dynamic phonon current on the domain wall via scattering. Specifically, we consider a one-dimensional magnetic wire with a coaxial easy-axis anisotropy, which can be realized by a single-crystalline iron nanowire embedded in a carbon nanotube [147]. It respects the rotational and translational symmetries and thus conserves the total angular and linear momenta. A magnetic domain wall breaks both symmetries, which opens channels for the exchange of both momenta with phonons. See Fig. 5.1 for an illustration of a domain-wall configuration for a ferromagnetic system. We show that the domain wall is birefringent for transverse waves and can thus act as a waveplate that alters the circular polarization—and thus the angular momentum—of phonons traveling through it. This change of phonons' angular momentum applies the torque on the domain wall. Reflection of phonons by the domain wall gives rise to the force acting on it. We study the domain-wall motion induced by the phononic torque and the force in ferromagnets and antiferromagnets.

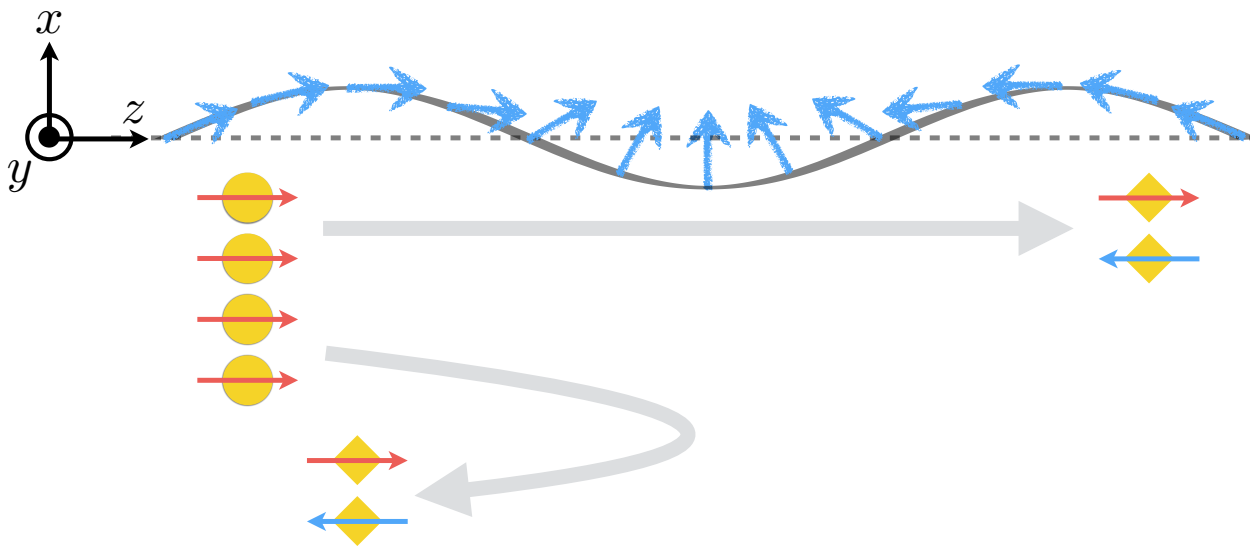

Figure 5.1: A schematic illustration of a ferromagnetic wire with a magnetic domain wall (shown by blue thick arrows) and a transverse elastic deformation (which is exaggerated for illustrative purposes). The yellow circles represent incoming phonons, quanta of elastic waves; the yellow diamonds represents transmitted and reflected phonons. The red (blue) arrows on circles represent phonons' angular momentum in the positive (negative) z direction. Phonons are injected from the left; some of them are reflected by the domain wall and thereby exert the force on it; some of the transmitted and reflected phonons change their angular momentum and thereby exert the torque on the wall.

5.2 Main Results

Our model system is a one-dimensional magnetic wire stretched along the global z axis by an external tension, in which the magnetic order parameter tends to align with the local orientation of the wire. The order parameter is the local spin angular-momentum density for ferromagnets and the local Néel order for antiferromagnets. For temperatures well below the ordering temperature, the local order parameter has the saturated magnitude and thus can be represented by the unit vector $\mathbf{n}(\zeta, t)$ pointing along its direction. Here, ζ is the internal coordinate of the lattice atoms along the wire. In this Letter, we are interested in the interaction between the magnetic soliton—domain wall—and the transverse vibrations of the wire, which are represented by $u(\zeta, t)$ and $v(\zeta, t)$ for the displacements of the atom at ζ in the lab-frame x and y direction, respectively [1]. We shall focus on small displacements by working to the quadratic order in u and v. In studying the dynamics of elastic waves, we shall assume that the dynamics of the magnetization is slow enough to be treated as static in the equations of motion for elastic waves, which would be valid if the speed of sound is much larger than that of magnons.

The potential energy that involves the magnetic order parameter is given by

$$U_{\rm m} = \int d\zeta \, \left[A\mathbf{n}'^2 + K\{1 - (\mathbf{n}\cdot\mathbf{t})^2\}\right]/2\,, \tag{5.2.1}$$

where the positive constants A and K are the exchange and anisotropy coefficients, respectively [2]. Here, $'$ is the derivative with respect to the intrinsic coordinate ζ; $\mathbf{t}(\zeta, t) \equiv (u', v', \sqrt{1 - u'^2 - v'^2})$ is the unit tangent vector of the wire. The magnetic anisotropy can be rooted in either the magneto-crystalline anisotropy or the shape anisotropy induced by

[1] By assuming that the Young's modulus is much larger than the applied tension, $E \gg \mathcal{T}$, we shall neglect longitudinal displacements by focusing on low-energy transverse modes [148–150].

[2] Transverse elastic deformations may affect the magnetic potential energy by modifying the geometry of the wire, which can be captured by an additional potential-energy term $\delta U_{\rm m} = \int d\zeta\, (u'^2 + v'^2)[\xi A\mathbf{n}'^2 + \nu K\{1 - (\mathbf{n}\cdot\mathbf{t})^2\}]/2$, where ξ and ν are the dimensionless parameters. This term modifies the strength of the potential for elastic waves in Eq. (5.3.1), $2\tilde{\kappa} \mapsto [2 - (\xi + \nu)]\tilde{\kappa}$ for u and $\tilde{\kappa} \mapsto [1 - (\xi + \nu)]\tilde{\kappa}$ for v, which does not change the elastic-wave-induced motion of the domain wall qualitatively.

dipolar interactions. When the wire is straight along the z axis, $u \equiv v \equiv 0$, there are two ground states: $\mathbf{n} \equiv \hat{\mathbf{z}}$ and $\mathbf{n} \equiv -\hat{\mathbf{z}}$. A domain wall is a stationary solution of $\delta_{\mathbf{n}} U_{\mathrm{m}} = 0$ that interpolates two ground states $\mathbf{n}(\zeta = \pm\infty) = \mp\hat{\mathbf{z}}$. It is given by [134]

$$n_x(\zeta) = \operatorname{sech}[(\zeta - Z)/\lambda] \cos\Phi \,, \tag{5.2.2a}$$

$$n_y(\zeta) = \operatorname{sech}[(\zeta - Z)/\lambda] \sin\Phi \,, \tag{5.2.2b}$$

$$n_z(\zeta) = -\tanh\left[(\zeta - Z)/\lambda\right] \,. \tag{5.2.2c}$$

Here, Z and Φ are the position and the azimuthal angle of the domain wall, respectively; $\lambda \equiv \sqrt{A/K}$ is the characteristic length scale of the problem, corresponding to the domain-wall width. Z and Φ parametrize two zero modes of the domain wall, which are associated with the breaking of the translational and spin-rotational symmetries. The dynamics of the position Z induced by the wire's transverse vibrations is of our main interest.

The linearized dynamics of the transverse displacements of the stretched wire can be described by the Lagrangian [148]

$$L_{\mathrm{e}} = \int d\zeta \, \left[\mu(\dot{u}^2 + \dot{v}^2) - \mathcal{T}(u'^2 + v'^2)\right]/2 \,, \tag{5.2.3}$$

where the positive constants μ and $\mathcal{T}$ are the mass density of the wire and the applied tension, respectively [3]. The equations of motion for u and v, that are derived from the Lagrangian L_{e} in conjunction with the potential energy U_{m} [Eq. (5.2.1)], are given by

$$\mu\ddot{u} - \left[\left\{\mathcal{T} + K(n_z^2 - n_x^2)\right\} u'\right]' = -K(n_z n_x)' \,, \tag{5.2.4a}$$

$$\mu\ddot{v} - \left[\left\{\mathcal{T} + K(n_z^2 - n_y^2)\right\} v'\right]' = -K(n_z n_y)' \,. \tag{5.2.4b}$$

For the uniform ground states, $\mathbf{n} \equiv \pm\hat{\mathbf{z}}$, the right-hand sides vanish and the tension is

[3] We neglect the bending energy $\propto (u'')^2$ [151] by assuming that the tension is strong so that the potential energy $\propto \mathcal{T}$ in L_{e} dominates over the bending energy.

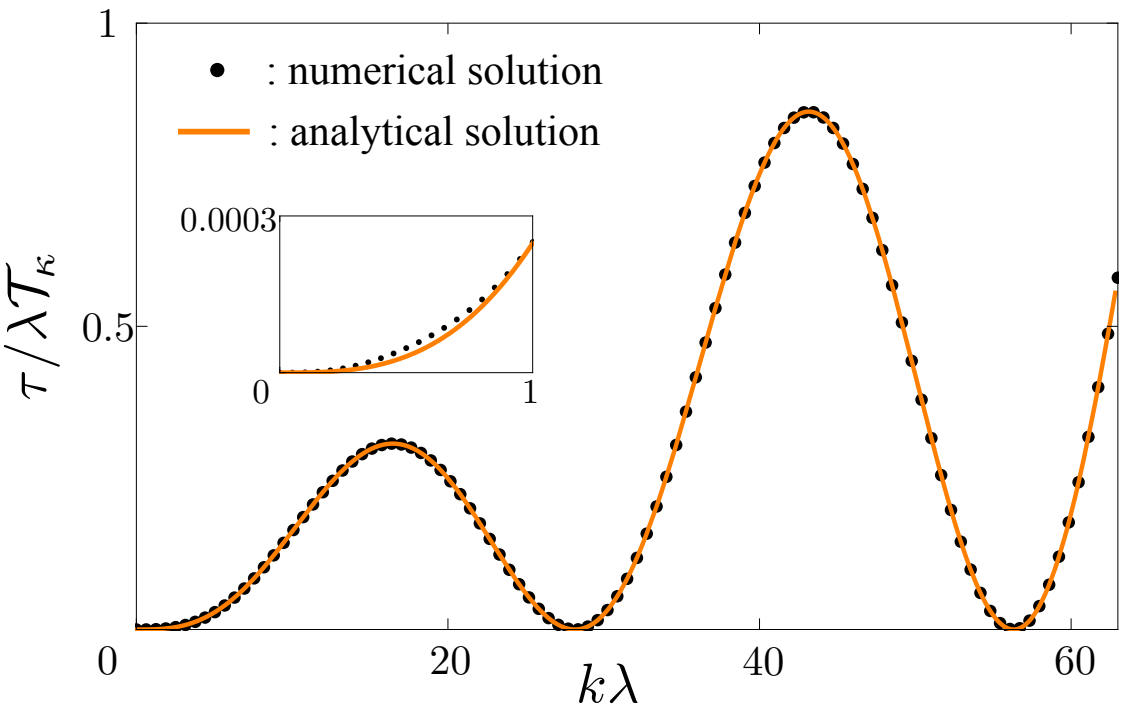

Figure 5.2: The torque τ on the domain wall by the circularly-polarized waves as a function of the wavenumber $k\lambda$ for the parameters $\kappa = 0.2$ and $a = \lambda/10$. The solid line is obtained with the analytical expression for τ in Eq. (5.2.5); the dots are obtained with τ in Eq. (5.4.2) calculated from numerical solutions of the differential equations (5.3.1). The inset shows a zoom-in at small wave vectors $k\lambda < 1$.

effectively increased from $\mathcal{T}$ to $\mathcal{T}_\kappa \equiv (1+\kappa)\mathcal{T}$ with $\kappa \equiv K/\mathcal{T}$. The dispersion relation is given by $\omega = \pm v_0 k$ with the speed $v_0 \equiv \sqrt{\mathcal{T}_\kappa/\mu}$. Using the propagating-wave solutions to the above equations in the presence of the domain wall, details of which will be shown later, we can derive the phononic torque and the force on the wall by invoking the conservation of the angular and linear momenta. The induced domain-wall speed is quadratic in the amplitude of waves, which allows us to assume that the domain wall is static in Eqs. (5.2.4) to the linear order in the amplitude [4].

The magnetic domain wall breaks the rotational and translational symmetries by selecting an azimuthal angle Φ and a position Z, respectively. Incoming elastic waves thereby scatters off the domain wall. By invoking the conservation of both momenta, we are able to derive

[4] In the quantum regime, the domain wall can be considered static only when its effective inertia is much larger than that of incoming phonons.

the torque τ and the force F on the domain wall. Let us present main features in the case of small-amplitude elastic waves, which allows us to neglect the backaction of the induced domain-wall motion on the elastic waves in Eqs. (5.2.4).

Let us present main features in the case of a small anisotropy $\kappa \ll 1$, which allows us to neglect the backaction of the induced domain-wall motion on the elastic waves in Eqs. (5.2.4).

First, circularly-polarized waves incoming from the left, $u(\zeta,t) = a\cos(k\zeta - \omega t)$ and $v(\zeta,t) = -a\sin(k\zeta - \omega t)$, exert the torque (i.e., the transfer of angular momentum) on the domain wall,

$$\tau \simeq \mathcal{T}_\kappa a^2 k[1 - \cos\{k\lambda \ln(1-\kappa)\}]\,, \tag{5.2.5}$$

for high-energy waves $k\lambda \gg 1$, which is obtained by the subtraction of the angular momentum current of the transmitted wave, $\mathcal{T}_\kappa a^2 k\cos\{k\lambda\ln(1-\kappa)\}$, from that of the incoming wave, $\mathcal{T}_\kappa a^2 k$. The physical origin of the torque can be understood as follows. From Eqs. (5.2.4), the domain wall locally modifies the tension for the u and v displacements by $K[1-2\,\mathrm{sech}^2(\zeta/\lambda)]$ and $K[1-\mathrm{sech}^2(\zeta/\lambda)]$, respectively. The v component thus propagates faster than the u component within the domain wall, which acts as a birefringent medium that can alter the polarization of the wave. The argument of the cosine function in Eq. (5.2.5) is the relative phase shift of u and v components of the transmitted wave, $\phi_{u,t} - \phi_{v,t} \simeq k\lambda\ln(1-\kappa)$. Figure 5.2 shows the torque τ as a function of the wavenumber $k\lambda$. Note that it oscillates as a function of $k\lambda$ with the period of $2\pi/\ln(1-\kappa)$. This torque by the elastic waves can drive ferromagnetic domain walls, analogous to the torque of spin waves [142]. The steady-state speed of the ferromagnetic domain wall is $V = \tau/2s$ [Eq. (5.5.2)] in the absence of damping, where $s \equiv \hbar S/\mathcal{V}$ is the saturated spin density ($\mathcal{V}$ is the volume per spin).

Secondly, linearly-polarized waves incoming from the left, $v(\zeta,t) = a\cos(k\zeta - \omega t)$ and $u(\zeta,t) \equiv 0$, exert no torque, but a finite force (i.e., the transfer of linear momentum) on the domain wall due to the reflection,

$$F \simeq \mathcal{T}_\kappa \kappa^2 \lambda^2 a^2 k^4\,, \tag{5.2.6}$$

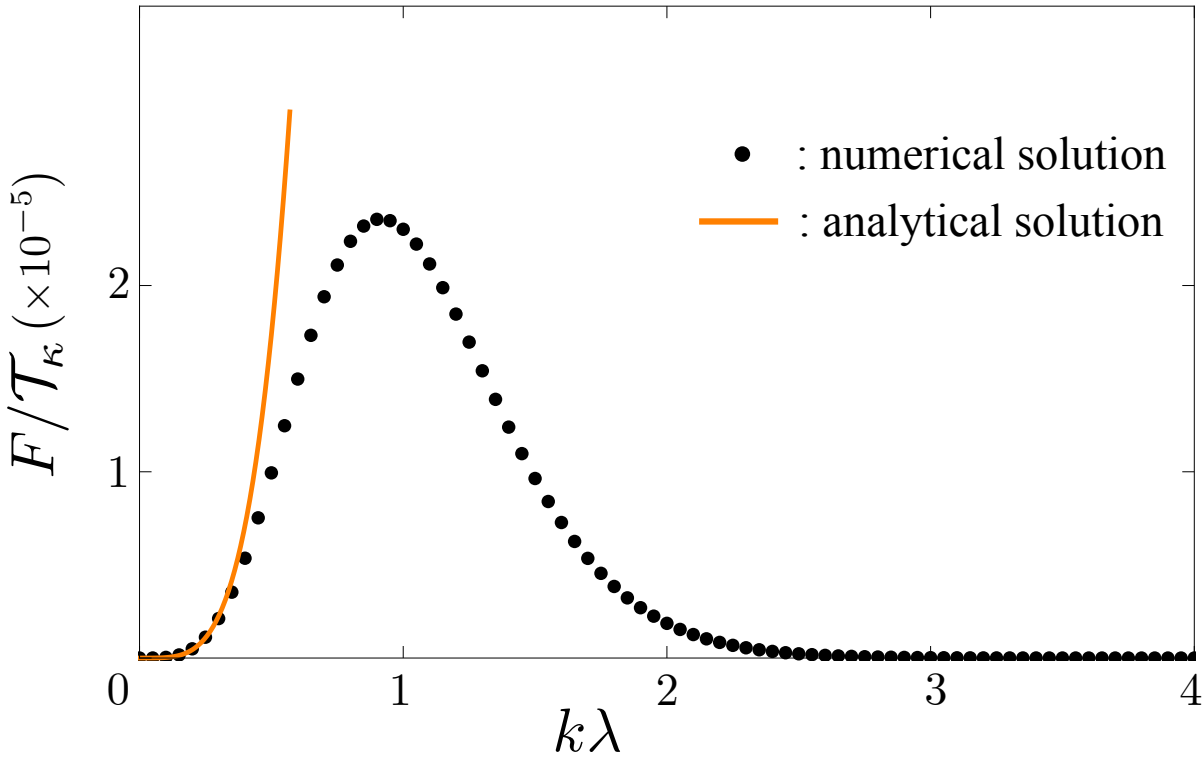

Figure 5.3: The force F on the domain wall exerted by the linearly-polarized waves perpendicular to the wall plane for the parameters $\kappa = 0.2$ and $a = \lambda/10$. The solid line is obtained with the analytical expression for F in Eq. (5.2.6); the dots are obtained with F in Eq. (5.4.3) calculated from numerical solutions of the differential equations (5.3.1).

for low-energy waves $k\lambda \ll 1$. It is the product of the pressure (i.e., the linear momentum current) of the incoming wave, $\mathcal{T}_\kappa a^2 k^2/2$, and twice the reflection probability, $2\kappa^2\lambda^2 k^2$. The reflection probability is exponentially small for high-energy waves $k\lambda \gg 1$, and so is the force. Figure 5.3 shows the force F as a function of the wavenumber $k\lambda$. This force of the elastic waves can drive antiferromagnetic domain walls, analogous to the force of spin waves [143,152]. The steady-state speed of the antiferromagnetic domain wall is $V = \lambda F/2\alpha s$ [Eq. (5.6.1)], where α is the Gilbert damping constant.

5.3 Transverse waves

Let us solve the differential equations (5.2.4) for u and v in the presence of the static domain wall given by Eqs. (5.2.2). A general solution is composed of static and dynamic components. A static one is determined by the right-hand sides of the equations [144,153], whereas dynamic components, which are of interest to us, are the propagating waves, for which we can neglect the right-hand sides. For the monochromatic solutions, i.e., $\propto \exp(-i\omega t)$, the equations are given by

$$\left[\left\{1 - 2\tilde{\kappa}\,\mathrm{sech}^2(\zeta/\lambda)\right\} u'\right]' = -k^2 u\,, \tag{5.3.1a}$$

$$\left[\left\{1 - \tilde{\kappa}\,\mathrm{sech}^2(\zeta/\lambda)\right\} v'\right]' = -k^2 v\,, \tag{5.3.1b}$$

with $k^2 \equiv \omega^2/v_0^2$ and $\tilde{\kappa} \equiv \kappa/(1+\kappa)$. We shall focus on solutions for v henceforth, from which we can obtain solutions for u by replacing $\tilde{\kappa}$ by $2\tilde{\kappa}$. For the given incoming-wave component, the solution far away from the wall can be characterized by four real numbers: the amplitude $t > 0$ and the phase-shift ϕ_t of the transmitted component and the amplitude $r > 0$ and the phase-shift ϕ_r of the reflected component:

$$v(\zeta) \propto \begin{cases} e^{ik\zeta} + re^{-ik\zeta + i\phi_r}\,, & \text{for } \zeta \ll -\lambda \\ te^{ik\zeta + i\phi_t}\,, & \text{for } \zeta \gg \lambda\,. \end{cases} \tag{5.3.2}$$

The equation can be transformed into a quantum-mechanic scattering problem by introducing a new coordinate η satisfying $d\zeta/d\eta = 1 - \tilde{\kappa}\ \mathrm{sech}^2(\zeta/\lambda)$:

$$\left[-\frac{d^2}{d\eta^2} + k^2\tilde{\kappa}\ \mathrm{sech}^2\,\frac{\zeta(\eta)}{\lambda}\right] v = k^2 v\,. \tag{5.3.3}$$

We obtain approximate solutions in the two extreme energy regimes. First, in the high-energy limit, $k\lambda \gg 1$, we use the Wentzel-Kramers-Brillouin approximation [154], within which the solution is $v(\zeta) \propto \exp\left[ik\int d\zeta\{1 - \tilde{\kappa}\ \mathrm{sech}^2(\zeta/\lambda)\}^{-1/2}\right]$ in the original coordinate ζ with the transmission amplitude $t = 1$. The phase shift of the transmitted wave is given by

$$\phi_t = k\int_{-\infty}^{\infty} \frac{d\zeta}{\sqrt{1 - \tilde{\kappa}\ \mathrm{sech}^2(\zeta/\lambda)}} = -k\lambda\ln(1-\tilde{\kappa})\,. \tag{5.3.4}$$

In the low-energy limit, we approximate the potential by the delta-function barrier with the height $h_k \equiv 2k^2\sqrt{\tilde{\kappa}/(1-\tilde{\kappa})}\arcsin\sqrt{\tilde{\kappa}}$ that is the spatial integral of the potential. After solving the scattering problem and going back to the original coordinate ζ, we obtain

$$r = \tilde{\kappa}k\lambda\,, \quad \phi_r = -\pi/2, \quad t = 1\,, \quad \phi_t = \tilde{\kappa}k\lambda\,, \tag{5.3.5}$$

to the first order in $k\lambda$. Note that for a small anisotropy, $\tilde{\kappa} \ll 1$, the phase shifts of the transmitted wave in the two regimes coincide: $-k\lambda\ln(1-\tilde{\kappa}) \simeq \tilde{\kappa}k\lambda$.

5.4 Torque and force.

In the uniform state, $\mathbf{n}(\zeta) \equiv \hat{\mathbf{z}}$, the effective Lagrangian density for the waves which includes the effect of the anisotropy is given by $\mathcal{L} = \mu(\dot{u}^2 + \dot{v}^2) - \mathcal{T}_\kappa(u'^2 + v'^2)$. Axial symmetry of the Lagrangian implies conservation of the corresponding angular momentum. The temporal and spatial components of the associated Nöther current [149, 152] are given by $\rho^s = \mu(u\dot{v} - v\dot{u})$ and $I^s = -\mathcal{T}_\kappa(uv' - vu')$, which are, respectively, the density and the current of the (orbital)

angular momentum [5]. We obtain the linear momentum density $T^{10} = -\mu\dot{u}u' + (u \to v)$ and the current $T^{11} = (\mu\dot{u}^2 + \mathcal{T}_\kappa u'^2)/2 + (u \to v)$ from the stress-energy tensor, $T^{\alpha\beta} \equiv \partial^\alpha u[\partial\mathcal{L}/\partial(\partial_\beta u)] + (u \to v) - \delta^{\alpha\beta}\mathcal{L}$ [149]. For monochromatic waves, $u(\zeta, t) = u_0 \cos(k\zeta - \omega t)$ and $v(\zeta, t) = v_0 \cos(k\zeta - \omega t + \Delta\phi)$, the angular and linear momentum currents are given by

$$I^s = \mathcal{T}_\kappa u_0 v_0 \sin(\Delta\phi)k\,, \quad T^{11} = \mathcal{T}_\kappa(u_0^2 + v_0^2)k^2/2\,. \tag{5.4.1}$$

An intuitive way to understand these momentum currents is to picture the elastic wave as a flux of phonons, particles carrying the angular momentum $\pm\hbar$ and the linear momentum $\hbar k$. For example, a circularly-polarized wave with $u_0 = v_0 = a$ and $\Delta\phi = \pi/2$ have $I^s = \mathcal{T}_\kappa a^2 k$ and $T^{11} = \mathcal{T}_\kappa a^2 k^2$; Their ratio is $T^{11}/I^s = k$, which is consistent with the particle picture.

Let us take an example of a circularly-polarized wave with $u_0 = v_0 = a$ and $\Delta\phi = \pi/2$. It has the angular and the linear momentum current, $I^s = \mathcal{T}_\kappa a^2 k$ and $T^{11} = \mathcal{T}_\kappa a^2 k^2$. We can obtain the number current from the linear momentum current by $T^{11}/\hbar k = \mathcal{T}_\kappa a^2 k/\hbar$. Comparison between the number current and the angular momentum current leads us to conclude that phonons in the wave has the angular momentum $+\hbar$ (polarized along the $\hat{\mathbf{z}}$ axis).

Let us now derive the torque and the force on the domain wall exerted by elastic waves. The torque is the difference of the angular momentum current I^s between the far left and far right of the domain wall; the force is the difference of the linear momentum current T^{11} between them. First, for the circularly-polarized incoming wave, $u(\zeta, t) = a\cos(k\zeta - \omega t)$ and $v(\zeta, t) = -a\sin(k\zeta - \omega t)$, the time-averaged torque and force are given by

$$\tau = \mathcal{T}_\kappa a^2(1 - t_u t_v \cos\Delta\phi_t - r_u r_v \cos\Delta\phi_r)k\,, \tag{5.4.2}$$

$$F = \mathcal{T}_\kappa a^2(r_u^2 + r_v^2)k^2\,, \tag{5.4.3}$$

[5] Ref. [155] showed that phonons in magnetic crystals can have nonzero orbital angular momentum in equilibrium.

where t_u and t_v are respectively the transmission amplitudes of the u and v components (and similarly r_u and r_v for the reflection amplitudes) and $\Delta\phi_t$ is the relative phase shift of the transmitted u and v components (and similarly $\Delta\phi_r$ for the reflected wave). Equation (5.2.5) for τ is the reflectionless limit of Eq. (5.4.2), corresponding to $k\lambda \gg 1$. Secondly, for the linearly-polarized incoming wave, $v(\zeta, t) = a\cos(k\zeta - \omega t)$, the torque vanishes and the force is given by

$$F = \mathcal{T}_\kappa a^2 r_v^2 k^2 \,. \tag{5.4.4}$$

5.5 Ferromagnetic domain wall

The dynamics of the ferromagnet is described by the Lagrangian [156], $L = s\int d\zeta\, \mathbf{a}(\mathbf{n})\cdot\mathbf{n} - U[\mathbf{n}]$, where $\mathbf{a}(\mathbf{n})$ is a vector potential of a magnetic monopole, $\boldsymbol{\nabla}_\mathbf{n}\times\mathbf{a} = \mathbf{n}$. The angular and linear momenta of the domain wall [Eqs. (5.2.2)] are given by, respectively, $J = J_0 + 2sZ$ and $P = P_0 - 2s\Phi$, where J_0 and P_0 are arbitrary [157, 158]. Viscous losses can be represented by the Rayleigh dissipation function [149] $R = \alpha s\int d\zeta\, \dot{\mathbf{n}}^2/2$, where α is Gilbert's damping constant [12]. By plugging the domain-wall solution, we obtain $R = \alpha s(\lambda\dot{\Phi}^2 + \dot{X}^2/\lambda)$. The conservations of the total angular and linear momenta yield

$$\tau = \dot{J} + 2\alpha s\lambda\dot{\Phi}\,, \quad F = \dot{P} + 2\alpha s\dot{Z}/\lambda\,. \tag{5.5.1}$$

The steady-state velocity $V = \dot{Z}$ is given by

$$V = \frac{\tau + \alpha\lambda F}{2(1+\alpha^2)s}\,. \tag{5.5.2}$$

5.6 Antiferromagnetic domain wall

The dynamics of the antiferromagnet is described by the Lagrangian, $L = \chi\int d\zeta\, \dot{\mathbf{n}}^2/2 - U[\mathbf{n}]$, where χ quantifies inertia of the order parameter [159,160]. The Rayleigh dissipation function

is $R = \alpha s \int d\zeta\, \dot{\mathbf{n}}^2/2$ [161]. For slow dynamics, the angular and linear momenta of the domain wall are respectively given by $J = I\dot{\Phi}$ and $P = M\dot{Z}$, where $I \equiv 2\chi\lambda$ and $M \equiv 2\chi/\lambda$ are the moment of inertia and the mass of a static domain wall [152]. Their equations of motion are same as Eqs. (5.5.1). The steady-state velocity $\dot{Z}(t) \to V$ is given by

$$V = \frac{\lambda F}{2\alpha s}\,. \tag{5.6.1}$$

5.7 Discussion

For experiments, linearly polarized elastic waves can be coherently excited by attaching a piezoelectric transducer to the magnetic wire, as done in Refs. [162, 163] to probe the magnetoacoustic Faraday effect [129]. Coherent excitation of circularly-polarized waves can be generated, for example, by exciting two linearly polarized modes with the fixed relative phase of $\pi/2$.

Let us make a quantitative estimate for the speed of the domain-wall in ferromagnets, $V = \tau/2s$ [Eq. (5.5.2)] in the zero-damping limit $\alpha = 0$ at the maximum efficiency of the phononic torque, i.e., $\tau = 2\mathcal{T}_\kappa a^2 k$ [Eq. (5.2.5)]. We take the parameters of iron for the magnet, the saturation magnetization $M_s = 2 \times 10^6$ A/m and the mass density $\rho = 7 \times 10^3$ kg/m^3 [164], and the parameter of lead zirconate titanate for the piezoelectric strain constant $d = 10^{-10}$ m/V [146]. For the iron wire of the cross-sectional area $\mathcal{A} = 20$ nm^2 [147] subjected to the tension $\mathcal{T} = 10^{-3}$ N, the application of the electric field $E = 1$ V/mm rotating at the frequency 10 MHz across the piezoelectric transducer of length $L = 100$ nm yields the speed $V \approx 40$ m/s (assuming the perfect coupling of stress between the transducer and the wire), which is comparable to the domain-wall speed by the spin-polarized electric current [48] and by the magnon current [142].

We have neglected the magnetoacoustic Faraday effect [162] as well as its inverse effect [165], which are absent in the static treatment of the magnetization according to the energy $U_{\rm m}$ (5.2.1) that is even under magnetization reversal. The effects might be present when the

magnetization is made dynamic, but it is suppressed when the magnetic and the acoustic resonances are significantly mismatched [129]. These effects, in principle, can influence the domain-wall motion. In particular, via the inverse effect, the circularly polarized elastic waves can induce the effective magnetic field along the axial direction and drive the ferromagnetic domain wall by contributing to the force F in Eq. (5.5.2) [134]. In the zero-damping limit $\alpha = 0$, however, this contribution can be neglected.

We are grateful for discussions with Héctor Ochoa and Ricardo Zarzuela, who helped us to formulate the problem. We also thank the anonymous referees, whose comments and questions led to the significant improvement of the Letter. This work was supported by the Army Research Office under Contract No. 911NF-14-1-0016.

Chapter 6

Evolution of the quantum Hall bulk spectrum into chiral edge states

One of the most intriguing and fundamental properties of topological systems is the correspondence between the conducting edge states and the gapped bulk spectrum. Here, we use a GaAs cleaved edge quantum wire to perform momentum-resolved spectroscopy of the quantum Hall edge states in a tunnel-coupled 2D electron gas. This reveals the momentum and position of the edge states with unprecedented precision and shows the evolution from very low magnetic fields all the way to high fields where depopulation occurs. We present consistent analytical and numerical models, inferring the edge states from the well known bulk spectrum, finding excellent agreement with the experiment – thus providing direct evidence for the bulk to edge correspondence. In addition, we observe various features beyond the single-particle picture, such as Fermi level pinning, exchange-enhanced spin splitting and signatures of edge-state reconstruction.

6.1 Introduction

Systems with topologically protected surface states, such as the quantum spin Hall insulator [166, 167] and many other topological insulators, are currently attracting great interest. Among the topological states, the integer quantum Hall effect [168] stands out since it was first discovered. It is the most simple case out of which others have emerged, and thus serves as a paradigmatic system. Accessing the surface states in a topological system separately and independently, however, has proven to be challenging for a number of reasons, including disorder, insufficient resolution or remnant bulk conductivity contaminating transport experiments. Local probes, such as scanning single electron transistors, could in principle overcome the bulk conductivity problem and have been intensely investigated in the context of quantum Hall systems [169–178]. However, moderate spatial resolution and the requirement of large magnetic fields for discriminating among individual edge states have limited existing experiments to low filling factors and prevented tracking the evolution of quantum hall edges all the way down to low fields.

Previously, tunneling spectroscopy of cleaved edge overgrowth wires has established the system as one of the best realizations of a 1D ballistic conductor, exhibiting distinct signatures such as quantized conductance [179], spin-charge separation [180], charge fractionalization [181] and indication of helical nuclear order induced by the strongly interacting electrons [182, 183]. Here, we use a vector magnet to independently control two orthogonal magnetic fields: one to form quantum Hall edge states and another to perform tunneling spectroscopy.

In this work, we use momentum resolved tunneling spectroscopy to track the guiding center (GC) positions of the quantum Hall edge states with nanometer precision. Over the magnetic field evolution, we observe first magnetic compression towards the sample edge, and then, at higher fields, motion into the bulk and magnetic depopulation of Landau levels (LLs). Note that in this work we are studying integer quantum Hall edge states

and not the spin Hall effect or any other topological state. However, this technique is also applicable to the latter states. Using both an analytical model and numerical solutions for the evolution of edge states in the limit of hard wall confinement [184–186], we are able to match very well the tunneling spectroscopy fingerprint of the conducting edge states from the topologically gapped bulk phase and hence reveal their direct correspondence. Individual edge modes [187–189] are discernible down to unprecedented low magnetic fields $B_z \approx 10\,\mathrm{mT}$, where the bulk filling factor ν is about 500. Furthermore, we observe the chiral nature of edge states, as well as Fermi level pinning effects. In addition, interactions lead to signatures of edge reconstruction and exchange-enhanced spin-splitting at large in-plane magnetic fields. We emphasize that this spectroscopy is done at zero bias, thus eliminating heating or lifetime effects.

6.2 Results

6.2.1 Integer quantum Hall edge states for the hard wall confinement

A magnetic field B_z, applied perpendicular to a 2D electron gas (2DEG), quenches the kinetic energy of free electrons and condenses them into discrete LLs that are energetically separated by the cyclotron energy $\hbar\omega_\mathrm{c}$. Here, $\omega_\mathrm{c} = eB_z/m^*$ denotes the cyclotron frequency, e the elementary charge, $\hbar$ the reduced Planck constant, and m^* the effective electron mass. Upon approaching the sample edge the electrostatic confinement potential lifts LLs in energy and causes them to intersect with the Fermi energy, thereby forming a corresponding edge state for each bulk LL, see Fig. 6.1a and Supplementary Fig. 4. Here, we use the Landau gauge (vector potential $\boldsymbol{A} = 0$ at the edge), where the momentum k_x along the quantum wires is a good quantum number that fully characterizes each state. Given k_x, all other quantities may be calculated, such as the wave function center of mass (CM) as well as the GC position $Y = k_x l_B^2$, where $l_B = \sqrt{\hbar/(eB_z)}$ denotes the magnetic length. Throughout the

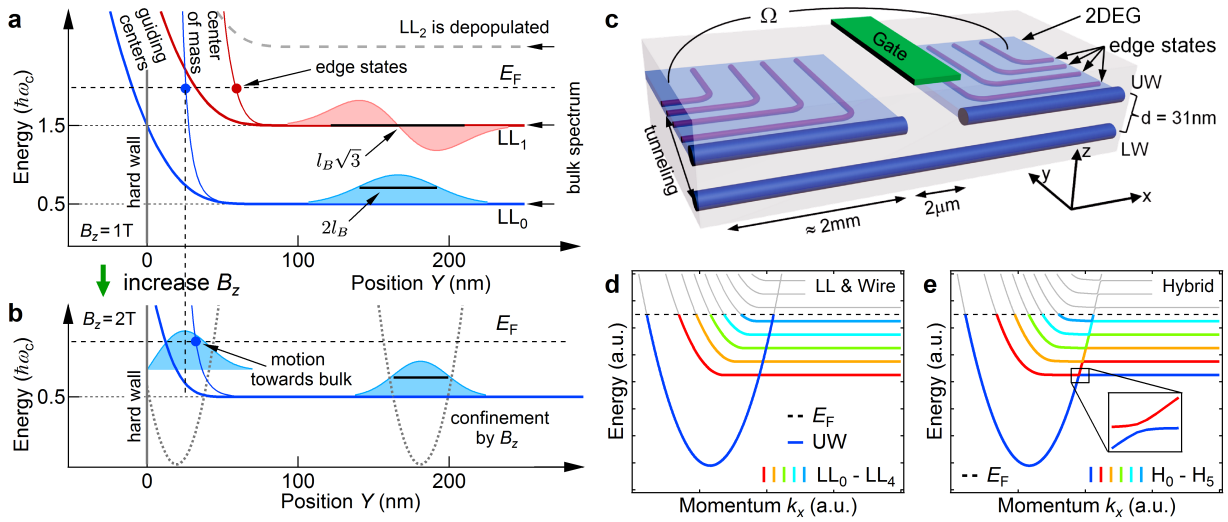

Figure 6.1: **Bulk to edge correspondence.** **a,** Energy evolution of the center of mass (CM) position (thin blue/red curves) and the guiding center (GC) position (bold blue/red curves) for the first two Landau levels LL_0 and LL_1. Here, LL_2 is above the Fermi energy and is depopulated. The confinement (hard wall) lifts the bulk LLs in energy, resulting in corresponding edge states (solid circles) when the CM is crossing the Fermi energy E_F. Note that the Fermi energy shown here is lower than in the experiment. **b,** Same as **a** for larger magnetic field B_z, where the width $2\sigma_n = 2l_B\sqrt{2n+1}$ of LL_n is squeezed and LL_1 was depopulated, with magnetic length l_B. **c,** Coordinate system (black) and sample schematic, showing the 2DEG in light blue, upper and lower quantum wire (UW/LW) in dark blue, top gate in green, and CM for integer quantum Hall edge states in purple. Ω indicates the conductance measurement. **d,** Simplified UW and LL dispersions calculated for independent triangular and hard wall confinement. **e,** Calculated dispersion for the combined confinement potential, resulting in hybridized states H_n with avoided crossings (see inset). Here, the bulk LL_0 transforms into the UW mode at the sample edge. Gray segments indicate empty states, colored ones are filled.

paper, the filling factor is defined as $\nu = 2n + g$, where $n = 0, 1, 2, ...$ is the orbital Landau level index, and $0 \leq g < 2$ is the spin occupancy.

At elevated B_z, shown in Fig. 6.1b, the cyclotron splitting is enhanced. As a consequence the highest LLs are energetically lifted above the Fermi energy and thus magnetically depopulated of electrons, compare Fig. 6.1a and b. In addition, increasing B_z reduces the magnetic length, thereby squeezing the remaining LL wave functions by magnetic compression and moving the corresponding edge states closer to the sample edge. This holds up to a certain point, when the edge state starts suddenly moving back into the bulk just before being magnetically depopulated, see Fig. 6.1b.

A sample schematic is depicted in Fig. 6.1c and consists of two parallel GaAs quantum wells, separated by a thin AlGaAs tunnel barrier. The upper quantum well hosts a high mobility 2DEG, while the bulk of the lower quantum well remains unpopulated. Cleavage of the sample and subsequent overgrowth results in strongly confined 1D-channels in both quantum wells (see methods section and refs. [179–181, 190–196] for more details), termed upper wire (UW) and lower wire (LW) in the following. The LW is used as a tunnel probe to spectroscopically image the integer quantum Hall edge states of the upper quantum well at effectively zero bias voltage.

A simplified picture for the complete dispersion for the upper system is shown in Fig. 6.1d. It consists of a single localized wire mode UW (dark blue), resulting from the triangular confinement at the sample edge, and the LL spectrum in presence of hard wall confinement and perpendicular magnetic field B_z. Solving the combined electrostatic problem (hard wall confinement with triangular potential near the edge) hybridizes the LL spectrum and quantum wire modes at commensurate conditions where energy and momentum are matched, see Fig. 6.1e. As a consequence the bulk LL_0 transforms into the lowest quantum wire mode at the sample edge. While each LL like edge state in Fig. 6.1e acquires an additional node in the wave function in comparison to the hard wall spectrum of Fig. 6.1d, the intersection with the Fermi energy E_F is hardly changed [197,198], giving almost the same effective momentum

k_x. Therefore, the simplified dispersion of Fig. 6.1d is used in the following to describe the magnetic field evolution of edge states.

The tunneling regime is obtained by setting the top gate in Fig. 6.1c to deplete the 2DEG and all UW modes beneath it while preserving a single conducting mode in the LW. This divides the upper system electrically into two halves but preserves tunnel coupling on each side to the LW. Due to translational invariance of UW and LW (away from the top gate, where tunneling occurs), momentum is conserved during the tunneling event, and can be controlled by means of the Lorentz force. In particular, in presence of an in-plane magnetic field B_y applied perpendicular to the plane spanned by the two wires (see coordinate system in Fig. 6.1c), tunneling electrons experience a momentum kick $\Delta k_x = -edB_y/\hbar$ along the x-direction of free propagation, thus effectively shifting the wire dispersions with respect to each other [180, 181, 193, 194]. Here, d denotes the tunneling distance along the z-direction. The resulting zero-bias tunneling conductance is large whenever Fermi-points of upper and lower system coincide, see also Supplementary Fig.1a. In a similar fashion, each LW mode can also be brought into resonance with any given LL. However, in contrast to the quantum wires, the effective momentum of edge modes $k_{x,\mathrm{LL_n}}$ of the LLs depends on B_z.

6.2.2 Formation and evolution of the edge states

Fig. 6.2 shows the measured differential tunneling conductance as a function of magnetic fields B_z and B_y. Two horizontal features are visible that correspond to resonant tunneling (energy and momentum conservation) between co-propagating electrons of the first upper and lower wire mode, $\mathrm{UW_1}$ and $\mathrm{LW_1}$, respectively. Since the electron density in $\mathrm{UW_1}$ and $\mathrm{LW_1}$ is very similar, only little momentum transfer and correspondingly small $|B_y|$ is required to bring the modes into resonance. These resonances are independent of B_z because the Y coordinates of both $\mathrm{UW_1}$ and $\mathrm{LW_1}$ modes are very similar. In addition to wire-wire tunneling, extensively studied in the past [180,181,193–196], sharp tunneling resonances of a different origin [187–189] are observed that split into fans of discrete curves in presence of a

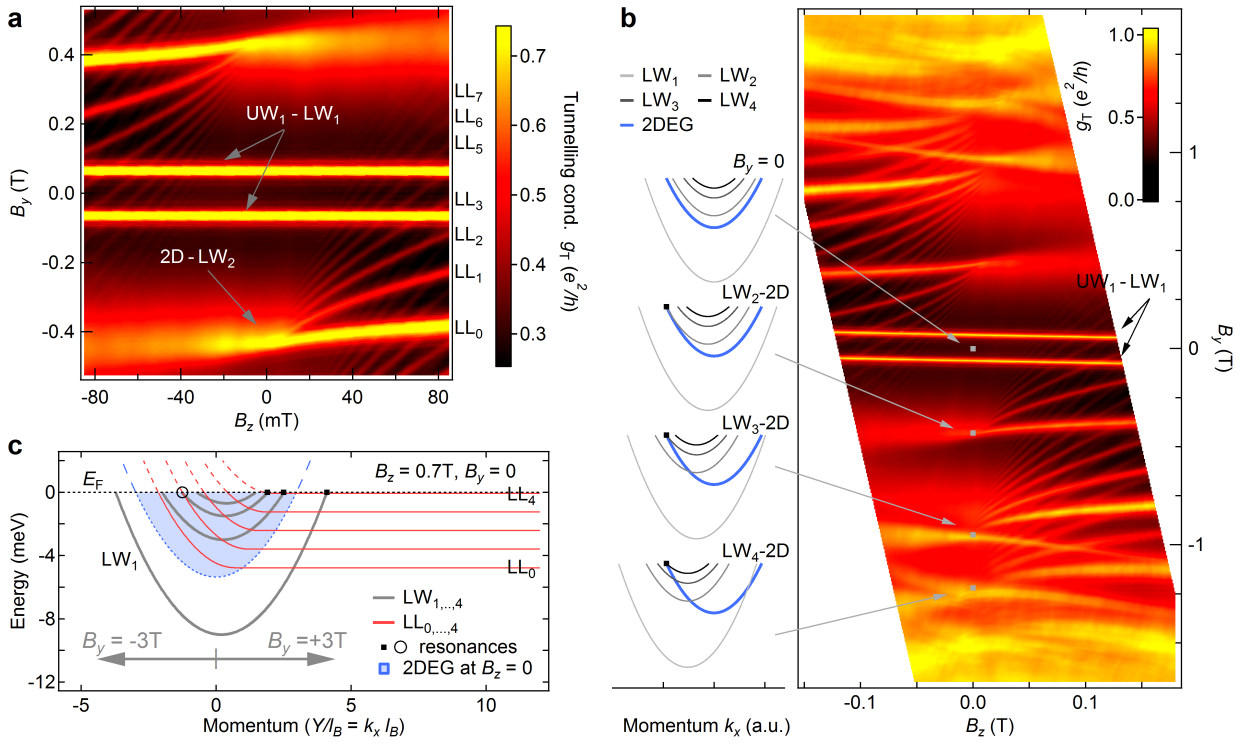

Figure 6.2: **Formation and B-field evolution of the chiral integer quantum Hall edge states. a,** Differential tunneling conductance as a function of in-plane magnetic field B_y and perpendicular magnetic field B_z at $\approx 10\,\mathrm{mK}$. The 2D-wire transitions break up into multiple curves and fan out with increasing B_z, see also Supplementary Fig. 2. Horizontal resonances at small $|B_y|$, associated with wire-wire tunneling, are not affected by B_z. **b**, Larger B_y range than **a**, showing 6 fans corresponding to tunneling to modes LW_2, LW_3, and LW_4. Due to the chiral nature of the states, the fans are not seen in the data when only B_z is reversed. The sketches depict the resonance condition (black dots) at $B_z = 0$. **c**, Schematic representation of quantum wire (gray) to LL (red) tunneling at $B_z = 0.7\,\mathrm{T}$. B_y shifts the lower wire dispersion in relation to the LLs, as indicated by gray arrows of corresponding length. The blue filled parabola indicates the 2DEG dispersion for $B_z = 0$, projected onto the k_x axis. Black dots and black circle indicate resonant tunneling to bulk states and edge state, respectively.

perpendicular field and separate with increasing field strength. For each fan, about 10 curves can be resolved down to $B_z \gtrsim 10\,\mathrm{mT}$, see Fig. 6.2. As we will show, these fans correspond to resonant tunneling between quantum Hall edge states and the LW modes which are acting as a momentum selective spectrometer. The fan structures observed here track the momentum evolution of edge states with B_z and thereby produce a fingerprint of the conducting edge states. This is in contrast to the conventional Landau fan that simply is an expression of the bulk filling factor as a function of 2DEG density and B_z.

The wire modes are supporting states propagating in both negative and positive x-direction, irrespective of the perpendicular field, and give transitions extending over both positive and negative B_z, see also Supplementary Fig. 6.1. The quantum Hall edge states, on the other hand, are chiral and are thus propagating only in one direction for a chosen sign of B_z along a given edge. The corresponding LL dispersions are therefore not symmetric under reversal of k_x, and the fan structures become directional. Indeed, the fans are seen only for one sign of B_z around a given B_y, e.g. in the lower right in Fig. 6.2a but not the lower left. The opposite sign of B_z also supports a fan but only when B_y is inverted at the same time, i.e. when the total B-field is switching sign (Onsager's reciprocity [199]), see upper left in Fig. 6.2a. This directly indicates the chiral nature of these edge states.

Besides fan structures in Fig. 6.2a, there are additional fans originating at different B_y values, see Fig. 6.2b where a larger field range is displayed. These other fans result from tunneling to other modes of the LW. Since each of the different modes in the LW has a different density and thus a different Fermi momentum, an overall momentum shift results which displaces the fans along B_y, as illustrated in the sketches of Fig. 6.2b, where the resonance condition at $B_z = 0$ is shown (origin of the fans).

In order to quantitatively understand the field evolution of the fan structures, the LL dispersions have to be considered, which depend on the electrostatics at the edge [200–207]. For the present samples, the cleavage exposes an atomically sharp edge, that is immediately overgrown by means of lattice matched molecular beam epitaxy [190, 191]. The resulting

hard wall confinement potential gives rise to the LL dispersions of Fig. 6.2c (red) [184, 186], shown along with the quantum wire modes in the lower well (gray) and the 2DEG at $B_z = 0$ (blue). Lowering B_z reduces the bulk LL energy splitting $\hbar\omega_c$ and hence introduces a more dense LL structure while leaving the LW modes unaffected (due to their strong transverse confinement). The in-plane magnetic field B_y, on the other hand, is assumed to not directly affect the LLs, but only shift their dispersion in relation to the LW.

The fan structures at positive B_Z in Fig. 6.2b can then be understood in terms of momentum conserving edge state tunneling using one of the LW left Fermi points as a spectrometer, see Fig. 6.2c, where the case of LW3 is marked with an open circle. Thus, each fan represents a map of the momenta of the LL edge states at the Fermi energy, and thus, via the GC-momentum relation $Y = k_x l_B^2$, a precise map of the GC positions of the edge states. Upon approaching $B_z = 0$, the effective momentum of edge states, i.e. the intersection of LLs with the chemical potential, approaches the $B_z = 0$ Fermi wave vector $-k_{\mathrm{F,2D}}$ of the 2DEG. During this process edge states associated with LLs of increasing orbital index subsequently come into co-propagating resonance with LW_2 at $B_y = 0$.

In the following section, the range in perpendicular magnetic field is extended (Fig. 6.3) in order to study the field evolution of edge states and their magnetic depopulation at large B_z. For better visibility, we plot the second derivative with respect to B_y of the differential tunnel conductance in Fig. 6.3a. A large number of interpenetrating resonances are visible, extracted in Fig. 6.3b for clarity, and grouped into bundles according to their different origin, i.e. red, black, and light blue data indicate co-propagating tunneling to the first three LW modes, LW_1, LW_2, and LW_3, respectively. The LL edge states can also be mapped in a counter-propagating fashion (Fig. 6.3c), e.g. where the wire state and edge states are propagating in opposite directions. To achieve momentum conservation in this case, a relatively large momentum kick needs to be provided by the magnetic field, and these transitions thus appear at larger B_y.

In addition to edge state−wire tunneling, intra−wire transitions are seen and color coded

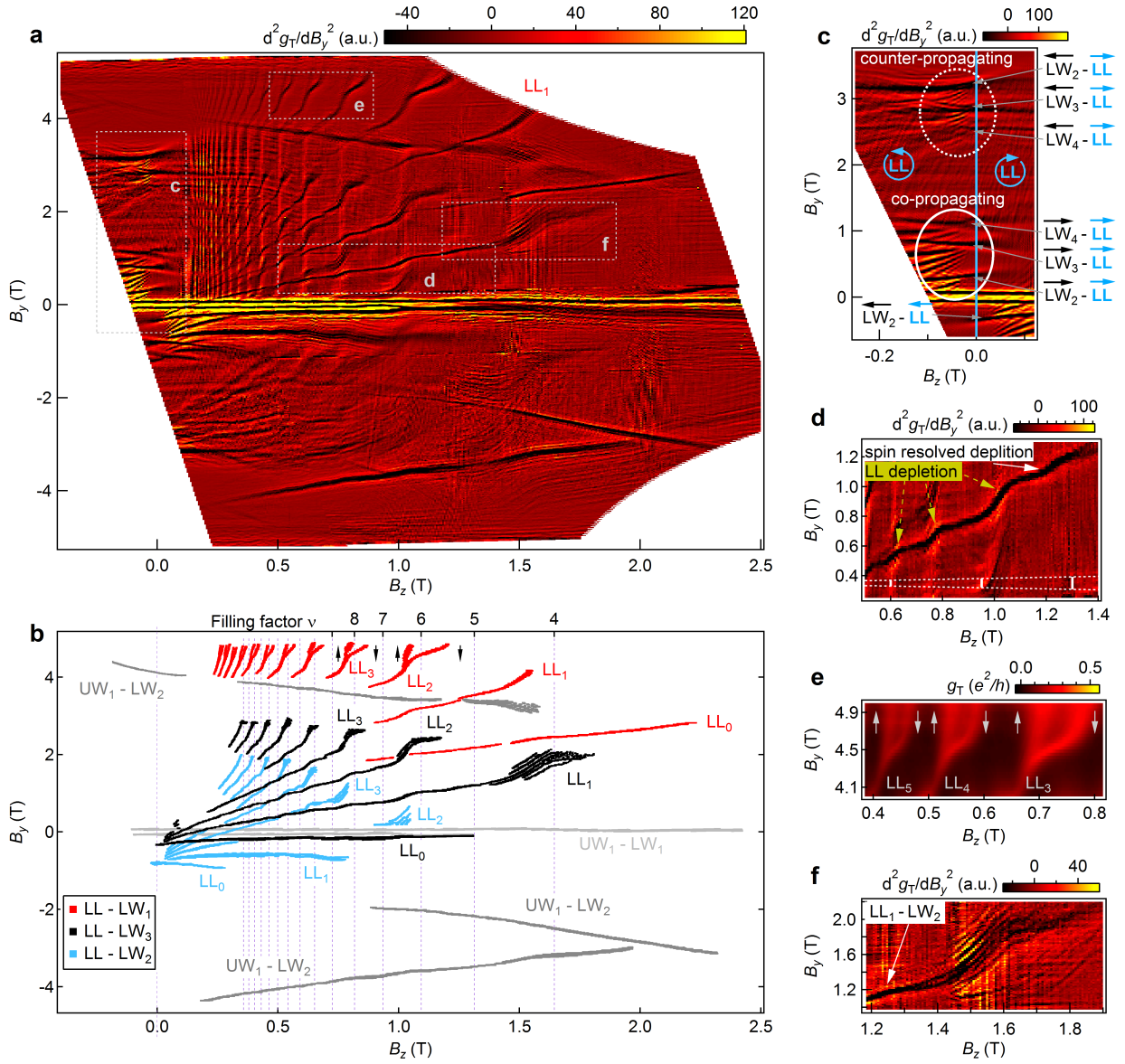

Figure 6.3: **Magnetic depopulation and spin splitting of integer quantum Hall edge states. a,** Second derivative with respect to B_y of the differential tunnel conductance (d^2g_T/dB_y^2) as a function of magnetic fields B_y and B_z. **b**, Extracted resonance positions from **a**. Red, black, and light blue data correspond to tunneling between edge modes and the first (LW_1), second (LW_2) and third (LW_3) lower wire mode. **c,d,e,f,** Zoom in of **a** for regions of interest: **c,** Landau fans for $B_z < 0$ (counter-clockwise edge states $\Leftrightarrow$ right moving edge state at cleaved edge), imaged with co-propagating (white solid ellipse) and counter-propagating wire modes (white dashed ellipse).**d,** Jumps in the resonance position whenever the bulk filling changes. The three vertical bars of growing height indicate a distance of 2 nm in real space. The height ΔB_y of the bar is given by $\Delta B_y = \Delta Y B_z/d$, where ΔY is the distance in real space. Thus, the real space resolution is improving with increasing magnetic field B_z. **e,** LL spin splitting clearly visible even in undifferentiated raw data (tunneling conductance g_T). **f,** branching out of resonances at the transition to magnetic depopulation.

in gray in Fig. 6.3b. As the wave functions for LW_1 and UW_1 are very similar, their CM positions nearly sit on top of each other and hence there is no resulting momentum kick $\Delta k_x = e\Delta y B_z/\hbar$ due to the perpendicular field. Here, Δy denotes their lateral displacement. As a consequence, the corresponding resonances (light gray) appear as horizontal lines. In contrast to this, transitions involving different wire modes, e.g. UW_2 and LW_1 (dark gray data in Fig. 6.3b), appear with a slope that reflects the different center of mass positions of the participating wave functions.

Returning to LL tunneling, we note a few important points. First, all LL resonances terminate on the right end at a specific bulk filling factor when magnetic depopulation removes the corresponding edge state from the sample, clearly seen for the black data in Fig. 6.3b. In particular, tunneling involving LL_2 with $n = 2$ is observed up to $B_z \approx 1.1\,\mathrm{T}$, terminating at the corresponding bulk filling factor $\nu = 6$, labeled on the top axes in Fig. 6.3b. Here, spin occupancy $g = 2$ because of a spin-unresolved case. The resonances for LL_3 with $n = 3$ are already lost above $B_z \approx 0.8$ at $\nu = 8$, independent of which LW mode is used as a spectrometer (compare red, black and light blue data in Fig. 6.3b).

6.2.3 Spin splitting and Landau level depopulation

A set of bright vertical features appears in the upper half of Fig. 6.3a (corresponding to the dashed vertical lines of integer filing factors in Fig. 6.3b), whose position is coincident with the disappearance of LL resonances. These features are even more visible in Supplementary Fig. 5. These result from probing the flat part of the LL dispersion i.e. they reflect the bulk filling factor, and account for the majority of the measured tunneling signal in Fig. 6.3 prior to differentiation of the data. For example at $B_z = 0.7\,\mathrm{T}$, shown in the level schematics of Fig. 6.2c, LL_4 is aligned with the chemical potential causing a resonance with the right Fermi-points of LW_1, LW_2, and LW_3 as indicated with black dots. While applying a positive in-plane magnetic field shifts the LW dispersions to the right and hence preserves resonant tunneling, this condition is lost for sufficiently negative B_y. Consequently, the vertical lines,

corresponding to magnetic depopulation of a LL in the bulk, appear predominantly at positive B_y.

Beyond the vertical lines, the smooth evolution of LL tunneling resonances from Fig. 6.2 develops shoulder-like structures at larger B_z, clearly seen in Fig. 6.3d. The shoulders appear exactly at the transition between bulk filling factors (vertical lines in Fig. 6.3b) and are attributed to Fermi level pinning to LLs and impurity states, respectively, previously only accessible through investigation of the bulk 2DEG properties [208, 209]. Here, we also note that the momentum resolution and the corresponding real space resolution of this spectroscopy technique improves with perpendicular magnetic field (white bars in Fig. 6.3d) and reaches the nanometer range for fields above 1 T. The resonance width depends on the degree to which momentum conservation is broken during tunneling, i.e. breaking of translational symmetry due to disorder and the finite size of the tunneling region. Finally, also, any variation of the tunneling distance between the upper and lower system, such as single-atomic steps in the growth plane or other crystal defects, will add to the observed broadening.

While each LL carries two spin resolved sub-bands, energetically split by the total Zeeman energy given by magnetic fields B_z and B_y, the corresponding difference in Fermi wave vectors is too small to be resolved by means of this spectroscopic method. However, at large in-plane magnetic fields, the interplay between Hartree term and exchange interactions [210] may lead to the formation of spin polarized strips where spin split sub-bands are also separated in real space [211]. As a consequence, tunneling resonances split up for the red data in Fig. 6.3e and the spectroscopy becomes spin selective.

6.2.4 Analytical model of resonant tunneling

In the last part of this article, we develop an analytical model [184, 185, 189, 197], and in addition provide numerical predictions (see supplement) for the evolution of LLs in the limit of hard wall confinement using a 1D single-particle Schrödinger solver. The perpendicular magnetic field introduces an additional local parabolic confinement, centered at each GC

position Y, hence condensing bulk electrons into discrete LLs with well known Hermite-Gaussian wave functions. We assume that upon approaching the hard wall, LLs remain at their bulk energy $E_n^{\mathrm{bulk}} = \hbar\omega_{\mathrm{c}}\left(n+\frac{1}{2}\right)$ until the tail of the wave function intersects with the hard wall ($Y \approx \sigma_n$ for $\mathrm{LL_n}$, with σ_n the half width of the LL wave function). When moving Y even closer to the edge or beyond, the hard wall retains the wave functions within the sample, thus separating in space the GC position $Y = k_x l_B^2$ and the wave function center of mass (CM) position, see Fig. 6.1a,b and Fig. 6.4a. As as consequence, LLs acquire kinetic energy and are simply lifted up the parabolic magnetic confinement until they cross the Fermi energy, thereby forming the conducting edge states (Figs. 6.1a,b and Supplementary Figs. 3 and 4). Using these approximations, the LL dispersion $E_n[k_x]$ reads:

$$E_n[k_x] = E_n^{\mathrm{bulk}} + \frac{\hbar^2}{2m^*}\Theta[\sigma_n - Y]\left(\frac{\sigma_n}{l_B^2} - k_x\right)^2, \tag{6.2.1}$$

where $\Theta[x]$ is the Heaviside function. The condition for resonant tunneling is obtained by equating the LL spectrum at the Fermi energy with the lower wire dispersion $\epsilon_{k_x}^{(l)}$, shifted in k_x-direction to account for the momentum kick $eB_y d$ (tunneling to the lower system in presence of B_y) and $eB_z\Delta y_i$ (displacement Δy_i of the $\mathrm{LW_i}$ wave function CM with respect to the cleaved edge):

$$\epsilon_{k_x}^{(l)} = \frac{\left(\hbar k_x - eB_y d - eB_z\Delta y_i\right)^2}{2m^*} + \epsilon_0^{(l)}. \tag{6.2.2}$$

Here, $\epsilon_0^{(l)}$ is an energy offset that accounts for the difference in band edges of 2DEG and respective lower wire mode with respect to the common Fermi energy. Combining Eqns (6.2.1), (6.2.2) we obtain the evolution of the tunneling resonances as a function of B_y and B_z,

$$\frac{eB_y d}{\hbar} = \sqrt{\frac{2n+1}{l_B^2}} - \sqrt{k_{\mathrm{F,2D}}^2 - \frac{2n+1}{l_B^2}} + \gamma_i - \frac{\Delta y_i}{l_B^2} \tag{6.2.3}$$

where $\gamma_i = \sqrt{k_{\mathrm{F,2D}}^2 - 2m^*\epsilon_0^{(l)}/\hbar^2}$ is a quantum wire mode dependent overall momentum shift.

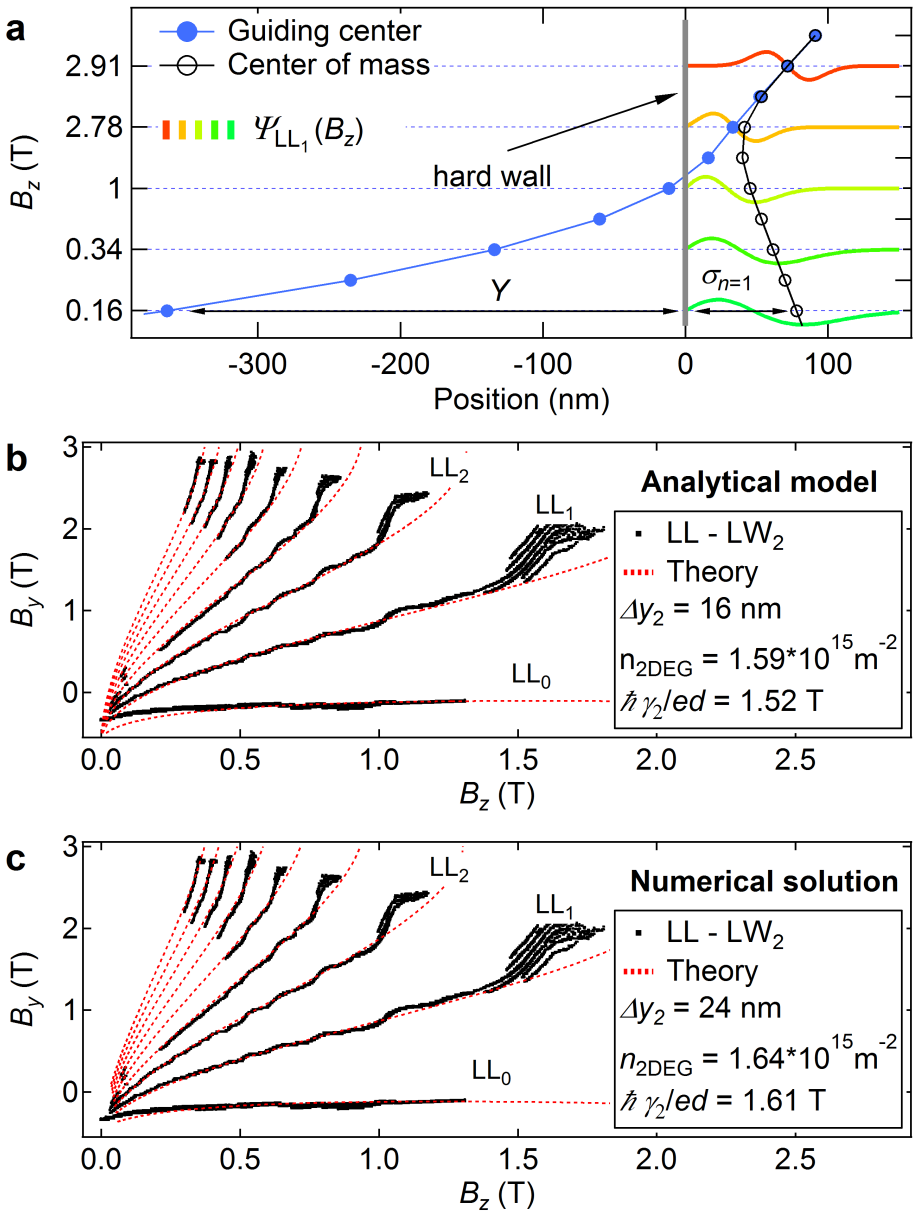

Figure 6.4: **Comparison of experiment and theory. a,** Landau Level wave functions for particular values of B_z chosen to visualize the important stages of magnetic field evolution. Note that the resulting vertical scale is highly nonlinear. The wave functions are obtained from a numerical Schrödinger solver, showing magnetic compression of the wave function and subsequent depopulation. The hard wall confinement completely separates wave function CM and GC position, the latter residing outside the physical sample for most of the B-field range. Hybridization of LLs and UW_1 would result in an additional node for LL wave functions at the Fermi energy. In **b,c** experimental data are compared to theoretical predictions from an analytical model and to numerical solutions from a single-particle Schrödinger solver, respectively.

6.3 Discussion

Both the numerical and the analytical models capture the experimental tunneling resonances very well and result in very similar fitting parameters, shown in Fig. 6.4b,c for LL tunneling to LW_2 (black data from Fig.6.3). We note that equally good fits are obtained for tunneling to other lower wire modes as well, using the same 2DEG density $n_{2\mathrm{DEG}} = k_{\mathrm{F,2D}}^2/2\pi$ and increasing quantum wire displacement Δy_i for higher modes (see Supplementary Fig. 5), as expected – thus lending further support to the models. We emphasize that both models consistently deliver the CM positions, with similar nanometer precision as the GC positions extracted directly from the spectroscopy. This makes it possible to plot a full map of the magnetic field evolution of the edge states, see Fig.6.4a. Throughout the process of increasing magnetic field Bz, the electron wave function is progressively compressed (from green to red curves). There are two stages of the edge state motion as magnetic field Bz increases: first, motion of the center of mass towards the hard wall (empty circles for $B_z < 2.78\,\mathrm{T}$) and motion away from the hard wall at larger fields, see also Supplementary Fig.3. During the latter stage, the center of mass merges with the guiding center position (black and blue curves approach and then coincide for larger B_z in Fig.6.4a), followed by depopulation of the corresponding LL.

Despite the good match between experiment and non-interacting single-particle theory, there remain minor discrepancies. In particular the shoulder structures at the transitions between integer bulk filling factors (Fig. 6.3d), and the spin splitting observed at large in-plane magnetic field (Fig. 6.3e) are not captured by the model. Furthermore, at the transition to magnetic depopulation, individual resonances are observed to branch out, clearly visible for e.g. the LL_1-LW_2 transition in Fig. 6.3f. Splitting of single resonances could arise e.g. from edge reconstruction or may also result from the formation of stripe or bubble phases.

In summary, we employed momentum-resolved tunneling spectroscopy to image the evolution for the lowest ≈ 10 integer quantum Hall edge states of a GaAs 2DEG with nanometer

resolution, and down to magnetic fields of $B_z \gtrsim 10\,\mathrm{mT}$ ($\nu_{\mathrm{bulk}} \approx 500$). We directly observe the chiral nature of integer quantum Hall edge states, as well as magnetic depopulation at the respective bulk filling factor. In addition, spin splitting is observed at the transition to depopulation. Theoretical predictions assuming the topologically gapped bulk spectrum and hard wall confinement reproduce very well the experimental data over the entire range of magnetic field, thus confirming the bulk to edge correspondence.

In the future, also fractional quantum Hall edge state can be investigated with the spectroscopy technique presented here. The present sample exhibits clearly visible $\nu = 4/3$ and $\nu = 5/3$ fractional states in conventional transport measurements. Imaging the fractional states by means of this highly sensitive momentum-resolved tunnel spectroscopy would be of great interest and can be addressed in future experiments. Fractional states are stabilized by electron-electron interactions and are thus believed to exist only in the vicinity of the respective filling factor, in contrast to integer edge states that persist at all fields up to their magnetic depopulation. Because of power law exponents determining the tunneling conductance from the fractional quantum Hall edge states [212–216], a pronounced DC bias voltage dependence is expected for these states. This also makes it very interesting to explore another experimental knob, bias voltage, which controls the energy transfer during the tunneling event.

Beyond fractional states, the technique described here can also be applied to other topological insulator materials. In those systems where a wire exhibiting tunneling can be integrated or placed in parallel, edge states, both 1D or 2D in nature, can also be studied with this method with unprecedented resolution in a weakly invasive way. We note that ultra clean wires, such as used here to probe the edge states, are not necessary, in fact, thus opening the door to studying a variety of topological materials and their exotic edge states with this new tunneling spectroscopy.

acknowledgments

We thank Carlos Egues, Bertrand Halperin, Daniel Loss, and Jelena Klinovaya for very

helpful discussions and we thank M. Steinacher and S. Martin and their teams for technical assistance. This work was supported by the Swiss Nanoscience Institute (SNI), NCCR QSIT, Swiss NSF, and the European Microkelvin Platform (EMP). A. Y. was supported by the NSF Grant No. DMR-1708688. The work at Princeton University was funded by the Gordon and Betty Moore Foundation through the EPiQS initiative Grant GBMF4420, and by the National Science Foundation MRSEC Grant DMR 1420541.

Author Contributions

T.P., C.P.S, D.M.Z conceived the experiment, analyzed the data and wrote the manuscript. T.P. and C.P.S. performed the experiments and numerical calculations. D.H. and Y.T. developed and carried out the theoretical work. G.B., A.Y., L.N.P., K.W.W. designed and fabricated the sample. All authors discussed the results and commented on the manuscript.

Competing interests

The authors declare no competing interests.

6.4 Methods

Device layout

The device used for this study is produced by means of the cleaved edge overgrowth method. It consists of a lower, 30 nm wide GaAs quantum well, separated by a 6 nm thick AlGaAs tunnel barrier from the upper, 20 nm thick GaAs quantum well [193]. A silicon doping layer above the upper quantum well provides free charge carriers, resulting in the formation of a 2DEG in the upper quantum well while the lower well remains unpopulated. The sample with prefabricated tungsten top gate is then cleaved inside the growth chamber and immediately overgrown on the sample edge (including a Si doping layer). Due to the additional side dopants, charge carriers are attracted to the sample edge, thereby forming strongly confined 1D channels (in upper and lower quantum well) along the entire cleaved edge. The 1D channels support a few (5 or less) transverse modes with sub-band spacing up

to 20 meV and mean free path exceeding 10 μm [179]. Ohmic indium solder contacts to the 2DEG allow for transport studies. While the upper 1D system is well coupled to the 2DEG, the lower 1D channels are only weakly tunnel coupled, thus allowing for tunnel spectroscopy measurements.

Measurements setup

Tunneling spectroscopy measurements are recorded with standard low frequency (5-10 Hz) lock-in technique with typically 6 μV AC excitation. All measurements are done at effectively zero DC bias using a specially designed low noise current preamplifier with active drift compensation (Basel Electronics Lab) ensuring $V_{DC} \lesssim 5\,\mu V$.

Significant efforts were taken in order to obtain low electronic temperatures [217–223]. The present device is mounted on a home-built silver epoxy sample holder inside a heavily filtered dilution refrigerator with 5 mK base temperature. Roughly 1.5 m of thermocoax wire is used in combination with two stages of home-built silver epoxy microwave filters [219] to efficiently filter and thermalize each measurement lead, resulting in electronic sample temperatures around 10 mK.

Numerical solution

Numerical solutions are obtained by solving the 1D Schrödinger equation using Numerov's method. The hard wall confinement forces the electronic wave functions to be zero at that boundary. The perpendicular magnetic field gives an additional parabolic confinement. Its minimum is shifted away from the hard wall by the GC position Y. The energy of a given solution is then changed iteratively until a vanishing wave function at the hard wall is obtained.

Data acquisition

A vector magnet (8 T solenoid and 4 T split-pair) is used to provide the external magnetic field for spectroscopy measurements. Exceptional device stability is required in order

to perform those extremely time consuming B-field vs B-field maps in the main article. In particular, Fig 6.3a is composed of 3 individual data sets with a total measurement time of roughly 6 weeks. In order to reduce the measurement time, here the magnetic field B_z was scanned in a zig-zag fashion, i.e. taking data during ramping up and ramping down of B_z. However, due to the finite inductance of the magnet, a hysteretic behavior of the applied B-field results, which was accounted for by performing a non-linear correction to the measured data. The empty white spaces in Fig 6.3a (round corners) are due to the accessible combined field range of the vector magnet. A slight sample misalignment with respect to the $y-$ and $z-$direction is accounted for by tilting the experimental data in Figs. 6.2-6.4

The data of all the Figures of the main manuscript and the relevant code are available on a Zenodo repository (https://doi.org/10.5281/zenodo.1251622).

Chapter 7

Outlook

We have seen in Chapters 1 through 3 how the Landau-Liifshitz-Gilbert equation can be used to study the non-equilibrium phases of a ferromagnet. In Chapter 2 we explored the static phase diagram in the presence of weak in-plane anisotropy, as well as the analogy to the long Josephson junction, and in Chapter 3 we studied the easy-plane ferromagnet in the presence of strong edge torques and illustrated the robustness of the spin superfluid. The results for the edge torque on one side are summarized in the schematic phase diagram of Figure 7.1.

In Chapters 4 and 6 we considered microscopic descriptions of some examples magnetic systems, including fermionizable weakly coupled series of spin chains and a cleved edge overgrowth 2DEG in the presence of an external magnetic field. In the former we illustrated the possibility of forming superconducting and quantum Hall-like phases with spin degrees of freedom, and in the latter we modeled tunneling and discovered a spin splitting of dissipationless edge currents in the presence of a strong in-plane magnetic field. Lastly, in Chapter 5 we studied the sound wave scattering with magnetic domain walls on a wire and proposed potential spintronic applications.

There are many possible future directions for building off of the above mentioned work. The anisotropic ferromagnet of Chapter 2 has potential for use as a spintronic logic gate

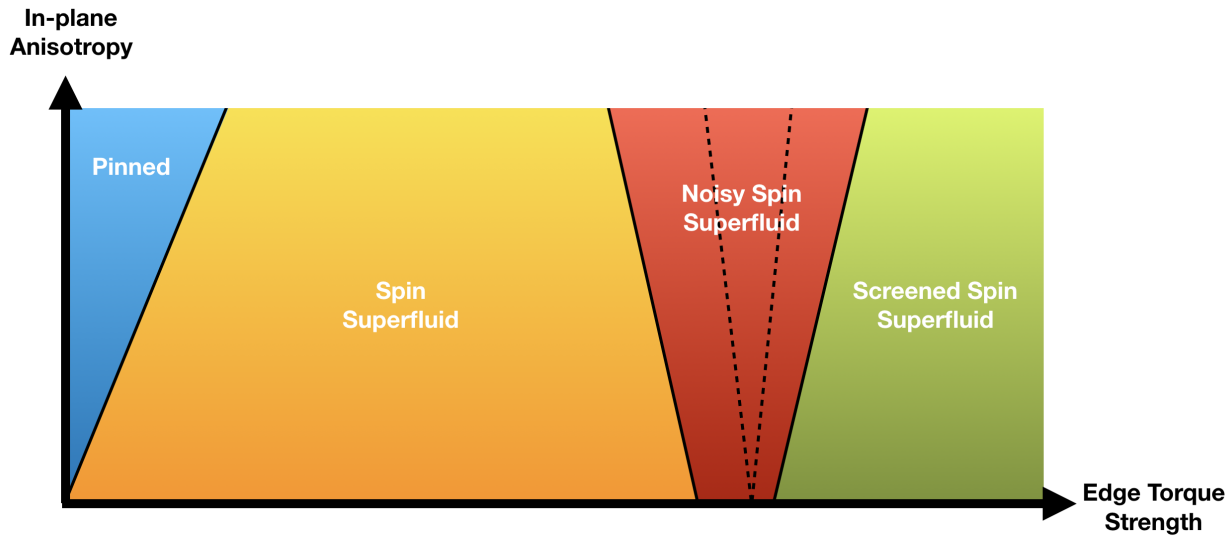

Figure 7.1: Schematic non-equilibrium phase diagram of the easy-plane ferromaget with a driving torque on one edge in the presence of weak in-plane anisotropy.

and neuromorphic computing component (see Figure 7.2). For example, in the static steady state phases, the anisotropic ferromagnet can act as a multibit register, which would exploit domain wall non-equilibrium phase hysterisis as a memory storage mechanism. In addition, at the threshold for dynamic phases, the anisotropic ferromagnet may be able to act as a sort of neuron, with traveling domain walls acting analogously to the discrete bursts of electrical signals in a synapse.

For the high bias regime of the ferromagnet discussed in chapter 3, future work could focus on the internal phase structure and spectral decomposition of the noisy spin superfluid in the intermediate bias regime of Figure 7.1. In addition, similar methods for studying magnetic non-equilibrium phases could be extended to other types of systems, such as antiferromagnets and correlated spin glassess.

For the fermionizable spin chains of Chapter 4, numerical modeling and renormalization group approaches would be useful in more exaustively characterizing the phases of these systems. And lastly, for the Quantum Hall system of Chapter 6, future work could focus on looking for edge state signatures of fractional quantum Hall effects. Such effects may be detectible in the form of nontrivial voltage or temperature dependence of the tunneling

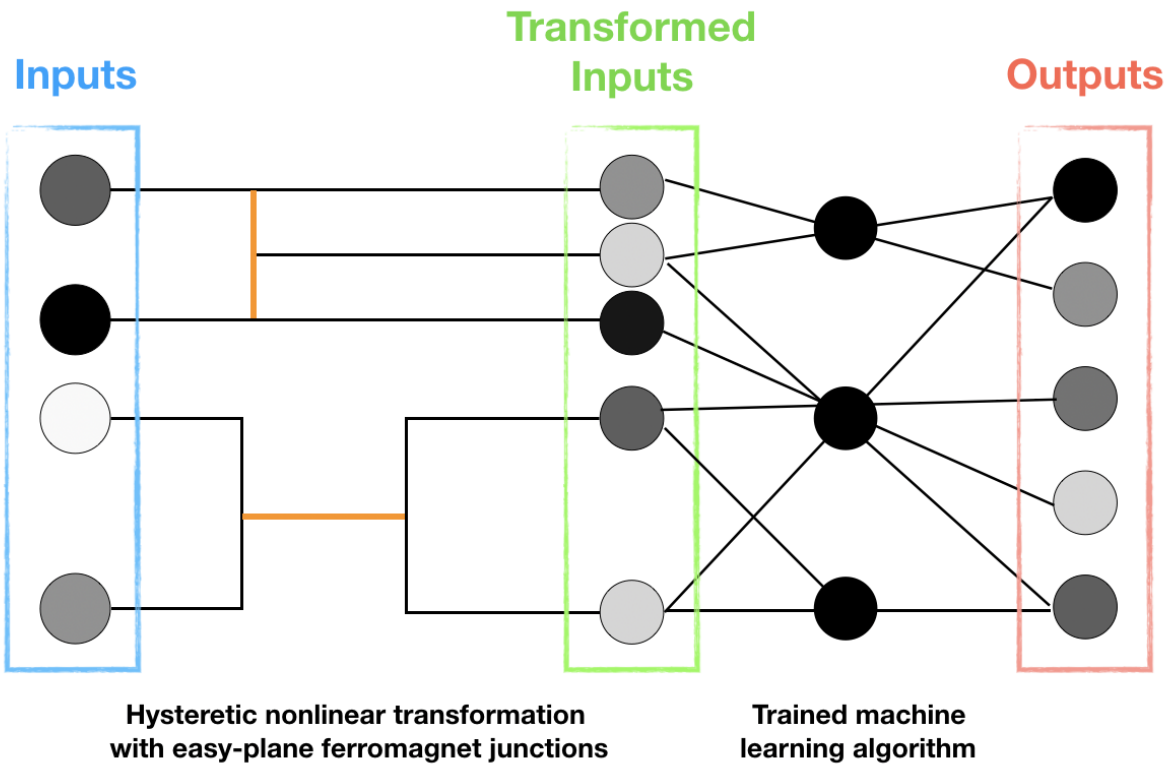

Figure 7.2: A simplified schematic diagram of a potential spintronics-based neuromorphic computer, which would transform imputs with a anisotropic ferromagnet base neural network and then extract usable data using a traditional machine learning algorithm.

amplitudes.

Bibliography

[1] S. K. Kim, D. Hill, and Y. Tserkovnyak, "Mechanical Actuation of Magnetic Domain-Wall Motion," *Phys. Rev. Lett.* **117** (Nov, 2016) 237201.

[2] D. Hill, S. K. Kim, and Y. Tserkovnyak, "Spin analogs of superconductivity and integer quantum Hall effect in an array of spin chains," *Phys. Rev. B* **95** (May, 2017) 180405.

[3] D. Hill, S. K. Kim, and Y. Tserkovnyak, "Spin-Torque-Biased Magnetic Strip: Nonequilibrium Phase Diagram and Relation to Long Josephson Junctions," *Phys. Rev. Lett.* **121** (Jul, 2018) 037202.

[4] T. Patlatiuk, C. P. Scheller, D. Hill, Y. Tserkovnyak, G. Barak, A. Yacoby, L. N. Pfeiffer, K. W. West, and D. M. Zumbühl, "Evolution of the quantum Hall bulk spectrum into chiral edge states," *Nat. Comm.* **9** (2018) 3692.

[5] T. Schneider, D. Hill, A. Kakay, K. Lenz, J. Lindner, J. Fassbender, P. Upadhyaya, Y. Liu, K. Wang, Y. Tserkovnyak, I. N. Krivorotov, and I. Barsukov, "Self-stabilizing spin superfluid," `arXiv:1811.09369`.

[6] M. Lakshmanan, "The fascinating world of the Landau-Lifshitz-Gilbert equation: an overview," *Philos. Trans. Royal Soc. A* **369** (2011).

[7] L. D. Landau and E. M. Lifshitz, "Theory of the dispersion of magnetic permeability in ferromagnetic bodies," *Phys. Z. Sowjetunion.* **8** (1935) 153.

[8] T. L. Gilbert, "A Lagrangian formulation of the gyromagnetic equation of the magnetic field," *Phys. Rev.* **100** (1955) 1243.

[9] T. Moriya, "New Mechanism of Anisotropic Superexchange Interaction," *Phys. Rev. Lett.* **4** (Mar, 1960) 228.

[10] M. J. Groenewold, "On the Principles of Elementary Quantum Mechanics," *Physica* **12** (1946) 405.

[11] K. Gilmore, Y. U. Idzerda, and M. D. Stiles, "Identification of the Dominant Precession-Damping Mechanism in Fe, Co, and Ni by First-Principles Calculations," *Phys. Rev. Lett.* **99** (Jul, 2007) 027204.

[12] T. L. Gilbert, "A phenomenological theory of damping in ferromagnetic materials," *IEEE Transactions on Magnetics* **40** (Nov, 2004) 3443–3449.

[13] J. Slonczewski, "Current-driven excitation of magnetic multilayers," *J. Magn. Magn. Mater.* **159** (1996), no. 1 L1 – L7.

[14] S. A. Wolf, D. D. Awschalom, R. A. Buhrman, J. M. Daughton, S. von Molnár, M. L. Roukes, A. Y. Chtchelkanova, and D. M. Treger, "Spintronics: A Spin-Based Electronics Vision for the Future," *Science* **294** (2001), no. 5546 1488–1495.

[15] S. Takei and Y. Tserkovnyak, "Superfluid Spin Transport Through Easy-Plane Ferromagnetic Insulators," *Phys. Rev. Lett.* **112** (jun, 2014) 227201.

[16] E. Locane and P. W. Brouwer, "Current-induced switching of magnetic molecules on topological insulator surfaces," *Phys. Rev. B* **95** (Mar, 2017) 125437.

[17] Y. Tserkovnyak and H. Ochoa, "Generalized boundary conditions for spin transfer," *Phys. Rev. B* **96** (Sep, 2017) 100402.

[18] E. Sonin, "Spin currents and spin superfluidity," *Adv. Phys.* **59** (2010), no. 3 181–255.

[19] Y. Tserkovnyak, "Perspective: (Beyond) spin transport in insulators," *Journal of Applied Physics* **124** (2018), no. 19 190901.

[20] Y. Tserkovnyak and M. Kläui, "Exploiting Coherence in Nonlinear Spin-Superfluid Transport," *Phys. Rev. Lett.* **119** (Nov, 2017) 187705.

[21] S. K. Ivanov, A. M. Kamchatnov, T. Congy, and N. Pavloff, "Solution of the Riemann problem for polarization waves in a two-component Bose-Einstein condensate," *Phys. Rev. E* **96** (Dec, 2017) 062202.

[22] S. Moulder, S. Beattie, R. P. Smith, N. Tammuz, and Z. Hadzibabic, "Quantized supercurrent decay in an annular Bose-Einstein condensate," *Phys. Rev. A* **86** (Jul, 2012) 013629.

[23] H. Chang, P. Li, W. Zhang, T. Liu, A. Hoffmann, L. Deng, and M. Wu, "Nanometer-Thick Yttrium Iron Garnet Films With Extremely Low Damping," *IEEE Magnetics Letters* **5** (2014) 1–4.

[24] E. B. Sonin, "Analogs of superfluid currents for spins and electron-hole pairs," *J. Exp. Theor. Phys.* **47** (1978), no. 6 1091–1099.

[25] J. König, M. C. Bønsager, and A. H. MacDonald, "Dissipationless Spin Transport in Thin Film Ferromagnets," *Phys. Rev. Lett.* **87** (Oct, 2001) 187202.

[26] S. Takei and Y. Tserkovnyak, "Nonlocal Magnetoresistance Mediated by Spin Superfluidity," *Phys. Rev. Lett.* **115** (Oct, 2015) 156604.

[27] W. Yuan, Q. Zhu, T. Su, Y. Yao, W. Xing, Y. Chen, Y. Ma, X. Lin, J. Shi, R. Shindou, X. C. Xie, and W. Han, "Experimental signatures of spin superfluid ground state in canted antiferromagnet Cr2O3 via nonlocal spin transport," *Sci. Adv.* **4** (2018).

[28] P. Stepanov, S. Che, D. Shcherbakov, J. Yang, K. Thilahar, G. Voigt, M. W. Bockrath, D. Smirnov, K. Watanabe, T. Taniguchi, R. K. Lake, Y. Barlas, A. H. MacDonald, and C. N. Lau, "Long-distance spin transport through a graphene quantum hall antiferromagnet.".

[29] C. S. Owen and D. J. Scalapino, "Vortex Structure and Critical Currents in Josephson Junctions," *Phys. Rev.* **164** (Dec, 1967) 538–544.

[30] S. V. Kuplevakhsky and A. M. Glukhov, "Exact analytical solution of the problem of current-carrying states of the Josephson junction in external magnetic fields," *Phys. Rev. B.* **76** (2007) 174515.

[31] S. V. Kuplevakhsky and A. M. Glukhov, "Static solitons of the sine-Gordon equation and equilibrium vortex structure in Josephson junctions," *Phys. Rev. B.* **73** (2006) 024513.

[32] M. Jaworski, "Flux-flow dynamics in a long Josephson junction with nonuniform bias current," *Supercond. Sci. Technol.* **21** (2008) 065016.

[33] Y. Tserkovnyak, A. Brataas, and G. E. W. Bauer, "Enhanced Gilbert Damping in Thin Ferromagnetic Films," *Phys. Rev. Lett.* **88** (2002), no. 11 117601.

[34] J. Sinova, S. O. Valenzuela, J. Wunderlich, C. H. Back, and T. Jungwirth, "Spin Hall effects," *Rev. Mod. Phys.* **87** (Oct, 2015) 1213–1260.

[35] B. I. Halperin and P. C. Hohenberg, "Hydrodynamic Theory of Spin Waves," *Phys. Rev.* **188** (Dec, 1969) 898–918.

[36] T. L. Gilbert, "A Phenomenological Theory of Damping in Ferromagnetic Materials," *IEEE Trans. Magn.* **40** (2004), no. 6 3443–3449.

[37] S. K. Kim, S. Takei, and Y. Tserkovnyak, "Thermally activated phase slips in superfluid spin transport in magnetic wires," *Phys. Rev. B* **93** (Jan, 2016) 020402(R).

[38] Y. Tserkovnyak and S. A. Bender, "Spin Hall phenomenology of magnetic dynamics," *Phys. Rev. B* **90** (Jul, 2014) 014428.

[39] J. Cuevas-Maraver, P. Kevrekidis, and F. Williams, eds., *The sine-Gordon Model and its Applications*, vol. 10 of *Nonlinear Systems and Complexity*. Springer, Cham, 2014.

[40] R. Gross, A. Marx, and F. Deppe, *Applied Superconductivity: Josephson Effect and Superconducting Electronics*. de Gruyter Textbook. Walter De Gruyter Incorporated, 2016.

[41] R. Parmentier, "Solitons and Long Josephson Junctions," in *The New Superconducting Electronics. NATO ASI Series* (H. Weinstock and R. Ralston, eds.), vol. 251, ch. 7, pp. 221–248. Springer, Van Godewijckstraat 30, 3311 GX Dordrecht, Netherlands, 1993.

[42] E. Iacocca, T. J. Silva, and M. A. Hoefer, "Symmetry-broken dissipative exchange flows in thin-film ferromagnets with in-plane anisotropy," *Phys. Rev. B* **96** (Oct, 2017) 134434.

[43] Y. Kajiwara, K. Harii, S. Takahashi, J. Ohe, K. Uchida, M. Mizuguchi, H. Umezawa, H. Kawai, K. Ando, K. Takanashi, S. Maekawa, and E. Saitoh, "Transmission of electrical signals by spin-wave interconversion in a magnetic insulator," *Nature* **464** (03, 2010) 262–266.

[44] H. Chen, A. D. Kent, A. H. MacDonald, and I. Sodemann, "Nonlocal transport mediated by spin supercurrents," *Phys. Rev. B* **90** (dec, 2014) 220401(R).

[45] G. P. Pepe, R. Scaldaferri, L. Parlato, G. Peluso, C. Granata, M. Russo, G. Rotoli, and N. E. Booth, "Low- T c three-terminal structures for new superconducting devices," *Supercond. Sci. Technol.* **14** (2001), no. 12 987.

[46] C. Guarcello, P. Solinas, M. Di Ventra, and F. Giazotto, "Solitonic Josephson-based meminductive systems," *Sci. Rep.* **7** (2016).

[47] G. S. D. Beach, C. Nistor, C. Knutson, M. Tsoi, and J. L. Erskine, "Dynamics of field-driven domain-wall propagation in ferromagnetic nanowires," *Nature Materials* **4** (Sept, 2005) 741.

[48] S. S. P. Parkin, M. Hayashi, and L. Thomas, "Magnetic Domain-Wall Racetrack Memory," *Science* **320** (2008), no. 5873 190–194.

[49] I. M. Miron, K. Garello, G. Gaudin, P.-J. Zermatten, M. V. Costache, S. Auffret, S. Bandiera, B. Rodmacq, A. Schuhl, and P. Gambardella, "Perpendicular switching of a single ferromagnetic layer induced by in-plane current injection," *Nature* **476** (2011) 189–193.

[50] A. V. Chumak, V. I. Vasyuchka, A. A. Serga, and B. Hillebrands, "Magnon spintronics," *Nat. Phys.* **11** (06, 2015) 453–461.

[51] A. Oosawa, M. Ishii, and H. Tanaka, "Field-induced three-dimensional magnetic ordering in the spin-gap system," *J. Phys. Condens. Matter* **11** (jan, 1999) 265–271.

[52] T. Nikuni, M. Oshikawa, A. Oosawa, and H. Tanaka, "Bose-Einstein Condensation of Dilute Magnons in TlCuCl3," *Phys. Rev. Lett.* **84** (jun, 2000) 5868–5871.

[53] T. Radu, H. Wilhelm, V. Yushankhai, D. Kovrizhin, R. Coldea, Z. Tylczynski, T. Luhmann, and F. Steglich, "Bose-Einstein Condensation of Magnons in Cs2CuCl4," *Phys. Rev. Lett.* **95** (sep, 2005) 127202.

[54] S. O. Demokritov, V. E. Demidov, O. Dzyapko, G. A. Melkov, A. A. Serga, B. Hillebrands, and A. N. Slavin, "Bose-Einstein condensation of quasi-equilibrium magnons at room temperature under pumping," *Nature* **443** (sep, 2006) 430–433.

[55] D. A. Bozhko, A. A. Serga, P. Clausen, V. I. Vasyuchka, F. Heussner, G. A. Melkov, A. Pomyalov, V. S. Lvov, and B. Hillebrands, "Supercurrent in a room-temperature Bose-Einstein magnon condensate," *Nat. Phys.* **12** (2016), no. 11 1057–1062.

[56] J. Bardeen, L. N. Cooper, and J. R. Schrieffer, "Microscopic Theory of Superconductivity," *Phys. Rev.* **106** (1957), no. 1 162–164.

[57] A. S. Borovik-Romanov, Y. M. Bun'kov, V. V. Dmitriev, and Y. M. Mukharskii, "Long-lived induction signal in superfluid ^{3}He-B," *Sov. Phys. JETP* **40** (1984) 1033.

[58] K.-H. Bennemann and J. B. Ketterson, eds., *Novel Superfluids*. Oxford University Press, nov, 2014.

[59] B. I. Halperin and P. C. Hohenberg, "Hydrodynamic Theory of Spin Waves," *Phys. Rev.* **188** (dec, 1969) 898–918.

[60] E. Sonin, "Spin currents and spin superfluidity," *Adv. Phys.* **59** (2010), no. 3 181–255.

[61] C. Scheck, L. Cheng, I. Barsukov, Z. Frait, and W. Bailey, "Low relaxation rate in epitaxial vanadium-doped ultrathin iron films," *Phys. Rev. Lett.* **98** (2007) 117601.

[62] I. Barsukov, S. Mankovsky, A. Rubacheva, R. Meckenstock, D. Spoddig, J. Lindner, N. Melnichak, B. Krumme, S. Makarov, H. Wende, H. Ebert, and M. Farle, "Magnetocrystalline anisotropy and Gilbert damping in iron-rich Fe1?xSix thin films," *Phys. Rev. B* **84** (2011) 180405(R).

[63] M. Schoen, D. Thonig, M. Schneider, T. Silva, H. Nembach, O. Eriksson, O. Karis, and J. Shaw, "Ultra-low magnetic damping of a metallic ferromagnet," *Nat. Phys.* **12** (2016) 839.

[64] H. Chang, P. Li, W. Zhang, T. Liu, A. Hoffmann, L. Deng, and M. Wu, "Nanometer-Thick Yttrium Iron Garnet Films With Extremely Low Damping," *IEEE Magn. Lett.* **5** (2014) 6700104.

[65] P. Stepanov, S. Che, D. Shcherbakov, J. Yang, R. Chen, K. Thilahar, G. Voigt, M. W. Bockrath, D. Smirnov, K. Watanabe, T. Taniguchi, R. K. Lake, Y. Barlas, A. H. MacDonald, and C. N. Lau, "Long-distance spin transport through a graphene quantum Hall antiferromagnet," *Nat. Phys.* **14** (2018) 907.

[66] W. Yuan, Q. Zhu, T. Su, Y. Yao, W. Xing, Y. Chen, Y. Ma, X. Lin, J. Shi, R. Shindou, X. C. Xie, and W. Han, "Experimental signatures of spin superfluid ground state in canted antiferromagnet Cr2O3 via nonlocal spin transport," *Sci. Adv.* **4** (apr, 2018) eaat1098.

[67] J. König, M. C. Bønsager, and A. H. MacDonald, "Dissipationless Spin Transport in Thin Film Ferromagnets," *Phys. Rev. Lett.* **87** (oct, 2001) 187202.

[68] B. Flebus, S. A. Bender, Y. Tserkovnyak, and R. A. Duine, "Two-Fluid Theory for Spin Superfluidity in Magnetic Insulators," *Phys. Rev. Lett.* **116** (mar, 2016) 117201.

[69] E. Iacocca, T. J. Silva, and M. A. Hoefer, "Breaking of Galilean Invariance in the Hydrodynamic Formulation of Ferromagnetic Thin Films," *Phys. Rev. Lett.* **118** (jan, 2017) 017203.

[70] E. Iacocca, T. J. Silva, and M. A. Hoefer, "Symmetry-broken dissipative exchange flows in thin-film ferromagnets with in-plane anisotropy," *Phys. Rev. B* **96** (oct, 2017) 134434.

[71] Y. Tserkovnyak and M. Kläui, "Exploiting Coherence in Nonlinear Spin-Superfluid Transport," *Phys. Rev. Lett.* **119** (nov, 2017) 187705.

[72] D. Hill, S. K. Kim, and Y. Tserkovnyak, "Spin-Torque-Biased Magnetic Strip: Nonequilibrium Phase Diagram and Relation to Long Josephson Junctions," *Phys. Rev. Lett.* **121** (jul, 2018) 037202.

[73] H. Chen and A. H. MacDonald, "Spin-Superfluidity and Spin-Current Mediated Non-Local Transport," *arXiv* (2016) 1604.02429.

[74] E. Sonin, "Superfluid spin transport in ferro- and antiferromagnets," *arXiv* (2018) 1810.07020.

[75] H. Skarsvåg, C. Holmqvist, and A. Brataas, "Spin Superfluidity and Long-Range Transport in Thin-Film Ferromagnets," *Phys. Rev. Lett.* **115** (dec, 2015) 237201.

[76] V. P. Kravchuk, D. D. Sheka, A. Kakay, O. M. Volkov, U. K. Rossler, J. van den Brink, D. Makarov, and Y. Gaididei, "Multiplet of Skyrmion States on a Curvilinear Defect: Reconfigurable Skyrmion Lattices," *Phys. Rev. Lett.* **120** (feb, 2018) 067201.

[77] P. Upadhyaya, S. K. Kim, and Y. Tserkovnyak, "Magnetic Domain Wall Floating on a Spin Superfluid," *Phys. Rev. Lett.* **118** (feb, 2017) 097201.

[78] Y. Tserkovnyak, A. Brataas, and G. E. W. Bauer, "Enhanced Gilbert Damping in Thin Ferromagnetic Films," *Phys. Rev. Lett.* **88** (Feb, 2002) 117601.

[79] V. E. Zakharov, V. S. Lvov, and S. S. Starobinets, "Spin-wave turbulence beyond the parametric excitation threshold," *Sov. Phys. Usp.* **17** (jun, 1975) 896–919.

[80] D. Hill, S. K. Kim, and Y. Tserkovnyak, "Easy-Plane Magnetic Strip as a Long Josephson Junction," *Phys. Rev. Lett.* **121** (2018) 037202.

[81] A. Humphries, T. Wang, E. Edwards, S. Allen, J. Shaw, H. Nembach, J. Xiao, T. Silva, and X. Fan, "Observation of spin-orbit effects with spin rotation symmetry," *Nat. Commun.* **8** (2017) 911.

[82] C. Safranski, E. Montoya, and I. Krivorotov, "Spin?orbit torque driven by a planar Hall current," *Nat. Nanotech.* **14** (2019) 27.

[83] T. Taniguchi, J. Grollier, and M. Stiles, "Spin-transfer torques generated by the anomalous Hall effect and anisotropic magnetoresistance," *Phys. Rev. Appl.* **3** (2015) 044001.

[84] C. Safranski, I. Barsukov, H. Lee, T. Schneider, A. Jara, A. Smith, H. Chang, K. Lenz, J. Lindner, Y. Tserkovnyak, M. Wu, and I. Krivorotov, "Spin caloritronic nano-oscillator," *Nat. Commun.* **8** (2017) 117.

[85] A. Vansteenkiste, J. Leliaert, M. Dvornik, M. Helsen, F. Garcia-Sanchez, and B. V. Waeyenberge, "The design and verification of MuMax3," *AIP Advances* **4** (oct, 2014) 107133.

[86] W. Wang, C. Mu, B. Zhang, Q. Liu, J. Wang, and D. Xue, "Two-dimensional periodic boundary conditions for demagnetization interactions in micromagnetics," *Comput. Mater. Sci.* **49** (jun, 2010) 84–87.

[87] I. H. Solt, "Temperature Dependence of YIG Magnetization," *J. Appl. Phys.* **33** (mar, 1962) 1189–1191.

[88] S. Klingler, A. V. Chumak, T. Mewes, B. Khodadadi, C. Mewes, C. Dubs, O. Surzhenko, B. Hillebrands, and A. Conca, "Measurements of the exchange stiffness of YIG films using broadband ferromagnetic resonance techniques," *J. Phys. D: Appl. Phys.* **48** (dec, 2014) 015001.

[89] C. Dubs, O. Surzhenko, R. Linke, A. Danilewsky, U. Bruckner, and J. Dellith, "Sub-micrometer yttrium iron garnet LPE films with low ferromagnetic resonance losses," *J. Phys. D: Appl. Phys.* **50** (apr, 2017) 204005.

[90] M. Tinkham, *Introduction to Superconductivity.* Dover, New York, 2004.

[91] J. Bardeen, L. N. Cooper, and J. R. Schrieffer, "Theory of Superconductivity," *Phys. Rev.* **108** (Dec, 1957) 1175–1204.

[92] R. Prange and S. Girvin, *The Quantum Hall Effect*. Springer Science and Business Media, 1990.

[93] K. v. Klitzing, G. Dorda, and M. Pepper, "New Method for High-Accuracy Determination of the Fine-Structure Constant Based on Quantized Hall Resistance," *Phys. Rev. Lett.* **45** (Aug, 1980) 494–497.

[94] S. A. Wolf, D. D. Awschalom, R. A. Buhrman, J. M. Daughton, S. von Molnár, M. L. Roukes, A. Y. Chtchelkanova, and D. M. Treger, "Spintronics: A Spin-Based Electronics Vision for the Future," *Science* **294** (2001), no. 5546 1488–1495.

[95] I. Zutic, J. Fabian, and S. Das Sarma, "Spintronics: Fundamentals and applications," *Rev. Mod. Phys.* **76** (Apr, 2004) 323–410.

[96] W. Chen and M. Sigrist, "Spin superfluidity in coplanar multiferroics," *Phys. Rev. B* **89** (Jan, 2014) 024511.

[97] S. Takei, B. I. Halperin, A. Yacoby, and Y. Tserkovnyak, "Superfluid spin transport through antiferromagnetic insulators," *Phys. Rev. B* **90** (Sep, 2014) 094408.

[98] W. Chen and M. Sigrist, "Dissipationless Multiferroic Magnonics," *Phys. Rev. Lett.* **114** (Apr, 2015) 157203.

[99] V. Kalmeyer and R. B. Laughlin, "Equivalence of the resonating-valence-bond and fractional quantum Hall states," *Phys. Rev. Lett.* **59** (Nov, 1987) 2095–2098.

[100] V. Kalmeyer and R. B. Laughlin, "Theory of the spin liquid state of the Heisenberg antiferromagnet," *Phys. Rev. B* **39** (Jun, 1989) 11879–11899.

[101] X. G. Wen, F. Wilczek, and A. Zee, "Chiral spin states and superconductivity," *Phys. Rev. B* **39** (Jun, 1989) 11413–11423.

[102] T. Meng, T. Neupert, M. Greiter, and R. Thomale, "Coupled-wire construction of chiral spin liquids," *Phys. Rev. B* **91** (Jun, 2015) 241106.

[103] F. D. M. Haldane and D. P. Arovas, "Quantized spin currents in two-dimensional chiral magnets," *Phys. Rev. B* **52** (Aug, 1995) 4223–4225.

[104] R. Matsumoto and S. Murakami, "Theoretical Prediction of a Rotating Magnon Wave Packet in Ferromagnets," *Phys. Rev. Lett.* **106** (May, 2011) 197202.

[105] R. Matsumoto and S. Murakami, "Rotational motion of magnons and the thermal Hall effect," *Phys. Rev. B* **84** (Nov, 2011) 184406.

[106] R. Shindou, J.-i. Ohe, R. Matsumoto, S. Murakami, and E. Saitoh, "Chiral spin-wave edge modes in dipolar magnetic thin films," *Phys. Rev. B* **87** (May, 2013) 174402.

[107] R. Shindou, R. Matsumoto, S. Murakami, and J.-i. Ohe, "Topological chiral magnonic edge mode in a magnonic crystal," *Phys. Rev. B* **87** (May, 2013) 174427.

[108] L. Zhang, J. Ren, J.-S. Wang, and B. Li, "Topological magnon insulator in insulating ferromagnet," *Phys. Rev. B* **87** (Apr, 2013) 144101.

[109] A. Mook, J. Henk, and I. Mertig, "Magnon Hall effect and topology in kagome lattices: A theoretical investigation," *Phys. Rev. B* **89** (Apr, 2014) 134409.

[110] A. Mook, J. Henk, and I. Mertig, "Edge states in topological magnon insulators," *Phys. Rev. B* **90** (Jul, 2014) 024412.

[111] V. M. Yakovenko, "Quantum Hall effect in quasi-one-dimensional conductors," *Phys. Rev. B* **43** (May, 1991) 11353–11366.

[112] J. Klinovaja, P. Stano, A. Yazdani, and D. Loss, "Topological Superconductivity and Majorana Fermions in RKKY Systems," *Phys. Rev. Lett.* **111** (Nov, 2013) 186805.

[113] C. L. Kane, R. Mukhopadhyay, and T. C. Lubensky, "Fractional Quantum Hall Effect in an Array of Quantum Wires," *Phys. Rev. Lett.* **88** (Jan, 2002) 036401.

[114] J. Klinovaja and Y. Tserkovnyak, "Quantum spin Hall effect in strip of stripes model," *Phys. Rev. B* **90** (Sep, 2014) 115426.

[115] P. Jordan and E. Z. Wigner, "Über das Paulische Äquivalenzverbot," 1928.

[116] V. Galitski, "Fermionization transform for certain higher-dimensional quantum spin models," *Phys. Rev. B* **82** (Aug, 2010) 060411.

[117] R. Micnas, J. Ranninger, and S. Robaszkiewicz, "Superconductivity in narrow-band systems with local nonretarded attractive interactions," *Rev. Mod. Phys.* **62** (Jan, 1990) 113–171.

[118] T. Giamarchi, "Theoretical framework for quasi-one dimensional systems," *Chem. Rev.* **104** (2004) 5037.

[119] X.-L. Qi and S.-C. Zhang, "Topological insulators and superconductors," *Rev. Mod. Phys.* **83** (2011) 1057–1110.

[120] O. Breunig, M. Garst, E. Sela, B. Buldmann, P. Becker, L. Bohatý, R. Müller, and T. Lorenz, "Spin-$\frac{1}{2}$ XXZ Chain System Cs_2CoCl_4 in a Transverse Magnetic Field," *Phys. Rev. Lett.* **111** (Oct, 2013) 187202.

[121] E. Goovaerts, H. De Raedt, and D. Schoemaker, "Pseudospin Dynamics of the One-Dimensional $S = \frac{1}{2}$ XY System $PrCl_3$ Studied by Electronic Raman Scattering," *Phys. Rev. Lett.* **52** (Apr, 1984) 1649–1652.

[122] H.-J. Mikeska and A. Kolezhuk, *One-dimensional magnetism.* Springer Berlin Heidelberg, 2004.

[123] V. Gritsev, B. Normand, and D. Baeriswyl, "Phase diagram of the Heisenberg spin ladder with ring exchange," *Phys. Rev. B* **69** (Mar, 2004) 094431.

[124] S. Capponi, P. Lecheminant, and M. Moliner, "Quantum phase transitions in multileg spin ladders with ring exchange," *Phys. Rev. B* **88** (Aug, 2013) 075132.

[125] H. Bruus and K. Flesberg, *Many-body Quantum Theory in Condensed Matter Physics*. Oxford University Press, Oxford, 2004.

[126] J. Sinova, S. O. Valenzuela, J. Wunderlich, C. H. Back, and T. Jungwirth, "Spin Hall effects," *Rev. Mod. Phys.* **87** (Oct, 2015) 1213–1260.

[127] A. V. Scherbakov, A. S. Salasyuk, A. V. Akimov, X. Liu, M. Bombeck, C. Brüggemann, D. R. Yakovlev, V. F. Sapega, J. K. Furdyna, and M. Bayer, "Coherent Magnetization Precession in Ferromagnetic (Ga,Mn)As Induced by Picosecond Acoustic Pulses," *Phys. Rev. Lett.* **105** (Sep, 2010) 117204.

[128] J.-W. Kim, M. Vomir, and J.-Y. Bigot, "Ultrafast Magnetoacoustics in Nickel Films," *Phys. Rev. Lett.* **109** (Oct, 2012) 166601.

[129] C. Kittel, "Interaction of Spin Waves and Ultrasonic Waves in Ferromagnetic Crystals," *Phys. Rev.* **110** (May, 1958) 836–841.

[130] K. Uchida, H. Adachi, T. An, T. Ota, M. Toda, B. Hillebrands, S. Maekawa, and E. Saitoh, "Long-range spin Seebeck effect and acoustic spin pumping," *Nat. Mat.* **10** (2011) 737.

[131] M. Weiler, H. Huebl, F. S. Goerg, F. D. Czeschka, R. Gross, and S. T. B. Goennenwein, "Spin Pumping with Coherent Elastic Waves," *Phys. Rev. Lett.* **108** (Apr, 2012) 176601.

[132] N. Ogawa, W. Koshibae, A. J. Beekman, N. Nagaosa, M. Kubota, M. Kawasaki, and Y. Tokura, "Photodrive of magnetic bubbles via magnetoelastic waves," *Proceedings of the National Academy of Sciences* **112** (2015), no. 29 8977–8981.

[133] A. M. Kosevich, B. A. Ivanov, and A. S. Kovalev, "Magnetic Solitons," *Phys. Rep.* **194** (1990) 117–238.

[134] N. L. Schryer and L. R. Walker, "The motion of 180° domain walls in uniform dc magnetic fields," *Journal of Applied Physics* **45** (1974), no. 12 5406–5421.

[135] A. P. Pyatakov, A. S. Sergeev, E. P. Nikolaeva, T. B. Kosykh, A. V. Nikolaev, K. A. Zvezdin, and A. K. Zvezdin, "Micromagnetism and topological defects in magnetoelectric media," *Physics-Uspekhi* **58** (2015), no. 10 981–992.

[136] "Current-driven excitation of magnetic multilayers," *J. Magn. Magn. Mater.* **159** (1996) L1–L7.

[137] L. Berger, "Emission of spin waves by a magnetic multilayer traversed by a current," *Phys. Rev. B* **54** (Oct, 1996) 9353–9358.

[138] A. C. Swaving and R. A. Duine, "Current-induced torques in continuous antiferromagnetic textures," *Phys. Rev. B* **83** (Feb, 2011) 054428.

[139] K. M. D. Hals, Y. Tserkovnyak, and A. Brataas, "Phenomenology of Current-Induced Dynamics in Antiferromagnets," *Phys. Rev. Lett.* **106** (Mar, 2011) 107206.

[140] A. A. Kovalev and Y. Tserkovnyak, "Thermomagnonic spin transfer and Peltier effects in insulating magnets," *Europhys. Lett.* **97** (2012), no. 6 67002.

[141] W. Jiang, P. Upadhyaya, Y. Fan, J. Zhao, M. Wang, L.-T. Chang, M. Lang, K. L. Wong, M. Lewis, Y.-T. Lin, J. Tang, S. Cherepov, X. Zhou, Y. Tserkovnyak, R. N. Schwartz, and K. L. Wang, "Direct Imaging of Thermally Driven Domain Wall Motion in Magnetic Insulators," *Phys. Rev. Lett.* **110** (Apr, 2013) 177202.

[142] P. Yan, X. S. Wang, and X. R. Wang, "All-Magnonic Spin-Transfer Torque and Domain Wall Propagation," *Phys. Rev. Lett.* **107** (Oct, 2011) 177207.

[143] E. G. Tveten, A. Qaiumzadeh, and A. Brataas, "Antiferromagnetic Domain Wall Motion Induced by Spin Waves," *Phys. Rev. Lett.* **112** (Apr, 2014) 147204.

[144] V. G. Baryakhtar, B. A. Ivanov, and M. V. Chetkin, "Dynamics of domain walls in weak ferromagnets," *Soviet Physics Uspekhi* **28** (jul, 1985) 563–588.

[145] S. O. Demokritov, A. I. Kirilyuk, N. M. Kreines, V. I. Kudinov, V. B. Smirnov, and M. V. Chetkin, "Interaction of the moving domain wall with phonons," *J. Magn. Magn. Mater.* **102** (1991) 339–353.

[146] M. T. Bryan, J. Dean, and D. A. Allwood, "Dynamics of stress-induced domain wall motion," *Phys. Rev. B* **85** (2012) 144411.

[147] K. Lipert, S. Bahr, F. Wolny, P. Atkinson, U. Weissker, T. Muhl, O. G. Schmidt, B. Buchner, and R. Klingeler, "An individual iron nanowire-filled carbon nanotube probed by micro-Hall magnetometry," *Applied Physics Letters* **97** (2010), no. 21 212503.

[148] M. Kardar, *Statistical physics of fields*. Cambridge University Press, Cambridge, 2007.

[149] H. Goldstein, C. Poole, and J. Safko, *Classical Mechanics*. Addison Wesley, 3rd ed. ed., 2002.

[150] E. I. Butikov, "Misconceptions about the energy of waves in a strained string," *Physica Scripta* **86** (2012), no. 3 035403.

[151] P. M. Chaikin and T. C. Lubensky, *Principles of condensed matter physics*. Cambridge University Press, Cambridge, 2000.

[152] S. K. Kim, Y. Tserkovnyak, and O. Tchernyshyov, "Propulsion of a domain wall in an antiferromagnet by magnons," *Phys. Rev. B* **90** (2014) 104406.

[153] A. K. Zvezdin and A. A. Mukhin, "Magnetoelastic solitary waves and supersonic domain-wall dynamics," *Zh. Eksp. Teor. Fiz* **102** (1992) 577–599.

[154] L. D. Landau and E. M. Lifshitz, *Quantum Mechanics*. Butterworth-Heinemann, Oxford, 3rd ed. ed., 1976.

[155] L. Zhang and Q. Niu, "Angular Momentum of Phonons and the Einstein–de Haas Effect," *Phys. Rev. Lett.* **112** (2014) 085503.

[156] A. Altland and B. Simons, *Condensed Matter Field Theory*. Cambridge University Press, Cambridge, 2006.

[157] P. Yan, A. Kamra, Y. Cao, and G. E. W. Bauer, "Angular and linear momentum of excited ferromagnets," *Phys. Rev. B* **88** (2013) 144413.

[158] O. Tchernyshyov, "Conserved momenta of a ferromagnetic soliton," *Ann. Phys.* **363** 98–113.

[159] I. V. Baryakhtar and B. A. Ivanov, "On Nonlinear Waves of Magnetization in Antiferromagnets," *Fiz. Nizk. Temp.* **5** (1979) 759–772.

[160] A. F. Andreev and V. I. Marchenko, "Symmetry and the macroscopic dynamics of magnetic materials," *Soviet Physics Uspekhi* **23** (1980), no. 1 21–34.

[161] H. V. Gomonay and V. M. Loktev, "Spin transfer and current-induced switching in antiferromagnets," *Phys. Rev. B* **81** (2010) 144427.

[162] H. Matthews and R. C. LeCraw, "Acoustic Wave Rotation by Magnon-Phonon Interaction," *Phys. Rev. Lett.* **8** (1962) 397–399.

[163] A. Sytcheva, U. Löw, S. Yasin, J. Wosnitza, S. Zherlitsyn, P. Thalmeier, T. Goto, P. Wyder, and B. Lüthi, "Acoustic Faraday effect in $Tb_3Ga_5O_{12}$," *Phys. Rev. B* **81** (2010) 214415.

[164] D. Jiles, *Introduction to Magnetism and Magnetic Materials*. Chapman and Hall, New York, 1991.

[165] D. I. Tokman and I. V. Pozdnyakova, "Inverse acoustic Faraday effect in single molecule magnets," *Eur. Phys. J. B* **86** (2013) 207.

[166] M. König, S. Wiedmann, C. Brüne, A. Roth, H. Buhmann, L. W. Molenkamp, X. L. Qi, and S. C. Zhang, "Quantum spin hall insulator state in HgTe quantum wells," *Science* **318** (2007) 766.

[167] K. Nowack, E. M. Spanton, M. Baenninger, M. König, J. R. Kirtley, B. Kalisky, C. Ames, P. Leubner, C. Brüne, H. Buhmann, L. W. Molenkamp, D. Goldhaber-Gordon, and K. A. Moler, "Imaging currents in HgTe quantum wells in the quantum spin hall regime," *Nat. Mater.* **12** (2013) 787.

[168] K. v. Klitzing, G. Dorda, and M. Pepper, "New method for High-Accuracy Determination of the Fine-Structure Constant Based on Quantized Hall Resistance," *Phys. Rev. Lett.* **45** (1980), no. 6 494.

[169] Y. Y. Wei, J. Weis, K. v. Klitzing, and K. Eberl, "Edge Strips in the Quantum Hall Regime Imaged by a Single-Electron Transistor," *Phys. Rev. Lett.* **81** (1998), no. 8 1674–1677.

[170] A. Yacoby, H. F. Hess, T. A. Fulton, L. N. Pfeiffer, and K. W. West, "Electrical imaging of the quantum Hall state," *Solid State Commun.* **111** (1999) 1–13.

[171] J. Weis and K. v. Klitzing, "Metrology and microscopic picture of the integer quantum Hall effect," *Phil. Trans. R. Soc. A* **369** (2011) 3954.

[172] M. E. Suddards, A. Baumgartner, M. Henini, and C. J. Mellor, "Scanning capacitance imaging of compressible and incompressible quantum Hall effect edge strips," *New Journal of Physics* **14** (2012), no. 8 083015.

[173] D. Zhang, S. Schmult, V. Venkatachalam, W. Dietsche, and A. Yacoby, "Local compressibility measurement of the $\nu_{tot} = 1$ quantum Hall state in a bilayer electron system," *Phys. Rev. B* **87** (2013) 205304.

[174] N. Pascher, C. Rössler, T. Ihn, K. Ensslin, C. Reichl, and W. Wegscheider, "Imaging the Conductance of Integer and Fractional Quantum Hall Edge States," *Phys. Rev. X* **4** (2014) 011014.

[175] L. J. Yin, H. Jiang, J. B. Qiao, and L. He, "Direct imaging of topological edge states at a bilayer graphene domain wall," *Nature Communications* **7** (2016) 11760.

[176] L. Peng, Y. Yuan, G. Li, X. Yang, J. J. Xian, C. J. Yi, Y. G. Shi, and Y. S. Fu, "Observation of topological states residing at step edges of WTe_2," *Nature Communications* **8** (2017) 659.

[177] K. Panos, R. R. Gerhardts, J. Weis, and K. von Klitzing, "Current distribution and Hall potential landscape towards breakdown of the quantum Hall effect: a scanning force microscopy investigation," *New Journal of Physics* **16** (2014), no. 11 113071.

[178] F. Dahlem, E. Ahlswede, J. Weis, and K. v. Klitzing, "Cryogenic scanning force microscopy of quantum Hall samples: Adiabatic transport originating in anisotropic depletion at contact interfaces," *Phys. Rev. B* **82** (2010) 121305.

[179] A. Yacoby, H. L. Störmer, N. S. Wingreen, L. N. Pfeiffer, K. W. Baldwin, and K. W. West, "Nonuniversal Conductance Quantization in Quantum Wires," *Phys. Rev. Lett.* **77** (1996) 4612.

[180] O. M. Auslaender, H. Steinberg, A. Yacoby, Y. Tserkovnyak, B. I. Halperin, K. W. Baldwin, L. N. Pfeiffer, and K. W. West, "Spin-Charge Separation and Localization in One Dimension," *Science* **308** (2005) 88.

[181] H. Steinberg, G. Barak, A. Yacoby, L. N. Pfeiffer, K. W. West, B. I. Halperin, and K. L. Hur, "Charge fractionalization in quantum wires," *Nat. Phys.* **4** (2008) 116.

[182] C. P. Scheller, T. M. Liu, G. Barak, A. Yacoby, L. N. Pfeiffer, K. W. West, and D. M. Zumbühl, "Possible Evidence for Helical Nuclear Spin Order in GaAs Quantum Wires," *Phys. Rev. Lett.* **112** (2014) 066801.

[183] B. Braunecker, P. Simon, and D. Loss, "Nuclear magnetism and electron order in interacting one-dimensional conductors," *Phys. Rev. B* **80** (2009) 165119.

[184] B. I. Halperin, "Quantized Hall conductance, current-carrying edge states, and the existence of extended states in a two-dimensional disordered potential," *Phys. Rev. B* **25** (1982), no. 4 2185.

[185] A. H. MacDonald and P. Středa, "Quantized Hall effect and edge currents," *Phys. Rev. B* **29** (1984) 1616.

[186] M. Büttiker, "Absence of backscattering in the quantum Hall effect in multiprobe conductors," *Phys. Rev. B* **38** (1988), no. 14 9375.

[187] M. Huber, M. Grayson, M. Rother, R. A. Deutschmann, W. Biberacher, W. Wegscheider, M. Bichler, and G. Abstreiter, "Tunneling in the quantum Hall regime between orthogonal quantum wells," *Physica E* **12** (2002) 125–128.

[188] M. Huber, M. Grayson, D. Schuh, M. Bichler, W. Biberacher, W. Wegscheider, and G. Abstreiter, "Probing the electrostatics of integer and quantum hall edges with momentum-resolved tunneling spectroscopy," *Physica E* **22** (2004) 164–167.

[189] M. Huber, M. Grayson, M. Rother, W. Biberacher, W. Wegscheider, and G. Abstreiter, "Structure of a Single Sharp Quantum Hall Edge Probed by Momentum-Resolved Tunneling," *Phys. Rev. Lett.* **94** (2005) 016805.

[190] L. Pfeiffer, H. L. Störmer, K. W. Baldwin, K. W. West, A. R. Goñi, A. Pinczuk, R. C. Ashoori, M. M. Dignam, and W. Wegscheider, "Cleaved edge overgrowth for quantum wire fabrication," *J. Cryst. Growth.* **127** (1993) 849.

[191] W. Wegscheider, W. Kang, L. N. Pfeiffer, K. W. West, H. L. Störmer, and K. W. Baldwin, "High-mobility transport along single quasi-1D quantum wires formed by cleaved edge overgrowth," *Solid State Electron.* **37** (1994) 547.

[192] A. Yacoby, H. L. Störmer, K. W. Baldwin, L. N. Pfeiffer, and K. W. West, "Magneto Transport Spectroscopy on a Quantum Wire," *Solid State Commun.* **101** (1997) 77.

[193] O. M. Auslaender, A. Yacoby, R. de Picciotto, K. W. Baldwin, L. N. Pfeiffer, and K. W. West, "Tunneling Spectroscopy of the Elementary Excitations on a One-Dimensional Wire," *Science* **295** (2002) 825.

[194] H. Steinberg, O. M. Auslaender, A. Yacoby, J. Qian, G. A. Fiete, Y. Tserkovnyak, B. I. Halperin, K. W. Baldwin, L. N. Pfeiffer, and K. W. West, "Localization transition in a ballistic quantum wire," *Phys. Rev. B* **73** (2006) 113307.

[195] Y. Tserkovnyak, B. I. Halperin, O. M. Auslaender, and A. Yacoby, "Finite-Size Effects in Tunneling between Parallel Quantum Wires," *Phys. Rev. Lett.* **89** (2002) 136805.

[196] Y. Tserkovnyak, B. I. Halperin, O. M. Auslaender, and A. Yacoby, "Interference and zero-bias anomaly in tunneling between Luttinger-liquid wires," *Phys. Rev. B* **68** (2003) 125312.

[197] M. Grayson, L. Steinke, D. Schuh, M. Bichler, L. Hoeppel, J. Smet, K. v. Klitzing, D. K. Maude, and G. Abstreiter, "Metallic and insulating states at a bent quantum Hall junction," *Phys. Rev. B* **76** (2007) 201304.

[198] L. Steinke, P. Cantwell, E. Stach, D. Schuh, A. Fontcuberta i Morral, M. Bichler, G. Abstreiter, and M. Grayson, "Hartree simulations of coupled quantum Hall edge states in corner-overgrown heterostructures," *Phys. Rev. B* **87** (2013) 165428.

[199] L. Onsager, "Reciprocal relations in irreversible processes," *Phys. Rev* **37** (1931) 405.

[200] D. B. Chklovskii, B. I. Shklovskii, and L. I. Glazman, "Electrostatics of edge channels," *Phys. Rev. B* **46** (1992), no. 7 4026.

[201] K. Lier and R. R. Gerhardts, "Self-consistent calculations of edge channels in laterally confined two-dimensional electron systems," *Phys. Rev. B* **50** (1994), no. 11 7757.

[202] K. Güven and R. R. Gerhardts, "Self-consistent local equilibrium model for density profile distribution of dissipative currents in a Hall bar under strong magnetic fields," *Phys. Rev. B* **67** (2003), no. 11 115327.

[203] A. Siddiki and R. R. Gerhardts, "Thomas-Fermi-Poisson theory of screening for laterally confined and unconfined two-dimensional electron systems in strong magnetic fields," *Phys. Rev. B* **68** (2003) 125315.

[204] A. Siddiki and R. R. Gerhardts, "Incompressible strips in dissipative Hall bars as origin of quantized Hall plateaus," *Phys. Rev. B* **70** (2004) 195335.

[205] J. Weis and K. von Klitzing, "Metrology and microscopic picture of the integer quantum Hall effect," *Phil. Trans. R. Soc. A* **369** (2011) 3954.

[206] S. Baer, C. Rössler, E. C. de Wiljes, P. L. Ardelt, T. Ihn, K. Ensslin, C. Reichl, and W. Wegscheider, "Interplay of fractional quantum Hall states and localization in quantum point contacts," *Phys. Rev. B* **89** (2014) 085424.

[207] R. R. Gerhardts, K. Panos, and J. Weis, "Current-induced asymmetries of incompressible strips in narrow quantum Hall systems," *New Journal of Physics* **15** (2013), no. 7 073034.

[208] O. E. Dial, R. C. Ahoori, L. N. Pfeiffer, and K. W. West, "High-resolution spectroscopy of two-dimensional electron systems," *Nature* **448** (2007) 176.

[209] O. E. Dial, R. C. Ahoori, L. N. Pfeiffer, and K. W. West, "Anomalous structure in the single particle spectrum of the fractional quantum Hall effect," *Nature* **464** (2010) 566.

[210] R. J. Nicholas, R. J. Haug, and K. v. Klitzing, "Exchange enhancement of the spin splitting in a GaAs-$Ga_xAl_{1-x}As$ heterojunction," *Phys. Rev. B* **37** (1988), no. 3 1294.

[211] J. Dempsey, B. Y. Gelfand, and B. I. Halperin, "Electron-Electron Interactions and Spontaneous Spin Polarization in Quantum Hall Edge States," *Phys. Rev. Lett.* **70** (1993), no. 23 3639.

[212] F. D. M. Haldane, "'Luttinger liquid theory' of one-dimensional quantum fluids. I. Properties of the Luttinger model and their extension to the general 1D interacting spinless Fermi gas," *Journal of Physics C: Solid State Physics* **14** (1981), no. 19 2585.

[213] F. D. M. Haldane, "Effective Harmonic-Fluid Approach to Low-Energy Properties of One-Dimensional Quantum Fluids," *Phys. Rev. Lett.* **47** (1981) 1840.

[214] A. M. Chang, L. N. Pfeiffer, and K. W. West, "Observation of Chiral Luttinger Behavior in Electron Tunneling into Fractional Quantum Hall Edges," *Phys. Rev. Lett.* **77** (1996) 2538.

[215] M. Zülicke, E. Shimshoni, and M. Governale, "Momentum-resolved tunneling into fractional quantum Hall edges," *Phys. Rev. B* **65** (2002) R241315.

[216] A. Seidel and K. Yang, "Momentum-resolved tunneling into the Pfaffian and anti-Pfaffian edges," *Phys. Rev. B* **80** (2009) 241309.

[217] A. C. Clark, K. K. Schwarzwälder, T. Bandi, D. Maradan, and D. M. Zumbühl, "Magnetic cooling for microkelvin nanoelectronics on a cryofree platform," *Rev. Sci. Instr.* **81** (2010) 103904.

[218] L. Casparis, M. Meschke, D. Maradan, A. C. Clark, C. P. Scheller, K. K. Schwarzwälder, J. P. Pekola, and D. M. Zumbühl, "Metallic Coulomb blockade thermometry down to 10 mK and below," *Rev. Sci. Instum.* **83** (2012) 083903.

[219] C. P. Scheller, S. Heizmann, K. Bedner, D. Giss, M. Meschke, D. M. Zumbühl, and A. C. Gossard, "Silver-Epoxy Microwave Filters and Thermalizers for Millikelvin Experiments," *Appl. Phys. Lett.* **104** (2014) 211106.

[220] D. Maradan, L. Casparis, T.-M. Liu, D. E. F. Biesinger, C. P. Scheller, D. M. Zumbühl, J. Zimmerman, and A. C. Gossard, "GaAs Quantum Dot Thermometry Using Direct Transport and Charge Sensing," *J. Low Temp. Phys.* **175** (2014) 784.

[221] A. V. Feshchenko, L. Casparis, I. M. Khaymovich, D. Maradan, O.-P. Saira, M. Palma, M. Meschke, J. P. Pekola, and D. M. Zumbühl, "Tunnel junction thermometry down to millikelvin temperatures," *Phys. Rev. Appl.* **4** (2015) 034001.

[222] M. Palma, C. P. Scheller, D. Maradan, A. V. Feshchenko, M. Meschke, and D. M. Zumbühl, "On-and-off chip cooling of a Coulomb blockade thermometer down to 2.8 mK," *Appl. Phys. Lett.* **111** (2017), no. 25 253105.

[223] M. Palma, D. Maradan, L. Casparis, T.-M. Liu, F. Froning, and D. M. Zumbühl, "Magnetic cooling for microkelvin nanoelectronics on a cryofree platform," *Rev. Sci. Instr.* **88** (2017) 043902.